

# **APPLIED COMPUTATIONAL ELECTROMAGNETICS SOCIETY JOURNAL**

**Special Issue on Antennas, Metasurfaces,  
and Testing Methodologies for 5G/6G  
Communication - Part I**

**Guest Editor:**

Yingsong Li, Harbin Engineering University

December 2022

Vol. 37 No. 12

ISSN 1054-4887

The ACES Journal is abstracted in INSPEC, in Engineering Index, DTIC, Science Citation Index Expanded, the Research Alert, and to Current Contents/Engineering, Computing & Technology.

The illustrations on the front cover have been obtained from the ARC research group at the Department of Electrical Engineering, Colorado School of Mines

Published, sold and distributed by: River Publishers, Alsbjergvej 10, 9260 Gistrup, Denmark

# THE APPLIED COMPUTATIONAL ELECTROMAGNETICS SOCIETY

<http://aces-society.org>

## EDITORS-IN-CHIEF

**Atef Elsherbeni**  
Colorado School of Mines, EE Dept.  
Golden, CO 80401, USA

**Sami Barmada**  
University of Pisa, ESE Dept.  
56122 Pisa, Italy

## ASSOCIATE EDITORS

**Maokun Li**  
Tsinghua University  
Beijing 100084, China

**Wei-Chung Weng**  
National Chi Nan University, EE Dept.  
Puli, Nantou 54561, Taiwan

**Paolo Mezzanotte**  
University of Perugia  
I-06125 Perugia, Italy

**Mauro Parise**  
University Campus Bio-Medico of Rome  
00128 Rome, Italy

**Alessandro Formisano**  
Seconda Università di Napoli  
81031 CE, Italy

**Luca Di Rienzo**  
Politecnico di Milano  
20133 Milano, Italy

**Yingsong Li**  
Harbin Engineering University  
Harbin 150001, China

**Piotr Gas**  
AGH University of Science and Technology  
30-059 Krakow, Poland

**Lei Zhao**  
Jiangsu Normal University  
Jiangsu 221116, China

**Riyadh Mansoor**  
Al-Muthanna University  
Samawa, Al-Muthanna, Iraq

**Long Li**  
Xidian University  
Shaanxi, 710071, China

**Sima Noghianian**  
Commscope  
Sunnyvale, CA 94089, USA

**Lijun Jiang**  
University of Hong Kong, EEE Dept.  
Hong Kong

**Steve J. Weiss**  
US Army Research Laboratory  
Adelphi Laboratory Center (RDRL-SER-M)  
Adelphi, MD 20783, USA

**Nunzia Fontana**  
University of Pisa  
56122 Pisa, Italy

**Shinishihiro Ohnuki**  
Nihon University  
Tokyo, Japan

**Jiming Song**  
Iowa State University, ECE Dept.  
Ames, IA 50011, USA

**Stefano Selleri**  
DINFO - University of Florence  
50139 Florence, Italy

**Kubilay Sertel**  
The Ohio State University  
Columbus, OH 43210, USA

**Toni Bjorninen**  
Tampere University  
Tampere, 33100, Finland

**Yu Mao Wu**  
Fudan University  
Shanghai 200433, China

**Giulio Antonini**  
University of L'Aquila  
67040 L'Aquila, Italy

**Santanu Kumar Behera**  
National Institute of Technology  
Rourkela-769008, India

**Fatih Kaburcuk**  
Sivas Cumhuriyet University  
Sivas 58140, Turkey

**Antonio Musolino**  
University of Pisa  
56126 Pisa, Italy

**Daniele Romano**  
University of L'Aquila  
67100 L'Aquila, Italy

**Huseyin Savci**  
Istanbul Medipol University  
34810 Beykoz, Istanbul

**Abdul A. Arkadan**  
Colorado School of Mines, EE Dept.  
Golden, CO 80401, USA

**Alireza Baghai-Wadji**  
University of Cape Town  
Cape Town, 7701, South Africa

**Zhixiang Huang**  
Anhui University  
China

**Salvatore Campione**  
Sandia National Laboratories  
Albuquerque, NM 87185, USA

**Marco Arjona López**  
La Laguna Institute of Technology  
Torreon, Coahuila 27266, Mexico

**Amin Kargar Behbahani**  
Florida International University  
Miami, FL 33174, USA

**Ibrahim Mahariq**  
American University of the Middle East  
Kuwait and University of  
Turkish Aeronautical Association  
Turkey

**Kaikai Xu**  
University of Electronic Science  
and Technology of China  
China

**Laila Marzall**  
University of Colorado, Boulder  
Boulder, CO 80309, USA

## EDITORIAL ASSISTANTS

**Matthew J. Inman**  
University of Mississippi, EE Dept.  
University, MS 38677, USA

**Shanell Lopez**  
Colorado School of Mines, EE Dept.  
Golden, CO 80401, USA

## EMERITUS EDITORS-IN-CHIEF

**Duncan C. Baker**  
EE Dept. U. of Pretoria  
0002 Pretoria, South Africa

**Allen Glisson**  
University of Mississippi, EE Dept.  
University, MS 38677, USA

**Ahmed Kishk**  
Concordia University, ECS Dept.  
Montreal, QC H3G 1M8, Canada

**Robert M. Bevensee**  
Box 812  
Alamo, CA 94507-0516

**Ozlem Kilic**  
Catholic University of America  
Washington, DC 20064, USA

**David E. Stein**  
USAF Scientific Advisory Board  
Washington, DC 20330, USA

## EMERITUS ASSOCIATE EDITORS

**Yasushi Kanai**  
Niigata Inst. of Technology  
Kashiwazaki, Japan

**Mohamed Abouzahra**  
MIT Lincoln Laboratory  
Lexington, MA, USA

**Alexander Yakovlev**  
University of Mississippi, EE Dept.  
University, MS 38677, USA

**Levent Gurel**  
Bilkent University  
Ankara, Turkey

**Sami Barmada**  
University of Pisa, ESE Dept.  
56122 Pisa, Italy

**Ozlem Kilic**  
Catholic University of America  
Washington, DC 20064, USA

**Erdem Topsakal**  
Mississippi State University, EE Dept.  
Mississippi State, MS 39762, USA

**Alistair Duffy**  
De Montfort University  
Leicester, UK

**Fan Yang**  
Tsinghua University, EE Dept.  
Beijing 100084, China

**Rocco Rizzo**  
University of Pisa  
56123 Pisa, Italy

**Atif Shamim**  
King Abdullah University of Science and  
Technology (KAUST)  
Thuwal 23955, Saudi Arabia

William O'Keefe Coburn  
US Army Research Laboratory  
Adelphi, MD 20783, USA

**Mohammed Hadi**  
Kuwait University, EE Dept.  
Safat, Kuwait

**Amedeo Capozzoli**  
Univerita di Naoli Federico II, DIETI  
I-80125 Napoli, Italy

**Wenxing Li**  
Harbin Engineering University  
Harbin 150001, China

**Qiang Ren**  
Beihang University  
Beijing 100191, China

## EMERITUS EDITORIAL ASSISTANTS

**Khaleb ElMaghoub**  
Trimble Navigation/MIT  
Boston, MA 02125, USA

**Kyle Patel**  
Colorado School of Mines, EE Dept.  
Golden, CO 80401, USA

**Christina Bonnington**  
University of Mississippi, EE Dept.  
University, MS 38677, USA

**Anne Graham**  
University of Mississippi, EE Dept.  
University, MS 38677, USA

**Madison Lee**  
Colorado School of Mines, EE Dept.  
Golen, CO 80401, USA

**Allison Tanner**  
Colorado School of Mines, EE Dept.  
Golden, CO 80401, USA

**Mohamed Al Sharkawy**  
Arab Academy for Science and Technology, ECE Dept.  
Alexandria, Egypt

TABLE OF CONTENTS

Design of Millimeter Wave Radar Antenna Array with Flat-top Pattern  
Nan Wang, Yibo Zhang, Kun Gao, Jian Wu, Beijia Dang, Zhizhan Kong,  
Haokun Wei, Feng Gao, and Shuangyang Liu ..... 1186

Optimal Antenna Pattern Design for the Instantaneous MIMO Channel  
Cuicui Zhang, Shuo Wang, Ming Zhang, Xiaobo Liu, and Anxue Zhang ..... 1192

Isolation Improvement Using the Field-Circuit Combined Method for In-Band  
Full-Duplex MIMO Antenna Arrays  
Yiran Da, Jianjia Yi, Jianxing Li, and Xiaoming Chen ..... 1200

Wideband Decoupled 8-Element MIMO Mobile Phone Antenna for Sub-6GHz  
5G NR Bands  
Jiagang He, Shichao Zhu, Jie Yu, Hao Li, and Gaosheng Li ..... 1208

A Simple Single-fed Left/Right-Hand Circular Polarization Antenna for GPS Applications  
Lulu Meng, Yingsong Li, and Zhixiang Huang ..... 1216

A Novel 4×4 MIMO Antenna Decoupled by T-Shaped Dummy Antenna with  
High Robustness for 5G Mobile Devices  
Junlin Wang, Xiaomin Chen, Xin Wang, and Min Wei ..... 1225

High-Isolated Full-Duplex Dongle Antenna Based on Even-Mode Suppression for B5G  
Communications  
Yiran Da, Xiaoming Chen, Aofang Zhang, Kunpeng Wei, and Ahmed A. Kishk ..... 1232

Wideband Single-Fed Circularly Polarized Stacked Patch Antenna With L-Shaped Stub  
Wen Li, Wei Xue, Yingsong Li, Xiang Xiong, Kwok L. Chung, and Zhixiang Huang ..... 1240

A Circularly Polarized Patch Antenna Array with Reduced Mutual Coupling Using the  
Aperture-Loading Decoupling Technique  
Xin Cheng, Bingyi Qian, Le Chang, Jinlin Liu, and Xiaoming Chen ..... 1249

Simultaneous Transmit and Receive Phased Array System Architecture and Prototype  
Comprehensive Verification  
Jie Zhang and Hongchao Wu ..... 1257

# Design of Millimeter Wave Radar Antenna Array with Flat-top Pattern

Nan Wang<sup>1</sup>, Yibo Zhang<sup>2</sup>, Kun Gao<sup>3</sup>, Jian Wu<sup>4</sup>, Beijia Dang<sup>4</sup>, Zhizhan Kong<sup>2</sup>,  
Haokun Wei<sup>1</sup>, Feng Gao<sup>1</sup>, and Shuangyang Liu<sup>5</sup>

<sup>1</sup>Power Research Institute of State Grid Shaanxi Electric Power Corporation Limited  
Xi'an, 710000, China  
232960917@qq.com, haokun.wei@foxmail.com, 15291830460@163.com

<sup>2</sup>State Grid Shaanxi Electric Power Corporation Limited  
Xi'an, 710000, China  
zhangyibo7373@163.com, kongzhizhan@126.com

<sup>3</sup>State Grid Xi'an Electric Power Corporation  
Xi'an, 710000, China  
Gaokun@sn.xa.sgcc.com.cn

<sup>4</sup>State Grid Shaanxi Power Transmission and Transformation Engineering Co., Ltd.  
Xi'an, 710000, China  
1053914849@qq.com, 172801427@qq.com

<sup>5</sup>School of Information and Communications Engineering  
Xi'an Jiaotong University, Xi'an, 710049, China  
lsy6820@stu.xjtu.edu.cn

**Abstract** – In this paper, a planar millimeter wave radar array antenna with flat-top pattern is proposed for wide detection angle. Firstly, the Chebyshev synthesis method is used to design the linear array with high gain and low sidelobe pattern which works in the 24 GHz frequency band. The maximum gain of the linear array is roughly 15 dBi, and the main-sidelobe ratio is close to 20 dB. By setting the excitations and phases distribution of the planar array feeding network, a  $5 \times 4$  antenna array with a flat-top pattern is obtained. The simulated and measured results show that the radar antenna array has a wide half-power beamwidth of 88 degrees, which can ensure that the automotive radar has a longer detection range and a larger monitoring angle.

**Index Terms** – Chebyshev synthesis method, flat-top pattern, low sidelobe, millimeter wave radar antenna.

## I. INTRODUCTION

Millimeter wave radar array antennas play an important role in unmanned driving and automobile collision avoidance radar systems due to their short wavelength, low sidelobe, high gain and other advantages. The 24 GHz vehicle-mounted radar can be used to detect obstacles around the vehicle and the driving environment

in front. In order to meet the needs of speed, distance and angle measurement, the vehicle-mounted radar has certain requirements for the designed antenna. Firstly, the antenna needs to have higher gain in order to obtain a greater detection distance. Secondly, the antenna needs to have a suitable beamwidth in order to avoid interference from vehicles in other lanes, and at the same time, the antenna also needs to meet the characteristics of low sidelobes [1, 2].

The design of antenna array is one of the main methods to improve the performance of the antenna [3, 4]. For instance, we can use optimization algorithms to design a shaped radiation pattern of the antenna array according to a specific application scenario [5–7], which quickly can save time and effort. Different array synthesis methods can also be used to achieve the goal [1, 8–10]. For example, antenna arrays with a sector beam pattern are designed on the premise of maintaining controllable excitation amplitude and phase according to the Woodward-Lawson array synthesis method [8]. The Taylor synthesis method [9] and the Chebyshev synthesis method [1, 10] are used to design antenna arrays with low sidelobes and high gain patterns. C. Wang, Y. Chen and S. Yang propose a planar antenna array with flat-top and sharp cut-off radiation patterns and the half-power beamwidth (HPBW) of the array in both the H-plane and

E-plane exceeds  $45^\circ$ , but its gain is low [11]. R. Chopra and G. Kumar design a  $9 \times 9$  high-gain planar antenna array by using two different feeding methods at the linear arrays' edges of the E-plane and H-plane, which are U-series and angular feeding, respectively [12]. The cross-polarization of the array is low, but its beamwidth is narrow. The performance of these antennas cannot meet the application requirements of millimeter wave automotive radar antennas perfectly.

In this paper, a millimeter wave radar antenna array with high gain, low sidelobe and wide beam is designed according to the application requirements of 24 GHz vehicle radars. The antenna array structures are designed and described in Section II, and the simulated and measured results are shown in Section III. Finally, the conclusion is given at the last section.

## II. ANTENNA DESIGN

### A. Design of series-fed antenna

The microstrip patch antenna is a commonly used radar antenna structure, which has the advantages of efficient processing, small size, and a flexible structure. However, the gain of a single microstrip antenna is relatively low, only 6 dBi-8 dBi [1, 2]. Therefore, we arrange the single microstrip antennas in a certain way to form a five-element series-fed linear array, and use MATLAB to obtain the current amplitude when  $N = 5$  and sidelobe level (SLL) = 20 dB according to the Chebyshev synthesis method. The current amplitude is shown in Table 1.

The center frequency  $f_0$  of the series-fed antenna designed in this paper is 24 GHz, and we use Rogers 5880 dielectric substrate with a dielectric constant of 2.2, a loss tangent of 0.0009, and a thickness of 0.508 mm, which is one of the commonly used radio frequency and microwave circuit boards, with high coverage frequency and low loss. Since the current amplitude value is related to the impedance of the patch, and the impedance changes with the change of the patch size, we can change the current amplitude value by adjusting the size of the patch to make it meet our expectations. As adjacent patches are coupled with each other and then change the amplitude and phase of each other's currents, it is necessary to optimize the parameters by using the simulation software HFSS to determine the optimal size of each patch. In addition, as the width of the patch changes, the length of the feeder connecting the microstrip patch also needs to be optimized to ensure that the distance between adjacent patches is approximately  $\lambda_g$  ( $\lambda_g$  is the guided wavelength at  $f_0$ ), so that the array elements are in phase to achieve edge-fire characteristics.

The model of the series-fed linear array is shown in Fig. 1. The main feeder of the antenna (0.5 mm line width) and the 50-ohm port feeder (1.5 mm line width)

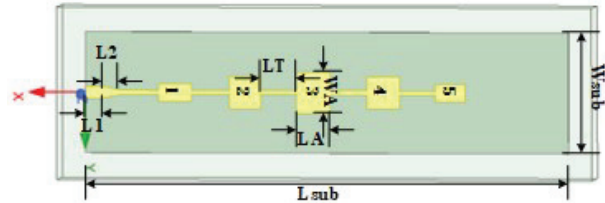


Fig. 1. The structure of the series-fed five-element patch linear array.

Table 1: Current amplitude coefficient calculated by Chebyshev synthesis method

Element Number	Coefficient Lowercase	Normalized Coefficient
1	1	0.5176
2	1.6085	0.8326
3	1.9319	1
4	1.6085	0.8326
5	1	0.5176

Table 2: Values of the patches parameters

Patch Number	WA(mm)	LA(mm)	LT(mm)
1	2.2	4.1	4.6
2	4.1	3.9	4.7
3	5.1	4.1	4.5
4	4	4	4.6
5	2.2	3.7	4.5

are transitioned using a gradual structure to achieve good impedance matching, where  $L_1 = 2$  mm,  $L_2 = 2.5$  mm, and other optimized parameter values are shown in Table 2.

### B. Design of the planar array antenna

Based on the series-fed linear array designed by the Chebyshev synthesis method, we designed a millimeter wave radar antenna array with a wider beam to identify and track multiple targets at the same time. A  $5 \times 4$  area array is simulated and the model structure and physical figure are shown in Figs. 2 and 3, respectively.  $D=6.25$  mm, which is  $0.5\lambda_0$  ( $\lambda_0$  is the free space wavelength at  $f_0$ ). Furthermore, by using a deep learning parameter optimization algorithm, the excitations and phases distribution of the feeding network when  $N = 4$ , HPBW  $>80^\circ$  are obtained quickly, as shown in Table 3. The feeding network is composed of cascaded multi-level T-type networks, the first-level T-type power distribution network is an equal power distribution network, and the one-to-four power distribution feeding network realizes the power distribution ratio and phase

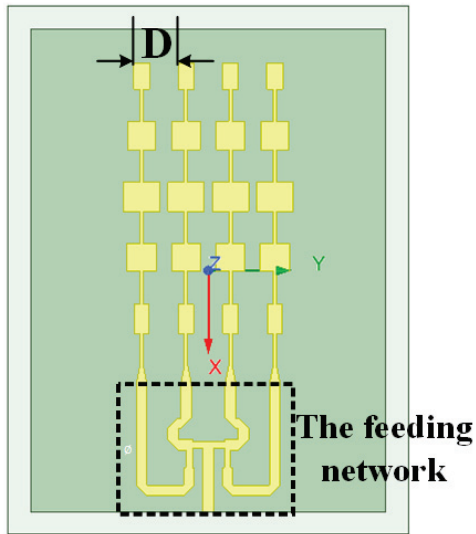


Fig. 2. The structure of the 5×4 planar array antenna.

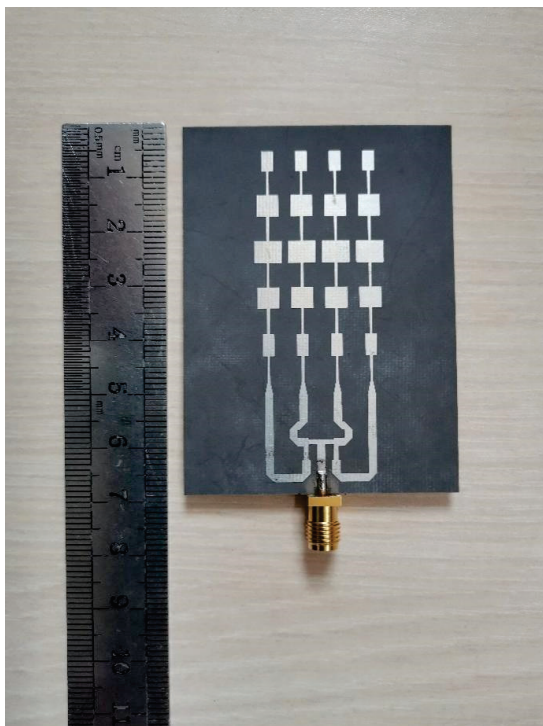


Fig. 3. The fabricated planar array antenna photograph.

difference that meet the requirements of the flat-top pattern. The simulated results are shown in Figs. 4 and 5, respectively.

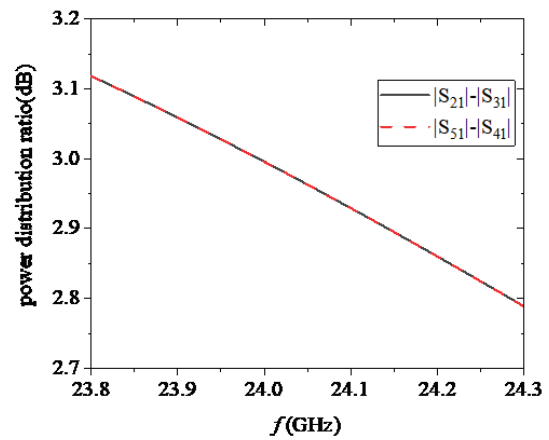


Fig. 4. The simulated power distribution ratio of the feeding network.

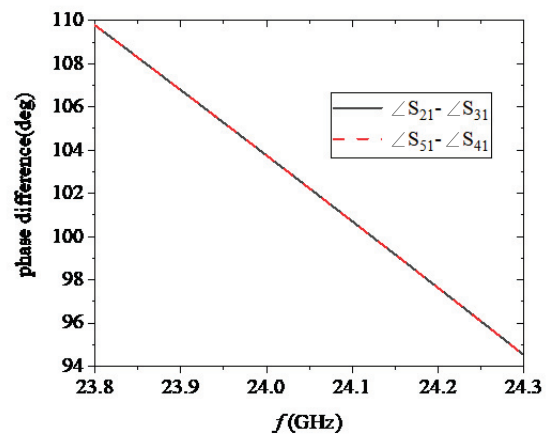


Fig. 5. The simulated phase difference of the feeding network.

Table 3: Distributions of excitations and phases

Port Number	Optimized Excitations	Excitations of Feeding Network
1	1∠0	1∠0
2	2∠-102	1.99∠-103.78
3	2∠-102	1.99∠-103.78
4	1∠0	1∠0

### III. RESULTS

#### A. Results of series-fed antenna

The simulated reflection coefficients and radiation patterns results of the series-fed linear array are shown in Figs. 6 and 7, respectively. Its working bandwidth is 23.983-24.36 GHz, so the absolute bandwidth is

0.377 GHz, and the relative bandwidth is 1.57%. The maximum gain of the E-plane pattern is about 15 dBi, and the SLL is nearly 20 dB. The microstrip antenna unit forms a series-fed array only in the X direction. Therefore, compared with the patterns of a single rectangular microstrip patch antenna [1, 2], the SLL and beamwidth of the E-plane (XOZ plane) are significantly reduced, while the SLL and beam width of the H plane pattern (YOZ plane) are almost unchanged.

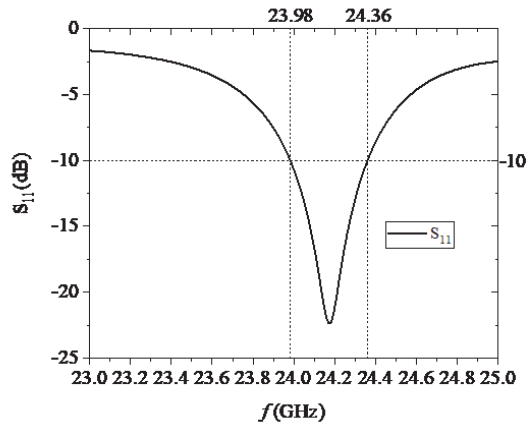


Fig. 6. The simulated reflection coefficients of the series-fed five-element patch linear array.

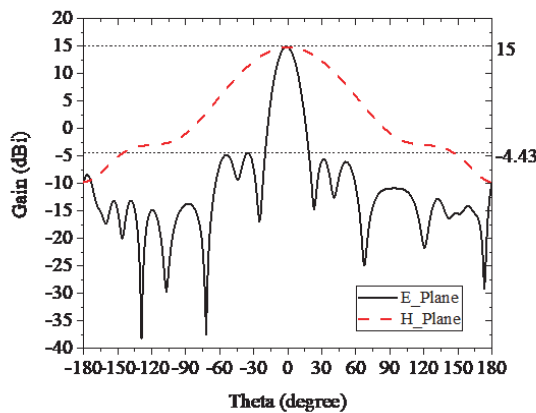


Fig. 7. The simulated radiation patterns of the series-fed five-element patch linear array.

**B. Results of the planar array antenna**

Figure 8 shows the simulated and measured S-parameters of the radar antenna array. Its bandwidth covers the working frequency band of a 24 GHz vehicle radar (24-24.25 GHz), and the return loss is greater

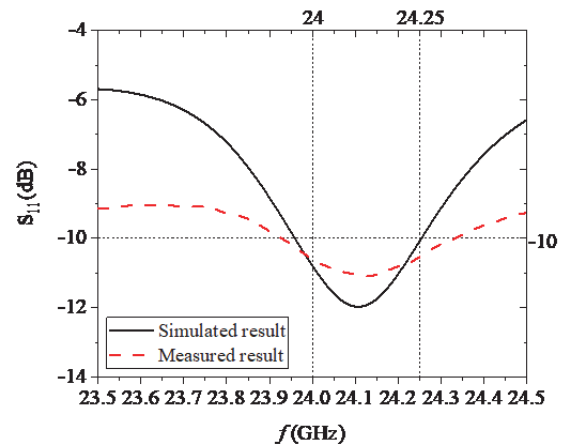


Fig. 8. The simulated and measured reflection coefficients of the planar array antenna.

than 10 dB within the required bandwidth. The anechoic chamber can be used to test the antenna patterns in the low frequency band [13]. In this paper, the near-field anechoic chamber test method is used to test them. The comparison between the simulated and measured radiation patterns are shown in Figs. 9 and 10. The maximum gain is roughly 12.7 dBi, and the SLL of the E-plane pattern is close to 13 dB. Furthermore, the HPBW of the H-plane is approximately 88 degrees, the SLL is greater than 17 dB, the average gain is about 12.3 dBi, and the fluctuation range is less than  $\pm 0.5$  dB in the beam range from  $-25^\circ$  to  $+25^\circ$ . Compared with the uniformly excited array, the antenna array has a lower maximum gain, which is a compromise between the gain and beamwidth [14]. There are some errors between all the

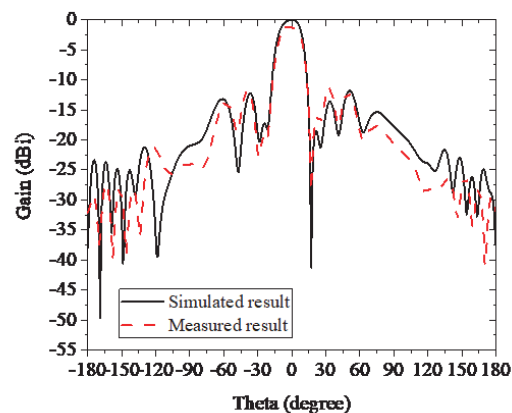


Fig. 9. The simulated and measured E-plane of the planar array antenna.

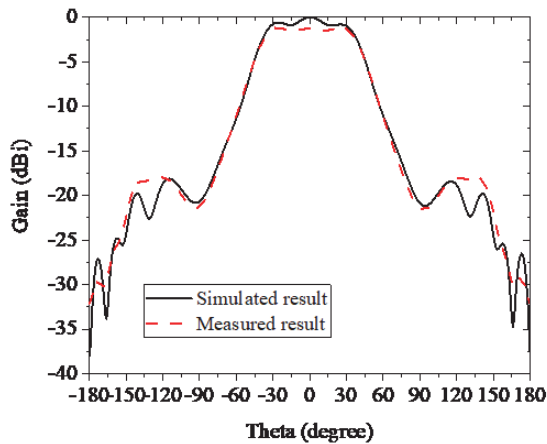


Fig. 10. The simulated and measured H-plane of the planar array antenna.

measured and simulated results, which may be caused by the actual plate loss and machining accuracy, but the trend of the two is the same, and the measured results are fundamentally consistent with the simulation results.

#### IV. CONCLUSION

In this paper, a millimeter wave radar antenna array with the flat-top pattern is designed for the application requirements of 24 GHz vehicle radars. The Chebyshev synthesis method is used to design the series-fed linear array, and the appropriate excitation and phase distribution of the array elements are obtained by using a deep learning parameter optimization algorithm. The radar antenna array bandwidth covers the working frequency (24-24.25 GHz) band of a 24 GHz vehicle radar, the maximum gain is roughly 12.7 dBi, and the SLL of the E-plane pattern is nearly 13 dB. The HPBW of the H-plane is approximately 88 degrees, and the average gain is about 12.3 dBi and the fluctuation range is less than  $\pm 0.5$  dB in the beam range of  $-25^\circ$  to  $+25^\circ$ , and the SLL is greater than 17 dB. In summary, the radar antenna array has high gain, appropriate lobe width, and at the same time satisfies the characteristics of low side-lobes, so it has a good performance.

#### ACKNOWLEDGMENT

This work was supported by the project of State Grid Shaanxi Electric Power Company Limited under Grant No. 5226SX21002Q.

#### REFERENCES

- [1] Y. Zhang, Y. Chen, Y. Liu, and Y. Lu, "Millimeter wave microstrip antenna array for automotive collision avoidance radar," *Int. Appl. Computat. Electromagn. Soc. Symp. - China (ACES)*, Beijing, pp. 1-2, Jul. 2018.
- [2] Y. Chen, Y. Liu, Y. Zhang, Z. Yue, and Y. Jia, "A 24 GHz millimeter wave microstrip antenna array for automotive radar," *Int. Symp. Antenn. and Propag. (ISAP)*, Xi'an, pp. 1-2, Oct. 2019.
- [3] X. Chen, M. Zhao, H. Huang, Y. Wang, S. Zhu, C. Zhang, J. Yi, and A. A. Kishk, "Simultaneous decoupling and decorrelation scheme of MIMO arrays," *IEEE Trans. Vehicular Technol.*, vol. 71, no. 2, pp. 2164-2169, 2022.
- [4] Y. Wang, X. Chen, X. Liu, J. Yi, J. Chen, A. Zhang, and A. A. Kishk, "Improvement of diversity and capacity of MIMO system using scatterer array," *IEEE Trans. Antenn. and Propag.*, vol. 70, no. 1, pp. 789-794, 2022.
- [5] G. K. Mahanti, T. K. Sinhamahapatra, A. Ahmed, and A. Chakrabarty, "Synthesis of flat-top beam pattern with a multiple concentric circular ring array antenna," *IEEE Region 10 and 3rd Int. Conf. Ind. and Inf. Sys.*, Kharagpur, pp. 1-4, Dec. 2008.
- [6] J. Jiping, Z. Youling, and B. Yong, "An improved array pattern synthesis algorithm based on Chebyshev polynomial," *Proc. 2011 Int. Conf. Comput. Sci. and Netw. Technol.*, Harbin, pp. 1125-1127, Dec. 2011.
- [7] J. K. Modi, K. K. Suman, R. K. Gangwar, and V. S. Gangwar, "Investigation on realistic synthesis approach for shaped beam patterns and its validation through EM simulation study," *IEEE Int. Conf. Electron., Comput. and Commun. Technol. (CONECCT)*, Bangalore, pp. 1-4, Jul. 2020.
- [8] A. M. Maruti and B. S. N. Kishore, "High gain and wide bandwidth array antenna for sector beam pattern synthesis," *Prog. Electromagn. Res. Lett.*, vol. 100, pp. 109-116, 2021.
- [9] L. A. R. Solano, M. S. Perez, and D. P. Santos, "Design, simulation and test of a slot antenna array using one parameter Taylor synthesis in the GHz range," *IEEE Latin America Trans.*, vol. 13, no. 10, pp. 3210-3215, 2015.
- [10] F. Enache, D. Deperateanu, A. Enache, and F. Popescu, "Sparse array antenna design based on dolph-chebyshev and genetic algorithms," *8th Int. Conf. Electron., Comput. Artific. Intell. (ECAI)*, Ploiesti, pp. 1-4, Jul. 2016.
- [11] C. Wang, Y. Chen, and S. Yang, "Dual-band dual-polarized antenna array with flat-top and sharp cutoff radiation patterns for 2G/3G/LTE cellular bands," *IEEE Trans. Antenn. and Propag.*, vol. 66, no. 11, pp. 5907-5917, 2018.
- [12] R. Chopra and G. Kumar, "Series- and corner-fed planar microstrip antenna arrays," *IEEE Trans.*

*Antenn. and Propag.*, vol. 67, no. 9, pp. 5982-5990, 2019.

- [13] W. Xue, Y. Ren, X. Chen, Z. Wang, Y. Li, and Y. Huang, "Measurement uncertainty of antenna efficiency measured using the two-antenna method in a reverberation chamber," *Applied Computational Electromagnetics Society (ACES) Journal*, vol. 36, no. 9, pp. 1152-1158, Sep. 2021.
- [14] X. Cai, W. Geyi, and Y. Guo, "A compact rectenna with flat-top angular coverage for RF energy harvesting," *IEEE Antenn. and Wirel. Propag. Lett.*, vol. 20, no. 7, pp. 1307-1311, Jul. 2021.



**Nan Wang** received his MSc degree in electromagnetic and microwave technology from Xidian University, Xi'an, China, in 2010. His current research interests include the research of operation and maintenance technology of power transmission and transformation equipment.



**Yibo Zhang** received his MSc degree in power electronics and power transmission from Xi'an University of Technology, Xi'an, China, in 2012. His current research interests include equipment technical maintenance and safety supervision.



**Kun Gao** received his MSc degree in electrical engineering and automation from North China Electric Power University, Beijing, China, in 2008. His current research interests include the operation and maintenance management of power transmission and transformation equipment.



**Jian Wu** received his BSc degree in electrical engineering and automation from Xi'an Polytechnic University, Xi'an, China, in 2020. His current research interests include transmission line construction management.



**Beijia Dang** graduated from Xi'an Electric Power College, Xi'an, China, in 2019 and majoring in electrical engineering and automation. Her current research interests include power grid emergency management.



**Zhizhan Kong** received the BSc degree in electrical engineering and automation from Shaanxi University of Technology, Hanzhong, China, in 1989. His current research interests include the operation and maintenance management of power transmission and transformation equipment.



**Haokun Wei** received his Ph.D. degree in electrical engineering from Xi'an University of Technology, Xi'an, China, in 2020. His current research interests include the power system, new energy consumption and other aspects.



**Feng Gao** received his MSc degree in electrical engineering and automation from Xi'an Jiaotong University, Xi'an, China, in 2010. His current research interests include the research of operation and maintenance technology of power transmission and transformation equipment.



**Shuangyang Liu** received the BSc degree in Information Engineering from Xi'an Jiaotong University, Xi'an, China, in 2020. She is currently pursuing an MSc degree in electronic information at Xi'an Jiaotong University. Her current research interests include metamaterials and antennas.

# Optimal Antenna Pattern Design for the Instantaneous MIMO Channel

Cuicui Zhang, Shuo Wang, Ming Zhang, Xiaobo Liu, and Anxue Zhang

School of Information and Communications Engineering  
Xi'an Jiaotong University, Xi'an, 710049, China  
anxuezhang@mail.xjtu.edu.cn

**Abstract** – Due to the rapid attenuation of the millimeter wave, it is necessary to use very large-scale antenna arrays in millimeter wave communications to get ultra-high directivity which improves the transmission distance and the signal-to-noise ratio. Considering the cost of large-scale RF links, analog beamforming plays an important role in large-scale MIMO communications. This paper discusses the calculation method of the antenna pattern that best matches the instantaneous MIMO channel in analog beamforming. By giving piecewise modeling on the antenna pattern, singular value decomposition and the water-filling algorithm are used to obtain the antenna pattern and the power distribution among antennas. The optimal antenna pattern can provide the target pattern for antenna synthesis to get the maximum capacity. The simulation results show that the method is effective.

**Index Terms** – maximum capacity, MIMO, optimal antenna pattern, spatial cluster model.

## I. INTRODUCTION

With commercial use of the 5th generation mobile communication technology and the layout of 6th generation mobile communication technology, the communication system is developing toward ultra-large bandwidth and ultra-low delay. Ultra-large-scale antenna technology and millimeter wave communication have received extensive attention [1-4]. Due to the rapid attenuation of the millimeter wave, beamforming technology of very large-scale antenna arrays is proposed [5]. Considering the high cost of large-scale RF links, analog beamforming plays an important role in large-scale MIMO communications. Analog beamforming based on the statistical channel model has been used to guide antenna design [6-8]. There is also hybrid beamforming based on new antenna structures [9], including hybrid beamforming on smart antennas [10], reconfigurable intelligent surface antennas [11, 12], and holographic antennas [13, 14].

However, the above methods use models in which the antenna parameters are included in the performance measurement of the communication system. The antenna design parameters are obtained first through optimization

algorithms and then the antenna pattern is obtained indirectly. All these methods require the designers to have knowledge both in antenna and communication fields, and different antenna structures need to be remodeled and reanalyzed, and the algorithm complexity is high.

Due to the cluster sparsity of millimeter wave channels, the complexity of beamforming methods using the deterministic and semi-deterministic spatial cluster channel model is reduced. In this paper, for the instantaneous MIMO channel which is modeled by the spatial cluster channel model, the antenna pattern best matching the wireless propagation environment is directly obtained. Without the antenna parameters involved, only the piecewise modeling and power constraints of the antenna pattern are carried out. The closed-form of the optimal antenna pattern can be obtained by using singular value decomposition. The optimal pattern can be used as the target pattern in antenna synthesis methods, such as the genetic algorithm [15], particle swarm optimization algorithm [16, 17], and other intelligence algorithms [18, 19], to further obtain the antenna parameters.

Antenna mutual coupling is a very important parameter that will greatly affect the performance of a tight array. There is literature on how to reduce mutual coupling in MIMO systems [20, 21]. In this paper, the antenna spacing is set to half wavelength, when the effect of mutual coupling is small. To focus on the optimal pattern design, the mutual coupling is not considered in this paper. It will be considered in further work.

## II. OPTIMAL ANTENNA DESIGN OF MIMO-SU

TR 38.901 [22] studies a channel model for frequencies from 0.5 to 100 GHz in the fifth generation mobile communication system. It is widely used in the research in the communication field. According to the channel description in 3GPP TR 38.901 [22], the antenna radiation characteristic is an important factor of the wireless channel. The antenna radiation characteristic and the wireless propagation environment jointly determine the wireless channel [23]. If the wireless propagation environment is full rank, such as a rich multi-path environment, the rank loss of the antenna radiation characteristic

will lead to rank loss of the transmission channel, which will result in the reduction of the multiplexing gain. On the contrary, a suitable antenna radiation characteristic not only ensures the full rank of the transmission channel but also has a good condition number in terms of diversity gain and multiplexing gain [24]. Therefore, it is valuable to find out the most suitable antenna pattern for the wireless propagation environment.

### A. System model

3GPP TR 38.901 is the specification that studies on channel model for frequencies from 0.5 to 100 GHz use, in which the channel is modeled as some spatial clusters. The channel coefficients without polarization in consideration are given by (1) when the transmitting antenna array and receiving antenna array are both linear arrays, and both aligned with the x-axis, as shown in Fig. 1.

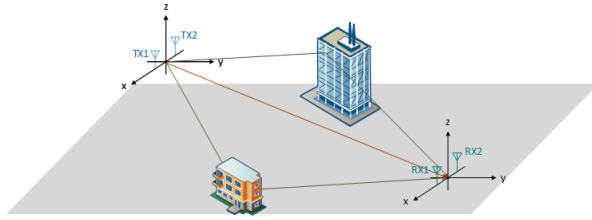


Fig. 1. Channel with 3 clusters.

$$H_{m,k} = \sum_{n=1}^N ( h_n f_{r_m}(AoA_n, ZoA_n) * f_{t_k}(AoD_n, ZoD_n) * e^{j(m-1)*\kappa d_r * \cos(AoA_n) \cos(ZoA_n)} * e^{j(k-1)*\kappa d_t * \cos(AoD_n) \cos(ZoD_n)} ), \quad (1. a)$$

$$\alpha_n = \kappa d_r * \cos(AoA_n) * \cos(ZoA_n), \quad (1. b)$$

$$\beta_n = \kappa d_t * \cos(AoD_n) * \cos(ZoD_n). \quad (1. c)$$

The channel coefficients can be written in matrix form (2), which is shown at the bottom of this page, where K and M are the numbers of transmitting and receiving antennas and N is the number of clusters.  $\alpha_n$  is the phase difference caused by the nth cluster on

two adjacent receiving antennas,  $\beta_n$  is the phase difference caused by the nth cluster on two adjacent transmitting antennas.  $f_{t_k}(\theta, \varphi)$  is the kth Tx antenna pattern.  $f_{r_m}(\theta, \varphi)$  is the mth Rx antenna pattern.  $\tilde{H}_{M \times N}$  shows the joint effect of the wireless propagation environment and the receiving antenna on the channel.  $F_{N \times K}$  shows the effect of the directivity of the transmission antenna on the channel.

Assuming that the receiving antenna is omnidirectional, the numbers of transmitting and receiving antennas are both 2, the antenna spacing is half a wavelength, and the propagation environment has 3 clusters as shown in Fig. 1, then the channel matrix H is given by (3), which is shown on the next page.

### B. Problem formulation

The capacity for MIMO channels is given by (4), [25].

$$C = \log_2 \det \left( I_M + \frac{P}{\sigma^2} H_{M \times K} * R_{ss} * H_{M \times K}^H \right) = \log_2 \det \left( I_M + \frac{P}{\sigma^2} \tilde{H}_{M \times N} * F_{N \times K} * R_{ss} * F_{N \times K}^H * \tilde{H}_{N \times M}^H \right), \quad (4. a)$$

$$R_{ss} = \begin{bmatrix} p_1 & \dots & 0 \\ \vdots & \ddots & \vdots \\ 0 & \dots & p_K \end{bmatrix}, \quad (4. b)$$

where  $R_{ss}$  is the covariance matrix of the transmission data streams, representing the transmission power distribution. The normalized  $p_k$  satisfies,

$$\sum_k p_k = 1, \quad (5)$$

the optimal antenna pattern can be obtained by the following optimization problem,

$$\text{maximize } C, \quad (6. a)$$

(F,  $R_{ss}$ )

subject to

$$\text{Tr}(R_{ss}) = 1. \quad (6. b)$$

To solve the above problem, the power constraint of  $R_{ss}$  is not enough, the constraint about the antenna pattern matrix F is needed too. The antenna pattern matrix F needs to be modeled first.

$$H_{M \times K} = \begin{bmatrix} h_1 f_{r_1}(AoA_1, ZoA_1) & h_2 f_{r_1}(AoA_2, ZoA_2) & \dots & h_N f_{r_1}(AoA_N, ZoA_N) \\ h_1 f_{r_2}(AoA_1, ZoA_1) e^{j\alpha_1} & h_2 f_{r_2}(AoA_2, ZoA_2) e^{j\alpha_2} & \dots & h_N f_{r_2}(AoA_N, ZoA_N) e^{j\alpha_N} \\ \vdots & \vdots & \ddots & \vdots \\ h_1 f_{r_M}(AoA_1, ZoA_1) e^{j(M-1)\alpha_1} & h_2 f_{r_M}(AoA_2, ZoA_2) e^{j(M-1)\alpha_2} & \dots & h_N f_{r_M}(AoA_N, ZoA_N) e^{j(M-1)\alpha_N} \end{bmatrix} * \begin{bmatrix} f_{t_1}(AoD_1, ZoD_1) & f_{t_2}(AoD_1, ZoD_1) e^{j\beta_1} & \dots & f_{t_K}(AoD_1, ZoD_1) e^{j(K-1)\beta_1} \\ f_{t_1}(AoD_2, ZoD_2) & f_{t_2}(AoD_2, ZoD_2) e^{j\beta_2} & \dots & f_{t_K}(AoD_2, ZoD_2) e^{j(K-1)\beta_2} \\ \vdots & \vdots & \ddots & \vdots \\ f_{t_1}(AoD_N, ZoD_N) & f_{t_2}(AoD_N, ZoD_N) e^{j\beta_N} & \dots & f_{t_K}(AoD_N, ZoD_N) e^{j(K-1)\beta_N} \end{bmatrix} = \tilde{H}_{M \times N} * F_{N \times K}, \quad (2)$$

$$H_{2 \times 2} = \begin{bmatrix} h_1 & h_2 & h_3 \\ h_1 e^{j\pi \cos(AoA_1) \cos(ZoA_1)} & h_2 e^{j\pi \cos(AoA_2) \cos(ZoA_2)} & h_3 e^{j\pi \cos(AoA_3) \cos(ZoA_3)} \end{bmatrix} * \begin{bmatrix} f_{i_1}(AoD_1, ZoD_1) & f_{i_2}(AoD_1, ZoD_1) e^{j\pi \cos(AoD_1) \cos(ZoD_1)} \\ f_{i_1}(AoD_2, ZoD_2) & f_{i_2}(AoD_2, ZoD_2) e^{j\pi \cos(AoD_2) \cos(ZoD_2)} \\ f_{i_1}(AoD_3, ZoD_3) & f_{i_2}(AoD_3, ZoD_3) e^{j\pi \cos(AoD_3) \cos(ZoD_3)} \end{bmatrix}. \quad (3)$$

### C. Piecewise modeling and constraints on antenna patterns

To solve the above problem, the antenna pattern is piecewise modeled. A sphere can be divided into equal  $S$  parts, in each part, radiation characteristics, such as the electric field, are equal. The description in two-dimensional space is shown in Fig. 2, where the solid line represents the actual pattern, and the dotted line represents the piecewise pattern. To ensure equal power, the integration of the dotted line and solid line are equal. The difference between them will be smaller with the increase of  $S$ .

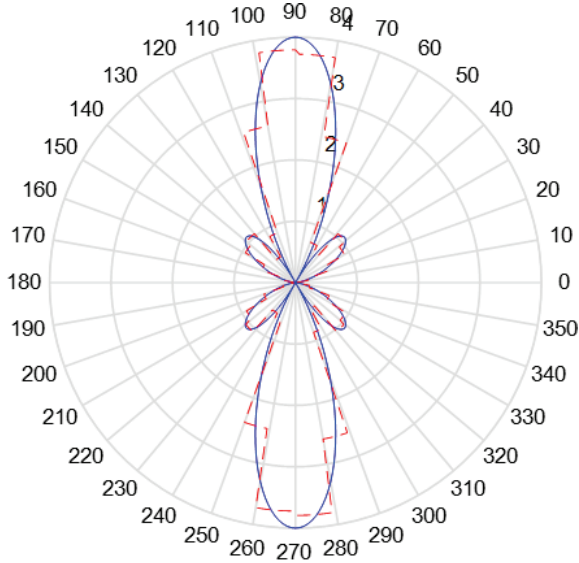


Fig. 2. Piecewise model on antenna pattern.

With the piecewise model, the power constraint is given by (7)

$$\frac{4\pi r^2}{S} \sum_s W_s = P, \quad (7)$$

where  $W_s$  is the power flow density. Therefore, the sum of  $W_n$  representing the antenna radiation power flow density at the angle where the  $n$ th cluster is located is given by (8)

$$\sum_n W_n \leq \frac{P}{4\pi r^2} * S, \quad (8)$$

more precisely,

$$\sum_n W_{s_n} = \frac{P}{4\pi r^2} * S * \gamma, \quad (9)$$

where  $\gamma$  is the ratio of the sum of the power in the angle of the channel clusters to the total power, which depends

on the ability of the antenna to depress the beam at an uninterest angle.

In (1), the distance attenuation factor  $\frac{1}{4\pi r^2}$  has been included in  $h_n$  as the path loss factor, and  $P$  has been picked in the capacity expression of (4.a), so the power constraint of  $F$  is given by (10),

$$\sum_n |f_m(AoD_n, ZoD_n)|^2 = S * \gamma \leq S, \quad (10)$$

here, the beam convergence factor is defined as (11)

$$\rho = S * \gamma, \quad (11)$$

which represents the ability of the antenna to converge beams in the spatial clusters of interest, and is affected by actual antenna parameters. In the subsequent calculation, the beam convergence factor is given as known. The calculation results below show that the beam convergence factor does not change the shape of the pattern, but only affects the power distribution in  $R_{ss}$ .

### D. Problem solving

After the constraint shown in (10), (6) is rewritten by (12),

$$\begin{aligned} & \underset{(F, R_{ss})}{\text{maximize}} \log_2 \det \left( I_M + \frac{P}{\sigma^2} \tilde{H}_{M \times N} * F_{N \times K} * R_{ss} \right. \\ & \left. * F^H_{K \times N} * \tilde{H}^H_{N \times M} \right), \end{aligned} \quad (12.a)$$

subject to

$$\text{Tr}(R_{ss}) = 1, \quad (12.b)$$

$$\sum_n |f_m(AoD_n, ZoD_n)|^2 = S * \gamma, \text{ for } m = 1, \dots, M, \quad (12.c)$$

Under the constraint in  $F$ ,  $F_{N \times K} * R_{ss} * F^H_{K \times N}$  is a symmetric positive definite matrix. Therefore, the optimal solution of  $F$  is the right singular matrix of  $\tilde{H}_{M \times N}$  [25] and  $R_{ss}$  can be obtained by the water-filling algorithm [25].

The singular value matrix is a unitary matrix, and any two columns of it are orthogonal. Therefore, the patterns of different transmitting antennas are orthogonal to each other in the clusters' direction. Meanwhile, in order to ensure a higher signal-to-noise ratio at the receiver, the beam convergence factor should be greater, that means the smaller the gain in the angles except the spatial clusters' direction, the better.

## III. OPTIMAL ANTENNA DESIGN OF MIMO-MU

In the MIMO-MU channel, shown in Fig. 3, the wireless propagation environment matrix for user 1 and user 2 are given by (13) and (14).  $F$  matrix for user 1 and user 2 are given by (15) and (16).

$$\tilde{H}_{2 \times 3}^{user1} = \begin{bmatrix} h_1^1 & h_2^1 & h_3^1 \\ h_1^1 e^{j\pi \cdot \cos(AoA_1^1) \cdot \cos(ZoA_1^1)} & h_2^1 e^{j\pi \cdot \cos(AoA_2^1) \cdot \cos(ZoA_2^1)} & h_3^1 e^{j\pi \cdot \cos(AoA_3^1) \cdot \cos(ZoA_3^1)} \end{bmatrix}, \quad (13)$$

$$\tilde{H}_{2 \times 3}^{user2} = \begin{bmatrix} h_1^2 & h_2^2 & h_3^2 \\ h_1^2 e^{j\pi \cdot \cos(AoA_1^2) \cdot \cos(ZoA_1^2)} & h_2^2 e^{j\pi \cdot \cos(AoA_2^2) \cdot \cos(ZoA_2^2)} & h_3^2 e^{j\pi \cdot \cos(AoA_3^2) \cdot \cos(ZoA_3^2)} \end{bmatrix}, \quad (14)$$

$$F_{3 \times 4}^{user1} = \begin{bmatrix} f_{f_1}(AoD_1^1, ZoD_1^1) & f_{f_2}(AoD_1^1, ZoD_1^1) e^{j\pi \cdot \cos(AoD_1^1) \cdot \cos(ZoD_1^1)} & f_{f_3}(AoD_1^1, ZoD_1^1) e^{j2\pi \cdot \cos(AoD_1^1) \cdot \cos(ZoD_1^1)} & f_{f_4}(AoD_1^1, ZoD_1^1) e^{j3\pi \cdot \cos(AoD_1^1) \cdot \cos(ZoD_1^1)} \\ f_{f_1}(AoD_2^1, ZoD_2^1) & f_{f_2}(AoD_2^1, ZoD_2^1) e^{j\pi \cdot \cos(AoD_2^1) \cdot \cos(ZoD_2^1)} & f_{f_3}(AoD_2^1, ZoD_2^1) e^{j2\pi \cdot \cos(AoD_2^1) \cdot \cos(ZoD_2^1)} & f_{f_4}(AoD_2^1, ZoD_2^1) e^{j3\pi \cdot \cos(AoD_2^1) \cdot \cos(ZoD_2^1)} \\ f_{f_1}(AoD_3^1, ZoD_3^1) & f_{f_2}(AoD_3^1, ZoD_3^1) e^{j\pi \cdot \cos(AoD_3^1) \cdot \cos(ZoD_3^1)} & f_{f_3}(AoD_3^1, ZoD_3^1) e^{j2\pi \cdot \cos(AoD_3^1) \cdot \cos(ZoD_3^1)} & f_{f_4}(AoD_3^1, ZoD_3^1) e^{j3\pi \cdot \cos(AoD_3^1) \cdot \cos(ZoD_3^1)} \end{bmatrix} \quad (15)$$

$$F_{3 \times 4}^{user2} = \begin{bmatrix} f_{f_1}(AoD_1^2, ZoD_1^2) & f_{f_2}(AoD_1^2, ZoD_1^2) e^{j\pi \cdot \cos(AoD_1^2) \cdot \cos(ZoD_1^2)} & f_{f_3}(AoD_1^2, ZoD_1^2) e^{j2\pi \cdot \cos(AoD_1^2) \cdot \cos(ZoD_1^2)} & f_{f_4}(AoD_1^2, ZoD_1^2) e^{j3\pi \cdot \cos(AoD_1^2) \cdot \cos(ZoD_1^2)} \\ f_{f_1}(AoD_2^2, ZoD_2^2) & f_{f_2}(AoD_2^2, ZoD_2^2) e^{j\pi \cdot \cos(AoD_2^2) \cdot \cos(ZoD_2^2)} & f_{f_3}(AoD_2^2, ZoD_2^2) e^{j2\pi \cdot \cos(AoD_2^2) \cdot \cos(ZoD_2^2)} & f_{f_4}(AoD_2^2, ZoD_2^2) e^{j3\pi \cdot \cos(AoD_2^2) \cdot \cos(ZoD_2^2)} \\ f_{f_1}(AoD_3^2, ZoD_3^2) & f_{f_2}(AoD_3^2, ZoD_3^2) e^{j\pi \cdot \cos(AoD_3^2) \cdot \cos(ZoD_3^2)} & f_{f_3}(AoD_3^2, ZoD_3^2) e^{j2\pi \cdot \cos(AoD_3^2) \cdot \cos(ZoD_3^2)} & f_{f_4}(AoD_3^2, ZoD_3^2) e^{j3\pi \cdot \cos(AoD_3^2) \cdot \cos(ZoD_3^2)} \end{bmatrix} \quad (16)$$

$$F_{6 \times 4} = \begin{bmatrix} F_{3 \times 4}^{user1} \\ F_{3 \times 4}^{user2} \end{bmatrix} = \begin{bmatrix} f_{f_1}(AoD_1^1, ZoD_1^1) & f_{f_2}(AoD_1^1, ZoD_1^1) e^{j\pi \cdot \cos(AoD_1^1) \cdot \cos(ZoD_1^1)} & f_{f_3}(AoD_1^1, ZoD_1^1) e^{j2\pi \cdot \cos(AoD_1^1) \cdot \cos(ZoD_1^1)} & f_{f_4}(AoD_1^1, ZoD_1^1) e^{j3\pi \cdot \cos(AoD_1^1) \cdot \cos(ZoD_1^1)} \\ f_{f_1}(AoD_2^1, ZoD_2^1) & f_{f_2}(AoD_2^1, ZoD_2^1) e^{j\pi \cdot \cos(AoD_2^1) \cdot \cos(ZoD_2^1)} & f_{f_3}(AoD_2^1, ZoD_2^1) e^{j2\pi \cdot \cos(AoD_2^1) \cdot \cos(ZoD_2^1)} & f_{f_4}(AoD_2^1, ZoD_2^1) e^{j3\pi \cdot \cos(AoD_2^1) \cdot \cos(ZoD_2^1)} \\ f_{f_1}(AoD_3^1, ZoD_3^1) & f_{f_2}(AoD_3^1, ZoD_3^1) e^{j\pi \cdot \cos(AoD_3^1) \cdot \cos(ZoD_3^1)} & f_{f_3}(AoD_3^1, ZoD_3^1) e^{j2\pi \cdot \cos(AoD_3^1) \cdot \cos(ZoD_3^1)} & f_{f_4}(AoD_3^1, ZoD_3^1) e^{j3\pi \cdot \cos(AoD_3^1) \cdot \cos(ZoD_3^1)} \\ f_{f_1}(AoD_1^2, ZoD_1^2) & f_{f_2}(AoD_1^2, ZoD_1^2) e^{j\pi \cdot \cos(AoD_1^2) \cdot \cos(ZoD_1^2)} & f_{f_3}(AoD_1^2, ZoD_1^2) e^{j2\pi \cdot \cos(AoD_1^2) \cdot \cos(ZoD_1^2)} & f_{f_4}(AoD_1^2, ZoD_1^2) e^{j3\pi \cdot \cos(AoD_1^2) \cdot \cos(ZoD_1^2)} \\ f_{f_1}(AoD_2^2, ZoD_2^2) & f_{f_2}(AoD_2^2, ZoD_2^2) e^{j\pi \cdot \cos(AoD_2^2) \cdot \cos(ZoD_2^2)} & f_{f_3}(AoD_2^2, ZoD_2^2) e^{j2\pi \cdot \cos(AoD_2^2) \cdot \cos(ZoD_2^2)} & f_{f_4}(AoD_2^2, ZoD_2^2) e^{j3\pi \cdot \cos(AoD_2^2) \cdot \cos(ZoD_2^2)} \\ f_{f_1}(AoD_3^2, ZoD_3^2) & f_{f_2}(AoD_3^2, ZoD_3^2) e^{j\pi \cdot \cos(AoD_3^2) \cdot \cos(ZoD_3^2)} & f_{f_3}(AoD_3^2, ZoD_3^2) e^{j2\pi \cdot \cos(AoD_3^2) \cdot \cos(ZoD_3^2)} & f_{f_4}(AoD_3^2, ZoD_3^2) e^{j3\pi \cdot \cos(AoD_3^2) \cdot \cos(ZoD_3^2)} \end{bmatrix} \quad (17)$$

$$\tilde{H}_{2 \times 6}^1 = [\tilde{H}_{2 \times 3}^{user1} \ 0] = \begin{bmatrix} h_1^1 & h_2^1 & h_3^1 & 0 & 0 & 0 \\ h_1^1 e^{j\pi \cdot \cos(AoA_1^1) \cdot \cos(ZoA_1^1)} & h_2^1 e^{j\pi \cdot \cos(AoA_2^1) \cdot \cos(ZoA_2^1)} & h_3^1 e^{j\pi \cdot \cos(AoA_3^1) \cdot \cos(ZoA_3^1)} & 0 & 0 & 0 \end{bmatrix}, \quad (18)$$

$$\tilde{H}_{2 \times 6}^2 = [0 \ \tilde{H}_{2 \times 3}^{user2}] = \begin{bmatrix} 0 & 0 & 0 & h_1^2 & h_2^2 & h_3^2 \\ 0 & 0 & 0 & h_1^2 e^{j\pi \cdot \cos(AoA_1^2) \cdot \cos(ZoA_1^2)} & h_2^2 e^{j\pi \cdot \cos(AoA_2^2) \cdot \cos(ZoA_2^2)} & h_3^2 e^{j\pi \cdot \cos(AoA_3^2) \cdot \cos(ZoA_3^2)} \end{bmatrix}, \quad (19)$$

$$H_{4 \times 4} = \begin{bmatrix} \tilde{H}_{2 \times 6}^1 \\ \tilde{H}_{2 \times 6}^2 \end{bmatrix} * \begin{bmatrix} F_{3 \times 4}^{user1} \\ F_{3 \times 4}^{user2} \end{bmatrix} = \tilde{H}_{4 \times 6} * F_{6 \times 4} = \begin{bmatrix} h_1^1 & h_2^1 & h_3^1 & 0 & 0 & 0 \\ h_1^1 e^{j\pi \cdot \cos(AoA_1^1) \cdot \cos(ZoA_1^1)} & h_2^1 e^{j\pi \cdot \cos(AoA_2^1) \cdot \cos(ZoA_2^1)} & h_3^1 e^{j\pi \cdot \cos(AoA_3^1) \cdot \cos(ZoA_3^1)} & 0 & 0 & 0 \\ 0 & 0 & 0 & h_1^2 & h_2^2 & h_3^2 \\ 0 & 0 & 0 & h_1^2 e^{j\pi \cdot \cos(AoA_1^2) \cdot \cos(ZoA_1^2)} & h_2^2 e^{j\pi \cdot \cos(AoA_2^2) \cdot \cos(ZoA_2^2)} & h_3^2 e^{j\pi \cdot \cos(AoA_3^2) \cdot \cos(ZoA_3^2)} \end{bmatrix} * \begin{bmatrix} f_{f_1}(AoD_1^1, ZoD_1^1) & f_{f_2}(AoD_1^1, ZoD_1^1) e^{j\pi \cdot \cos(AoD_1^1) \cdot \cos(ZoD_1^1)} & f_{f_3}(AoD_1^1, ZoD_1^1) e^{j2\pi \cdot \cos(AoD_1^1) \cdot \cos(ZoD_1^1)} & f_{f_4}(AoD_1^1, ZoD_1^1) e^{j3\pi \cdot \cos(AoD_1^1) \cdot \cos(ZoD_1^1)} \\ f_{f_1}(AoD_2^1, ZoD_2^1) & f_{f_2}(AoD_2^1, ZoD_2^1) e^{j\pi \cdot \cos(AoD_2^1) \cdot \cos(ZoD_2^1)} & f_{f_3}(AoD_2^1, ZoD_2^1) e^{j2\pi \cdot \cos(AoD_2^1) \cdot \cos(ZoD_2^1)} & f_{f_4}(AoD_2^1, ZoD_2^1) e^{j3\pi \cdot \cos(AoD_2^1) \cdot \cos(ZoD_2^1)} \\ f_{f_1}(AoD_3^1, ZoD_3^1) & f_{f_2}(AoD_3^1, ZoD_3^1) e^{j\pi \cdot \cos(AoD_3^1) \cdot \cos(ZoD_3^1)} & f_{f_3}(AoD_3^1, ZoD_3^1) e^{j2\pi \cdot \cos(AoD_3^1) \cdot \cos(ZoD_3^1)} & f_{f_4}(AoD_3^1, ZoD_3^1) e^{j3\pi \cdot \cos(AoD_3^1) \cdot \cos(ZoD_3^1)} \\ f_{f_1}(AoD_1^2, ZoD_1^2) & f_{f_2}(AoD_1^2, ZoD_1^2) e^{j\pi \cdot \cos(AoD_1^2) \cdot \cos(ZoD_1^2)} & f_{f_3}(AoD_1^2, ZoD_1^2) e^{j2\pi \cdot \cos(AoD_1^2) \cdot \cos(ZoD_1^2)} & f_{f_4}(AoD_1^2, ZoD_1^2) e^{j3\pi \cdot \cos(AoD_1^2) \cdot \cos(ZoD_1^2)} \\ f_{f_1}(AoD_2^2, ZoD_2^2) & f_{f_2}(AoD_2^2, ZoD_2^2) e^{j\pi \cdot \cos(AoD_2^2) \cdot \cos(ZoD_2^2)} & f_{f_3}(AoD_2^2, ZoD_2^2) e^{j2\pi \cdot \cos(AoD_2^2) \cdot \cos(ZoD_2^2)} & f_{f_4}(AoD_2^2, ZoD_2^2) e^{j3\pi \cdot \cos(AoD_2^2) \cdot \cos(ZoD_2^2)} \\ f_{f_1}(AoD_3^2, ZoD_3^2) & f_{f_2}(AoD_3^2, ZoD_3^2) e^{j\pi \cdot \cos(AoD_3^2) \cdot \cos(ZoD_3^2)} & f_{f_3}(AoD_3^2, ZoD_3^2) e^{j2\pi \cdot \cos(AoD_3^2) \cdot \cos(ZoD_3^2)} & f_{f_4}(AoD_3^2, ZoD_3^2) e^{j3\pi \cdot \cos(AoD_3^2) \cdot \cos(ZoD_3^2)} \end{bmatrix}. \quad (20)$$

where  $h_n^u$  is the gain of  $n$ th cluster for the  $u$ th user.  $AoA_n^u$ ,  $ZoA_n^u$ ,  $AoD_n^u$  and  $ZoD_n^u$  are the angles of the  $n$ th cluster for the  $u$ th user. Rewrite  $F$  as (17), rewrite  $\tilde{H}_{2 \times 3}^1$  as  $\tilde{H}_{2 \times 6}^1$  shown as (18), rewrite  $\tilde{H}_{2 \times 3}^{user2}$  as  $\tilde{H}_{2 \times 6}^2$  shown as (19). The channel coefficients matrix between 4 receiving anten-

nas and 4 transmitting antennas for MIMO-MU is given by (20).

Therefore, the capacity for MIMO-MU is given by (21),

$$C = \log_2 \det \left( I_4 + \frac{P}{\sigma^2} \tilde{H}_{4 \times 6} * F_{6 \times 4} * R_{ss} * F_{4 \times 6}^H * \tilde{H}_{6 \times 4}^H \right). \quad (21)$$

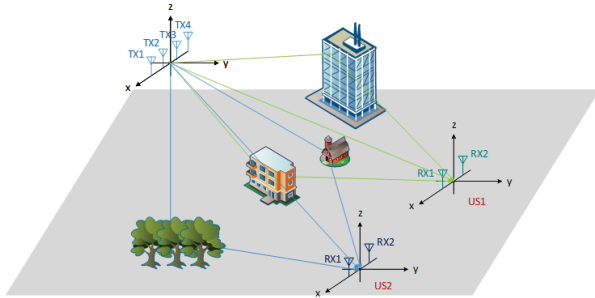


Fig. 3. Channel with two users.

Using the same solution in subsection D, the optimal patterns of  $F$  is the right singular matrix of  $\tilde{H}_{4 \times 6}$ , and  $R_{ss}$  can be obtained by the water-filling algorithm.

Because  $\tilde{H}_{4 \times 6}$  is block matrix, the optimal  $F$  is block matrix too, which is given by (22),

$$F_{6 \times 4} = \begin{bmatrix} V_{3 \times 2}^1 & 0 \\ 0 & V_{3 \times 2}^2 \end{bmatrix}, \quad (22.a)$$

$$\tilde{H}_{2 \times 3}^{user1} = U_{2 \times 3}^1 S_{3 \times 3}^1 V_{3 \times 3}^1, \quad (22.b)$$

$$\tilde{H}_{2 \times 3}^{user2} = U_{2 \times 3}^2 S_{3 \times 3}^2 V_{3 \times 3}^2, \quad (22.c)$$

where  $V_{3 \times 2}^1$  and  $V_{3 \times 2}^2$  are the two columns of  $V_{3 \times 3}^1$  and  $V_{3 \times 3}^2$ , which is the right singular matrix of  $\tilde{H}_{2 \times 3}^{user1}$  and  $\tilde{H}_{2 \times 3}^{user2}$ . There are only two singular values for  $\tilde{H}_{2 \times 3}^{user1}$  and  $\tilde{H}_{2 \times 3}^{user2}$ , so the third column of  $V_{3 \times 3}^1$  and  $V_{3 \times 3}^2$  are both zero vector.

The results in (22) show that the four antennas at the transmitter are divided into two groups. The first two antennas transmit beams to the spatial clusters of user 1, and the last two antennas transmit beams to the spatial clusters of user 2. The spatial decoupling between the two users is realized by the directivity of the transmission antennas.

On the spatial clusters of user 2, the beam gain of the first two transmit antennas should preferably be 0, otherwise it will cause interference to user 2; Similarly, on the spatial clusters of user 1, the beam gain of the last two antennas should preferably be 0, otherwise it will cause interference to user 1.

The above solution is only one of the most direct results of the optimal pattern.  $F$  can also be the vector space of the right singular vector of the wireless propagation environment channel matrix  $\tilde{H}$ . But it needs to cooperate with the digital baseband precoding to realize the decoupling of the data flow to the two users.

That is, the optimal  $F$  matrix should meet the following conditions:

1. Full rank
2. All singular values are equal

The above conditions can ensure that the loss of the condition number and the rank loss of the channel matrix

$H$  will not occur due to the rank loss of  $F$  or the bad condition number of  $F$ .

## IV. SIMULATION

### A. Simulation for MIMO-SU

In the QurdiGa channel model, the BERLIN\_Uma\_NLOS scenario is used to generate a wireless channel with 15 clusters, as shown in Fig. 4. The number of Tx antennas and Rx antennas are both 2. The total power is set to 10 W. The noise power is set to  $10^{-12} mW$  which is close to the noise power of the phone 117dBm. According to the calculation in subsection D, the optimal pattern  $F$  is shown in Fig. 5. Corresponding to different beam convergence factors, the power distribution and capacity are shown in Table 1.

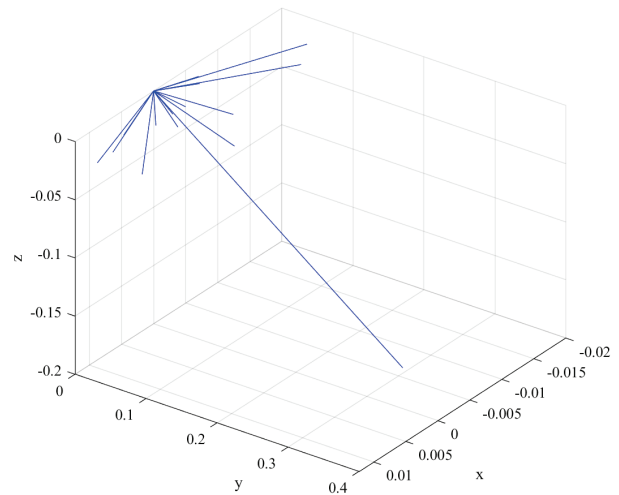


Fig. 4. Clusters for MIMO-SU channel.

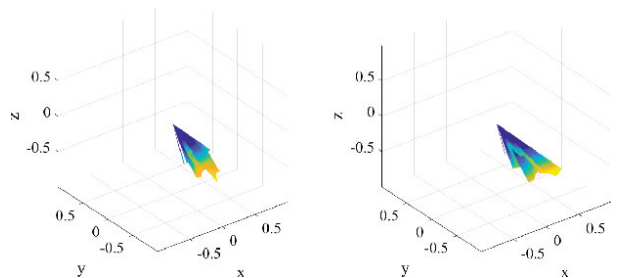


Fig. 5. Optimal patterns for Tx1 (left) and Tx2 (right).

Simulation results show that the patterns of different transmitting antennas are orthogonal to each other in the clusters' direction; The increase of beam convergence factor will increase the gain of the transmitting antenna

Table 1: Power distribution and capacity

Beam Convergence Factor	Power Distribution (W)	Capacity (bits/s/Hz)
$\rho=1$	6.3411, 3.6589	6.7926
$\rho=2$	5.6720, 4.3280	8.4427
$\rho=3$	5.4468, 4.5532	9.4877
$\rho=100$	5.0134, 4.9866	19.3404

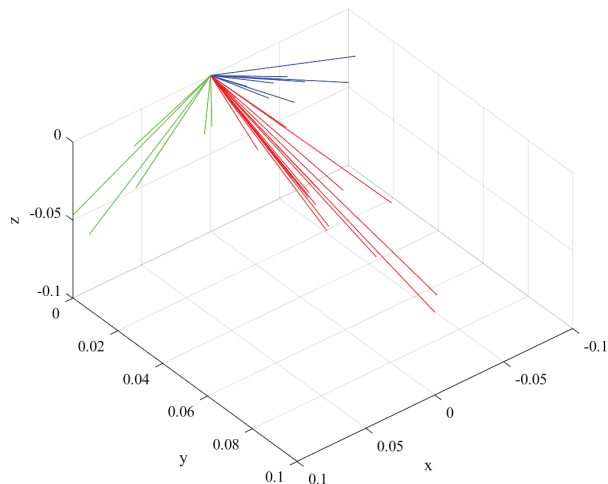


Fig. 6. Clusters for MIMO-MU channel.

pattern in the direction of each transmitting cluster in equal proportion, but will not change the shape of the pattern; At the same time, the increase of beam convergence factor will make the transmission power distribution of each transmitting antenna closer. When the beam convergence factor is large, the capacity will be greatly improved, and the power distribution between antennas is close to average.

**B. Simulation for MIMO-MU**

In the MIMO-MU simulation, there is one sender with 8 antennas and three users with 2 antennas each.

The MIMO-MU channel with 3 users is shown in Fig. 6. There are 15 clusters for each user. The right, middle and left parts of lines represent the propagation clusters pointing to user 1, user 2, and user 3. The lines' direction in the figure represents the angle of the cluster, the length represents the cluster's gain.

The optimal patterns for the first 6 Tx antennas are shown in Fig. 7. The power distribution is shown in Table 2.

The simulation results show that the first six antennas are exactly divided into three groups, each serving

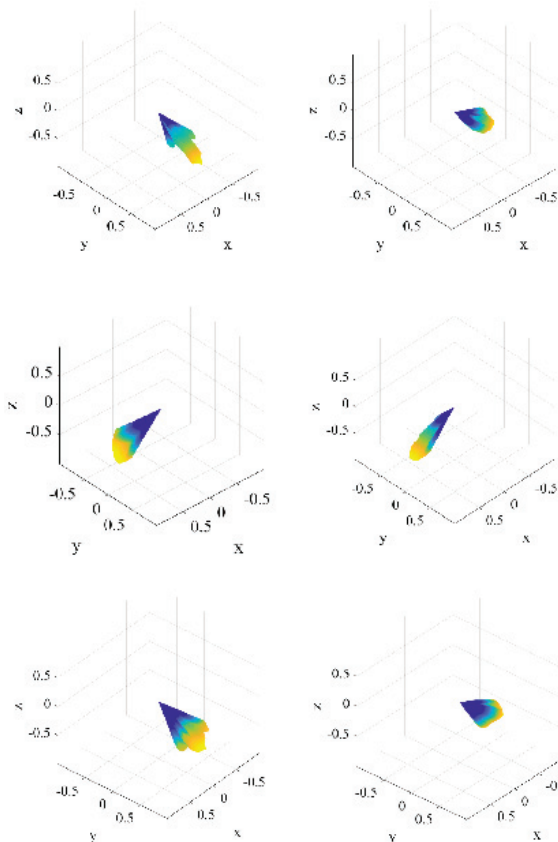


Fig. 7. Optimal patterns for 6 Tx antennas.

Table 2: Power distribution and capacity in MIMO-MU

Beam Convergence Factor	Power Distribution (W)	Capacity(bits/s/Hz)
$\rho=1$	1.9584, 1.8851, 1.8406, 1.7178, 1.6374, 0.9608, 0.0000, 0.0000.	18.0202
$\rho=2$	1.8127, 1.7761, 1.7538, 1.6924, 1.6522, 1.3128, 0.0000, 0.0000.	23.2046
$\rho=3$	1.7642, 1.7398, 1.7250, 1.6837, 1.6568, 1.4306, 0.0000, 0.0000.	26.4202
$\rho=100$	1.6734, 1.6729, 1.6709, 1.6690, 1.6641, 1.6498, 0.0000, 0.0000.	50.2034

one user, and the last two antennas are not used, which is consistent with the analysis in Section III.

## V. CONCLUSION

For the instantaneous MIMO channel based on the spatial cluster model, the product form of the channel coefficient matrix from the environment cluster matrix and transmit antenna pattern matrix has been given. Through piecewise modeling for the transmitting antenna pattern and power constraints, the optimization problem of maximizing the capacity has been solved by using singular value decomposition and the water-filling algorithm. The closed-form of the optimal antenna pattern has been achieved. The simulation results show the solution in this paper is effective.

## REFERENCES

- [1] C. Wang, F. Haider, X. Gao, X. You, Y. Yang, and D. Yuan, "Cellular architecture and key technologies for 5G wireless communication networks," *IEEE Commun. Mag.*, vol. 52, no. 2, pp. 122-130, Feb. 2014.
- [2] Z. Pi and F. Khan, "An introduction to millimeter-wave mobile broadband systems," *IEEE Commun. Mag.*, vol. 49, no. 6, pp. 101-107, Jun. 2011.
- [3] Z. Zhang, Y. Xiao, Z. Ma, M. Xiao, Z. Ding, X. Lei, G. K. Karagininidis, and P. Fan, "6G wireless networks: vision, requirements, architecture, and key technologies," *IEEE Veh. Technol. Mag.*, vol. 14, no. 3, pp. 28-41, Sep. 2019.
- [4] H. Pei, X. Chen, X. Huang, X. Liu, X. Zhang, and Y. Huang, "Key issues and algorithms of multiple-input-multiple-output over-the-air testing in the multi-probe anechoic chamber setup," *Sci. China Inf. Sci.*, vol. 65, no. 3, pp. 47-73, Mar. 2022.
- [5] W. Hong, K.-H. Baek, Y. Lee, Y. Kim, and S.-T. Ko, "Study and prototyping of practically large-scale mmWave antenna systems for 5G cellular devices," *IEEE Commun. Mag.*, vol. 52, no. 9, pp. 63-69, Sep. 2014.
- [6] B. T. Quist and M. A. Jensen, "Optimal antenna pattern design for MIMO systems," *IEEE Antennas and Propagation Society International Symposium*, Honolulu, HI, USA, pp. 1905-1908, 2007.
- [7] D. Evans and M. A. Jensen, "Near-optimal radiation characteristics for diversity antenna design," *IEEE International Workshop on Antenna Technology*, Santa Monica, CA, USA, pp. 1-4, 2009.
- [8] D. N. Evans and M. A. Jensen, "Near-optimal radiation patterns for antenna diversity," *IEEE Trans. Antennas Propag.*, vol. 58, no. 11, pp. 3765-3769, Nov. 2010.
- [9] Y. Wang, X. Chen, H. Pei, W. Sha, H. Yi, and A. A. Kishk, "MIMO performance enhancement of MIMO arrays using PCS-based near-field optimization technique," *Sci. China Inf. Sci.*, in press, doi: 10.1007/s11432-022-3595-y.
- [10] S. Song, Y. Da, B. Qian, X. Huang, X. Chen, Y. Li, and A. A. Kishk, "Dielectric resonator magnetoelectric dipole arrays with low cross polarization, backward radiation, and mutual coupling for MIMO base station applications," *China Commun.*, in press.
- [11] C. Feng, W. Shen, J. An, and L. Hanzo, "Joint hybrid and passive RIS-assisted beamforming for mmWave MIMO systems relying on dynamically configured subarrays," *IEEE IoT Journal*, vol. 9, no. 15, pp. 13913-13926, Aug. 2022.
- [12] Q. Zhu, R. Liu, Y. Liu, M. Li, and Q. Liu, "Joint design of hybrid and reflection beamforming for RIS-aided mmWave MIMO communications," *IEEE Globecom Workshops (GC Wkshps)*, Madrid, Spain, pp. 1-6, 2021.
- [13] R. Deng, B. Di, H. Zhang, Y. Tan, and L. Song, "Reconfigurable holographic surface-enabled multi-user wireless communications: Amplitude-controlled holographic beamforming," *IEEE Trans. Wireless Commun.*, vol. 21, no. 8, pp. 6003-6017, Aug. 2022.
- [14] R. Deng, B. Di, H. Zhang, and L. Song, "HDMA: holographic-pattern division multiple access," *IEEE J. Sel. Areas Commun.*, vol. 40, no. 4, pp. 1317-1332, Apr. 2022.
- [15] C.-H. Hsu, "Optimizing uplink beam pattern of smart antenna by phase-amplitude disturbance in a linear array," *IEEE Antennas and Propagation Society Symposium, 2004*, Monterey, CA, USA, vol. 3, pp. 2827-2830, 2004.
- [16] S. Ma, H. Li, A. Cao, J. Tan, and J. Zhou, "Pattern synthesis of the distributed array based on the hybrid algorithm of particle swarm optimization and convex optimization," *11th International Conference on Natural Computation (ICNC)*, Zhangji-ajie, pp. 1230-1234, 2015.
- [17] E. R. Schlosser, S. M. Tolfo, and M. V. T. Heckler, "Particle swarm optimization for antenna arrays synthesis," *SBMO/IEEE MTT-S International Microwave and Optoelectronics Conference (IMOC)*, Porto de Galinhas, Brazil, pp. 1-6, 2015.
- [18] A. Smida, R. Ghayoula, H. Trabelsi, and A. Gharsallah, "Adaptive radiation pattern optimization for antenna arrays by phase using a Taguchi Optimization method," *11th Mediterranean Microwave Symposium (MMS)*, Yasmine Hammamet, Tunisia, pp. 138-141, 2011.
- [19] A. Smida, R. Ghayoula, and A. Gharsallah, "Beamforming multibeam antenna array using Taguchi Optimization method," *2nd World Symposium on Web Applications and Networking (WSWAN)*, Sousse, Tunisia, pp. 1-4, 2015.

- [20] W. Shi, X. Liu, and Y. Li, "ULA fitting for MIMO radar," *IEEE Commun. Lett.*, vol. 26, no. 9, pp. 2190-2194, Sep. 2020.
- [21] S. Luo, Y. Li, T. Jiang, and B. Li, "FSS and meta-material based low mutual coupling MIMO antenna array," *IEEE International Symposium on Antennas and Propagation and USNC-URSI Radio Science Meeting*, Atlanta, GA, pp. 725-726, 2019.
- [22] 3GPP. TR 38.901 V16.1.0, "5G; Study on channel model for frequencies from 0.5 to 100 GHz," Nov. 2020.
- [23] X. Chen, M. Zhao, H. Huang, Y. Wang, S. Zhu, C. Zhang, J. Yi, and A. A. Kishk, "Simultaneous decoupling and decorrelation scheme of MIMO arrays," *IEEE Trans. Veh. Technol.*, vol. 71, no. 2, pp. 2164-2169, Feb. 2022.
- [24] Y. Wang, X. Chen, X. Liu, J. Yi, J. Chen, A. Zhang, and A. A. Kishk, "Improvement of diversity and capacity of MIMO system using scatterer array," *IEEE Trans. Antennas Propag.*, vol. 70, no. 1, pp. 789-794, Jan. 2022.
- [25] J. R. Hampton, *Introduction to MIMO Communications*, Cambridge University Press, Cambridge, UK, 2013.



**Cuicui Zhang** received her B.S. and M.S. degrees in Information and Communications Engineering from Xi'an Jiaotong University, Xi'an, China, in 2010 and 2013. She is currently pursuing a Ph.D. degree in Electronics Science and Technology from Xi'an Jiaotong University, Xi'an, China. Her research interest is antenna design for 5G/6G MIMO systems.



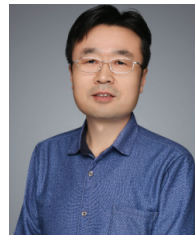
**Shuo Wang** received his B.S. degree in Information Engineering from Xi'an Jiaotong University, Xi'an, China, in 2020. He is currently studying for an M.S. degree at the School of Information and Communications Engineering from Xi'an Jiaotong University, Xi'an, China. His research interest is communication algorithms related to reconfigurable antennas for 5G MIMO systems.



**Ming Zhang** received his B.S. and M.S. degrees in Information and Communications Engineering, and his Ph.D. degree in Electronic Science and Technology, all from Xi'an Jiaotong University, Xi'an, China, in 2008, 2011, and 2017, respectively. From 2011 to 2014, he was with Huawei Technologies Co., Ltd., Xi'an, China. He is currently an associate professor at Xi'an Jiaotong University. His research interests include array signal processing and numerical optimization.



**Xiaobo Liu** (Member, IEEE) was born in Baoji, China, in 1992. He received his B.Eng. degree in Information Engineering and his Ph.D. degree in Electronic Science and Technology from Xi'an Jiaotong University, Xi'an, China, in 2014 and 2018, respectively. Since 2019, he has been a Research Associate at Xi'an Jiaotong University. He has authored or coauthored more than 20 articles in international and domestic journals and conferences. His research interests include electromagnetic fields and microwave theory, computational electromagnetics, metasurface, antenna design, and microwave circuits.



**Anxue Zhang** received his B.S. degree in Electrical Engineering from Henan Normal University, Henan, China, in 1996, and M.S. and Ph.D. degrees in Electrical Engineering from Xi'an Jiaotong University, Xi'an, China, in 1999 and 2003, respectively. He is currently a professor and director of the Institute of Electromagnetics and Information Technology of Xi'an Jiaotong University. He is also a member of the Academic Committee of the Key Laboratory of Ultra-High Speed Circuit Design and Electromagnetic Compatibility at the Ministry of Education. His research areas include antenna and electromagnetic wave propagation, RF and microwave circuit design, and metamaterials. He has coauthored one book, and more than 300 journal papers on these topics.

# Isolation Improvement Using the Field-Circuit Combined Method for In-Band Full-Duplex MIMO Antenna Arrays

Yiran Da, Jianjia Yi, Jianxing Li, and Xiaoming Chen

School of Information and Communications Engineering  
Xi'an Jiaotong University, Xi'an, 710049, China  
dyr916@stu.xjtu.edu.cn, xiaoming.chen@mail.xjtu.edu.cn

**Abstract** – This paper proposes a field-circuit combined decoupling method for co-polarized in-band full-duplex multiple-input multiple-output (MIMO) antenna arrays. The proposed field-circuit combined method is composed of decoupling network and neutralization-based decoupling. An in-band full-duplex antenna with high isolation and low cross-polarization level is designed and extended to a  $1 \times 4$  linear array. The decoupling network and ADS are applied for the array to alleviate the mutual coupling by rebuilding the neutralization wave paths in the circuit and field domains. Thus, low coupling ( $< -25$  dB) among the transmitting/receiving antennas and high isolation ( $> 47$  dB) between the transmitting and receiving antennas are achieved at 2.6 GHz, exhibiting a superior decoupling performance.

**Index Terms** – antenna array, decoupling, field-circuit combined, in-band full-duplex.

## I. INTRODUCTION

With the increasing demand for wireless communication systems, full-duplex communication was developed for higher spectrum efficiency [1, 2]. In-band full-duplex antennas have been studied for base station applications [3, 4], which can transmit and receive signals simultaneously in the same frequency band. When full-duplex antennas are used in MIMO antenna arrays, the antenna elements are closely arranged due to the limited space. Signal interference is generated between the receiving and transmitting antennas, and mutual coupling is generated between the receiving/transmitting antennas, which significantly deteriorate the performances of the wireless communication systems (including receiver performance, error rate, dynamic range, and channel capacity) [5–7]. Notably, 100 dB isolation between the transmitter and receiver is generally required for full-duplex systems, which is usually achieved by combining the antenna, analog and digital domains [8, 9]. Therefore, the isolation at antenna level should be improved as much as possible to reduce the order of the analog radio

frequency filters, thus facilitating the subsequent design of the communication system. Furthermore, mutual coupling (among the transmitting/receiving antennas) below  $-25$  dB is sufficient for MIMO arrays.

Various methods have been studied for suppressing the mutual couplings. The first type is the field domain decoupling method, which is classified into two categories of partition and neutralization. Decoupling resonator [10, 11], defected ground [12], and meta-material structures [13, 14] are based on the partition principle. Neutralization approaches cancel the original coupling waves between antennas by rebuilding the additional wave paths with equal amplitude and opposite phase, such as decoupling grounds [15, 16], array antenna decoupling surface (ADS) [17], dielectric superstrate [18] and planar path [19]. The second type is the circuit domain decoupling method. Decoupling networks [20–22] construct the coupling signals through the feeding network in the circuit domain, which cancel out with the original coupling signals between the antennas. These methods can effectively improve the isolation; however, they are usually used for conventional antenna arrays rather than full-duplex antenna arrays. When considering full-duplex operation, the isolation between the transmitting and receiving antennas is important. In the full-duplex antenna array proposed in [23], only 30 dB isolation can be obtained. After increasing the antenna spacing, higher isolation ( $> 42$  dB) is obtained in [24]. In [25, 26], the interference between the transmitter and receiver is suppressed by integrating with the feeding network based on antiphase feeding technique. However, the transmitting and receiving antennas have orthogonal polarizations in above arrays [23–26], which is not applicable for some scenarios.

In this paper, a field-circuit combined decoupling method is proposed for co-polarized in-band full-duplex MIMO arrays. The proposed decoupling method consisting of the decoupling network and the ADS could construct the neutralization wave paths from circuit and field perspectives, respectively. An in-band full-duplex antenna with high isolation and low cross-polarization

Table 1: Performance comparison of full-duplex antenna arrays

Ref.	Pol.	Ant. Dis. ( $\lambda$ )	Isolation (TX/RX-RX/TX)	Coupling (TX/RX-TX/RX)
[23]	cross-pol.	0.57	> 30 dB	< -20 dB
[24]	cross-pol.	0.67	> 42 dB	< -25 dB
[25]	cross-pol.	0.50	> 50 dB	-
This work	co-pol.	0.56	> 47 dB	< -25 dB

level is designed and formed into a  $1 \times 4$  linear array with the spacing of  $0.56\lambda$  (where  $\lambda$  is the free-space wavelength at the working frequency). The decoupling network could alleviate the couplings between different antennas and the ADS could enhance the isolation in a single antenna. The  $1 \times 4$  full-duplex antenna array with the field-circuit combined decoupling method is fabricated and measured. At the working frequency of 2.6 GHz, both low coupling (< -25 dB) among the transmitting/receiving antennas and high isolation (> 47 dB) between the transmitting and receiving antennas are achieved. The performances of in-band full-duplex antenna arrays are compared in Table 1.

## II. FULL-DUPLEX ANTENNA ELEMENT

The configuration of the in-band full-duplex antenna is shown in Fig. 1, which is composed of a rectangular patch, four open-ended stubs, a fence-strip resonator (FSR), a metallic ground, and two dielectric layers. The dielectric substrates are made of F4B with a dielectric constant of 2.2 and a loss tangent of 0.001. The metallic strip is printed on the bottom side of the dielectric 1, and the patch and open-ended stubs are printed on the top side. The patch and strip are connected by series of metallic vias. The FSR structure consisting of metallic vias and strip is utilized to enhance the isolation between the TX and RX ports [4]. Two pairs of open-ended stubs are loaded to reduce the H-plane cross-polarizations of the shorted patch antennas [27]. Besides, the dimension of the antenna is reduced by using the rectangular slots on the patch. The TX and RX ports are excited by the symmetrical metallic probes, exhibiting the same linearly polarizations. The parameters of the antenna are listed in the caption of Fig. 1.

Figure 2 shows the simulated S-parameters of the full-duplex antenna. The reflection coefficients ( $S_{11}$  and  $S_{22}$ ) are lower than -10 dB, and the port isolation is above 30 dB at around 2.6 GHz. The simulated E-plane and H-plane radiation patterns for the TX and RX ports of the full-duplex antenna are shown in Fig. 3. As observed, the H-plane cross-polarization levels for both

ports maintain below -19.8 dB, and the satisfactory broadside radiated patterns are achieved.

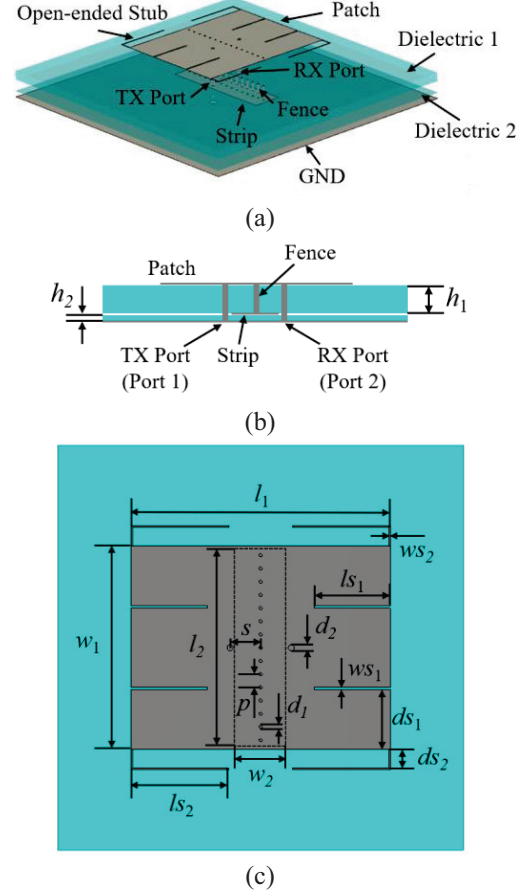


Fig. 1. Configuration of the full-duplex antenna. (a) Perspective view. (b) Side view. (c) Top view. The optimized parameters are:  $h_1 = 3$ ,  $h_2 = 0.165$ ,  $l_1 = 50$ ,  $l_2 = 40$ ,  $w_1 = 39$ ,  $w_2 = 10.4$ ,  $l_{s1} = 12.6$ ,  $l_{s2} = 19.2$ ,  $w_{s1} = 0.5$ ,  $w_{s2} = 0.3$ ,  $d_{s1} = 11.25$ ,  $d_{s2} = 4$ ,  $d_1 = 0.6$ ,  $d_2 = 1$ ,  $s = 6$ ,  $p = 2.6$  (all dimensions in mm).

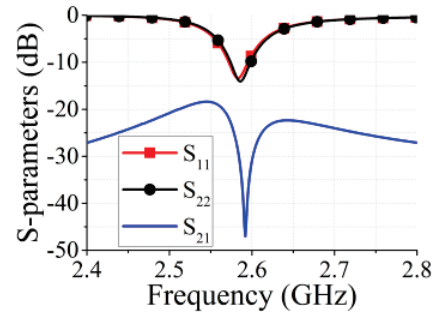


Fig. 2. Simulated S-parameters of the full-duplex antenna.

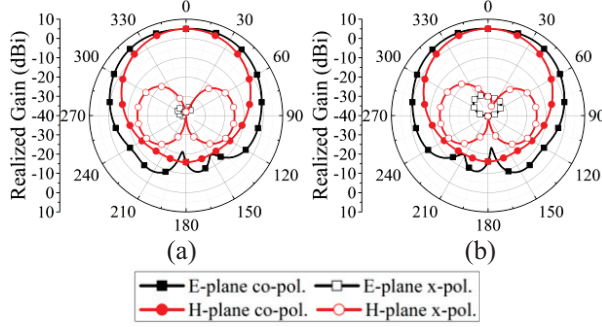


Fig. 3. Simulated radiation patterns of the full-duplex antenna at 2.58 GHz. (a) TX port. (b) RX port.

### III. FULL-DUPLEX ANTENNA ARRAY WITH FIELD-CIRCUIT COMBINED METHOD

#### A. Field-circuit combined method

The co-polarized in-band full-duplex antenna is expanded to a  $1 \times 4$  linear array with the element separation of 65 mm ( $0.56\lambda$ ), as shown in Fig. 4 (a). In such an array, both the coupling among transmitting/receiving antennas (e.g.,  $S_{13}$ ,  $S_{53}$ , and  $S_{73}$ ) and the isolation between transmitting and receiving antennas (e.g.,  $1/S_{23}$ ,  $1/S_{43}$ ,  $1/S_{63}$ , and  $1/S_{83}$ ) need to be considered. Figure 4 (b) shows the perspective view of the  $1 \times 4$  full-duplex antenna array with decoupling network, and the bottom view is shown in Fig. 4 (c). The microstrip transmission lines are printed on the bottom side of the dielectric substrate (made of 0.508 mm-thick Rogers RO4350B substrate with  $\epsilon_r = 3.66$  and  $\tan\delta = 0.0037$ ) below the ground layer. The apertures are etched on the metallic ground and placed below the patches' edges. Figure 4 (d) presents the array with decoupling network and ADS. The ADS is composed of a 1 mm-thick FR4 dielectric substrate (with  $\epsilon_r = 4.4$  and  $\tan\delta = 0.02$ ) and four rectangular metal radiator patches, which is arranged above the antenna array with a height of 3 mm. The final dimensions of the array and the decoupling structures are listed in the caption of Fig. 4.

The microstrip decoupling network at the feeding layer is provided for the linear array, as shown in Figs. 4 (b) and (c). The additional coupling wave from the feeding line of antenna element to adjacent antenna is generated by loading the apertures on the feeding lines [22]. The aperture coupling between the transmitting/receiving port and the adjacent transmitting or receiving port in different antenna is introduced from the circuit perspective, which is controlled by the size of the aperture. Since the apertures and feeding points of the radiating patches are connected by the feeding lines, the length and width of the microstrip transmission lines also need to be considered when decoupling. Therefore,

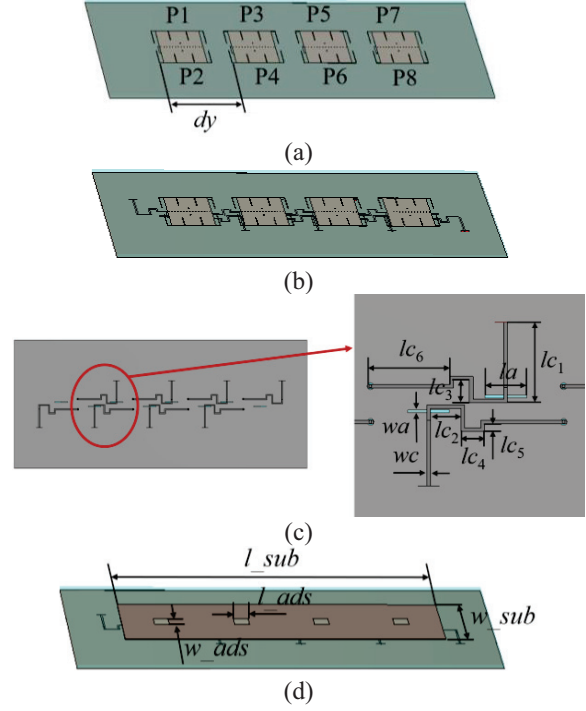


Fig. 4. Configuration of the  $1 \times 4$  full-duplex antenna array with/without the decoupling structures (decoupling network and ADS). (a) Perspective view of the array without decoupling structures (Array 1). (b) Perspective view of the array with decoupling network (Array 2). (c) Perspective view of the array with decoupling network and ADS (Array 3). (d) Bottom view of Array 3. The optimized dimensions are:  $dy = 65$ ,  $l_{sub} = 260$ ,  $w_{sub} = 65$ ,  $l_{ads} = 12$ ,  $w_{ads} = 12$ ,  $la = 14$ ,  $wa = 1$ ,  $lc_1 = 27.1$ ,  $lc_2 = 12.8$ ,  $lc_3 = 7.7$ ,  $lc_4 = 7.8$ ,  $lc_5 = 2.7$ ,  $lc_6 = 28.9$ ,  $wc = 1.2$  (all dimensions in mm).

the original couplings among different antenna elements can be neutralized by utilizing the aperture-loaded decoupling network.

Figure 5 shows the simulated S-parameters of the  $1 \times 4$  full-duplex antenna array with and without the decoupling network. Due to the page limit, only the S-parameters of the middle element of the array are shown here. As observed, after applying the decoupling network, the mutual couplings among neighboring transmitting/receiving antennas are effectively reduced from  $-19$  to  $-25$  dB or lower (see  $S_{13}$ ,  $S_{53}$ , and  $S_{73}$  in Fig. 5 (a)), while the isolations of the transmitting and receiving ports in different antennas ( $1/S_{23}$ ,  $1/S_{63}$ , and  $1/S_{83}$ ) are improved by around 12 dB (from 35 to 47 dB) at the working frequency of 2.6 GHz. The reflection coefficient of the antenna ( $S_{33}$ ) maintains below  $-10$  dB, and the isolation between the transmitting and receiving ports in a single antenna ( $1/S_{43}$ ) maintains above 30 dB.

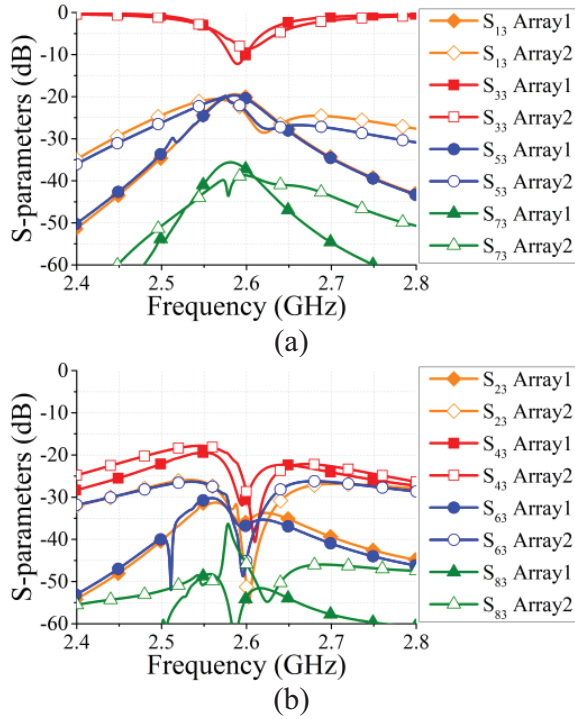


Fig. 5. Simulated S-parameters of the  $1 \times 4$  full-duplex antenna array with/without the decoupling network. (a)  $S_{13}$ ,  $S_{33}$ ,  $S_{53}$ , and  $S_{73}$ . (b)  $S_{23}$ ,  $S_{43}$ ,  $S_{63}$ , and  $S_{83}$ .

Thus, the decoupling networks can significantly suppress the couplings among different antennas, but have little effect on the port isolation in a single antenna. To improve the isolation between the transmitting and receiving ports in a single antenna, the ADS structure is employed for the array with the decoupling network, as electromagnetic waves radiated by the transmitting antenna are reflected by the metal reflector and received by the receiving antenna in the same element, forming an additional coupling wave path from the field perspective [17]. The amplitude and phase of the additional wave path are determined by the height and the size of the metal reflectors. Thus, the original coupling between transmitting and receiving ports in a single antenna can be counteracted by employing the ADS.

Figure 6 shows the simulated S-parameters of the  $1 \times 4$  full-duplex antenna array with and without the decoupling network and ADS. It is obvious that, with the decoupling network and ADS, the isolation between the transmitting and receiving ports in a single antenna is significantly improved from 30 to 50 dB at the working frequency of 2.6 GHz (see  $1/S_{43}$  in Fig. 6 (a)). The couplings among neighboring transmitting/receiving antennas ( $S_{13}$ ,  $S_{53}$ , and  $S_{73}$ ) remain below  $-25$  dB, while the isolations of the transmitting and receiving ports in different antennas ( $1/S_{23}$ ,  $1/S_{63}$ , and  $1/S_{83}$ ) remain larger

than 47 dB. Meanwhile, the reflection coefficient of the antenna ( $S_{33}$ ) continues below  $-10$  dB. Therefore, after loading the ADS structure, the isolation between the transmitting and receiving ports in a single antenna is effectively enhanced while maintaining the other high isolations between different antennas. Figure 7 presents the simulated normalized E-plane and H-plane radiation patterns of TX port (P3) with and without the decoupling network and ADS. As can be seen, the radiation patterns

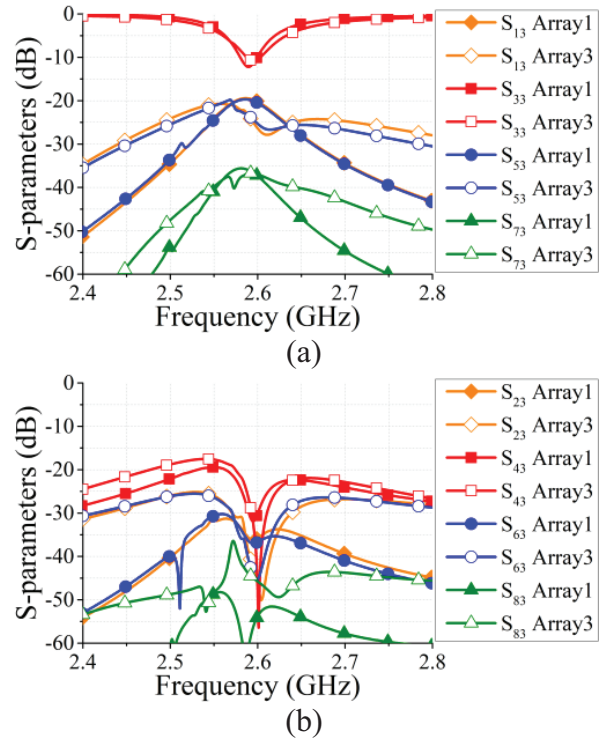


Fig. 6. Simulated S-parameters of the  $1 \times 4$  full-duplex antenna array with/without the decoupling network and ADS. (a)  $S_{13}$ ,  $S_{33}$ ,  $S_{53}$ , and  $S_{73}$ . (b)  $S_{23}$ ,  $S_{43}$ ,  $S_{63}$ , and  $S_{83}$ .

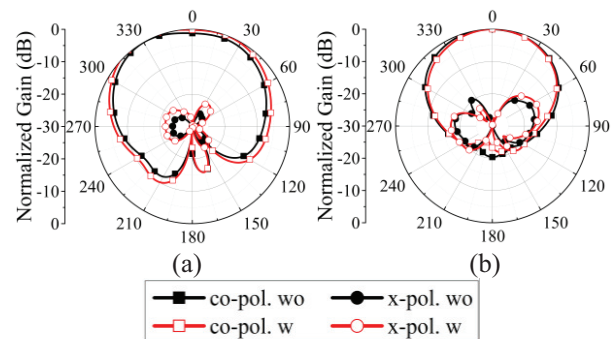


Fig. 7. Simulated normalized radiation patterns of TX port (P3) with/without the decoupling network and ADS. (a) E-plane. (b) H-plane.

with the decoupling network and ADS are comparable to the original patterns, exhibiting low cross-polarization level ( $< -14.5$  dB) and satisfactory radiation performances.

It is concluded that all the isolations of the co-polarized in-band full-duplex antenna array can be significantly enhanced by employing the decoupling network and ADS. The proposed field-circuit combined decoupling method combines the circuit domain decoupling network and the field domain ADS structure to simultaneously obtain lower coupling between the transmitting/receiving antennas and higher isolation between transmitting and receiving antennas.

**B. Measurement results**

Figure 8 shows the prototype photos of the  $1 \times 4$  full-duplex antenna array with the field-circuit combined method. The decoupling network and the ADS structure are employed in the array. The ADS and the substrate layers are fixed together using Nylon screws.

The simulated and measured S-parameters of the  $1 \times 4$  full-duplex antenna array using the field-circuit combined method are presented in Fig. 9. It is clear that, at the working frequency of 2.6 GHz, the coupling between the transmitting/receiving antennas is about  $-25$  dB or lower, while the coupling between the transmitting and receiving antennas is lower than  $-47$  dB. The measurement results are comparable to the simulation results. The small discrepancies are caused by imperfect soldering, manufacturing tolerance, and measurement errors. Figure 10 shows the simulated and measured E-plane and H-plane radiation patterns of TX port (P3) using the field-circuit combined method. Low cross-polarization level ( $< -14.5$  dB) and satisfactory radiation perfor-

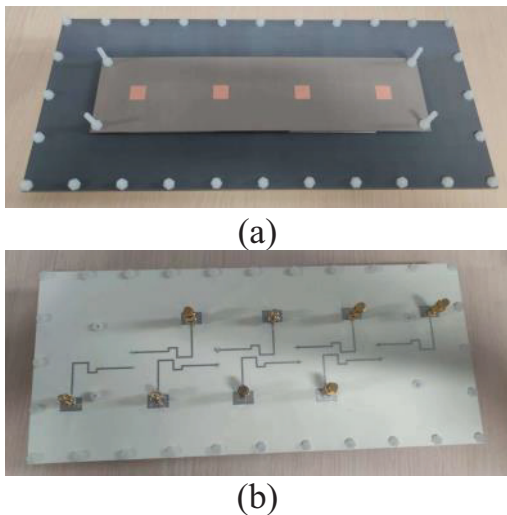


Fig. 8. Photographs of the prototype. (a) Top view. (b) Bottom view.

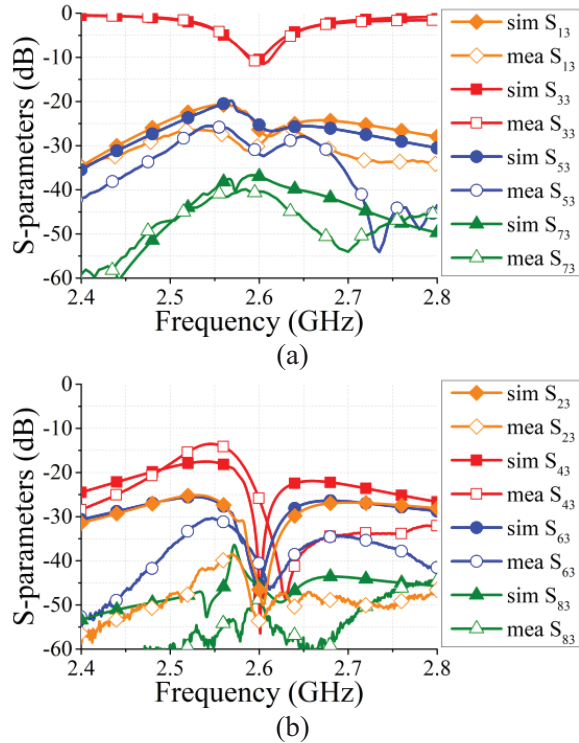


Fig. 9. Simulated and measured S-parameters of the  $1 \times 4$  full-duplex antenna array using the field-circuit combined method (decoupling network and ADS). (a)  $S_{13}$ ,  $S_{33}$ ,  $S_{53}$ , and  $S_{73}$ . (b)  $S_{23}$ ,  $S_{43}$ ,  $S_{63}$ , and  $S_{83}$ .

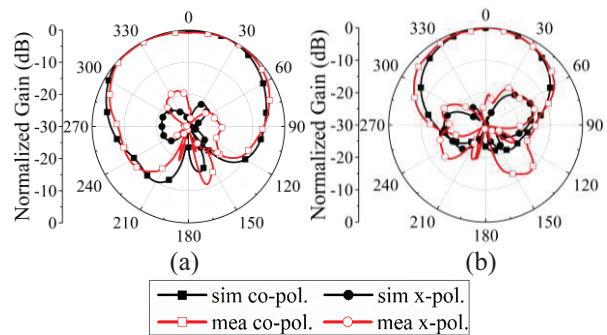


Fig. 10. Simulated and measured radiation patterns of TX port (P3) using the field-circuit combined method (decoupling network and ADS). (a) E-plane. (b) H-plane.

mances are obtained. Meanwhile, the simulated and measured radiation patterns are in good agreement.

**IV. CONCLUSION**

A field-circuit combined decoupling method consisting of the decoupling network and ADS was presented in this paper. The additional coupling waves in the circuit and field domains were generated to cancel the original couplings. An in-band full-duplex

antenna with the same polarization was designed and formed into a  $1 \times 4$  linear array. The coupling between different antennas could be suppressed by the decoupling network, and the isolation in a single antenna could be enhanced by the ADS. The  $1 \times 4$  array, together with the decoupling network and the ADS, have been manufactured and experimented. The simulated and measured results were in reasonable consistent. Low coupling ( $< -25$  dB) among the transmitting/receiving antennas and high isolation ( $> 47$  dB) between the transmitting and receiving antennas were achieved at 2.6 GHz. Therefore, the proposed field-circuit combined decoupling method could be used for enhancing the isolations of co-polarized in-band full-duplex MIMO arrays.

### ACKNOWLEDGMENT

This work was supported by the National Key Research and Development Program of China under Grant 2022YFB3902400.

### REFERENCES

- [1] A. Sabharwal, P. Schniter, D. Guo, D. W. Bliss, S. Rangarajan, and R. Wichman, "In-band full-duplex wireless: Challenges and opportunities," *IEEE J. Sel. Areas Commun.*, vol. 32, no. 9, pp. 1637-1652, Sep. 2014.
- [2] D. Kim, H. Lee, and D. Hong, "A survey of in-band full-duplex transmission: From the perspective of PHY and MAC layers," *IEEE Commun. Surv. Tuts.*, vol. 17, no. 4, pp. 2017-2046, 2015.
- [3] W. Zhang, J. Hu, Y. Li, and Z. Zhang, "Design of a stacked co-polarized full-duplex antenna with broadside radiation," *IEEE Trans. Antennas Propag.*, vol. 69, no. 11, pp. 7111-7118, Nov. 2021.
- [4] Y. He and Y. Li, "Compact co-linearly polarized microstrip antenna with fence-strip resonator loading for in-band full-duplex Systems," *IEEE Trans. Antenn. Propag.*, vol. 69, no. 11, pp. 7125-7133, Nov. 2021.
- [5] J. H. Zhang, F. M. He, W. Li, and Y. Li, "Self-interference cancellation: A comprehensive review from circuits and fields perspectives," *Electron.*, vol. 11, no. 2, pp. 172, Jan. 2022.
- [6] F. Peng, F. Yang, B. Liu, and X. Chen, "Experimental investigation of decoupling effect on the nonlinearity of power amplifiers in transmitter array," *Applied Computational Electromagnetics Society (ACES) Journal*, in press.
- [7] X. Chen, S. Zhang, and Q. Li, "A review of mutual coupling in MIMO systems," *IEEE Access*, vol. 6, pp. 24706-24719, Apr. 2018.
- [8] Z. Zhang, K. Long, A. V. Vasilakos, and L. Hanzo, "Full-duplex wireless communications: challenges, solutions, and future research directions," *Proc. IEEE*, vol. 104, no. 7, pp. 1369-1409, Jul. 2016.
- [9] S. B. Venkatakrishnan, A. Hovsepian, A. D. Johnson, T. Nakatani, E. A. Alwan, and J. L. Volakis, "Techniques for achieving high isolation in RF domain for simultaneous transmit and receive," *IEEE Open J. Antennas Propag.*, vol. 1, pp. 358-367, Jul. 2020.
- [10] M. Li, X. Chen, A. Zhang, W. Fan, and A. A. Kishk, "Split-ring resonator-loaded baffles for decoupling of dual-polarized base station array," *IEEE Antennas Wirel. Propag. Lett.*, vol. 19, no. 10, pp. 1828-1832, Oct. 2020.
- [11] F. Faraz, X. Chen, Q. Li, J. Tang, J. Li, T. A. Khan, and X. Zhang, "Mutual coupling reduction of dual polarized low profile MIMO antenna using decoupling resonators," *Applied Computational Electromagnetics Society (ACES) Journal*, vol. 35, no. 1, pp. 38-43, Jan. 2020.
- [12] B. Qian, X. Chen, and A. A. Kishk, "Decoupling of microstrip antennas with defected ground structure using the common/differential mode theory," *IEEE Antennas Wirel. Propag. Lett.*, vol. 20, no. 5, pp. 828-832, May 2021.
- [13] K. Yu, Y. Li, and X. Liu, "Mutual coupling reduction of a MIMO antenna array using 3-D novel meta-material structures," *Applied Computational Electromagnetics Society (ACES) Journal*, vol. 33, no. 7, pp. 758-763, Jul. 2018.
- [14] S. Luo, Y. Li, Y. Xia, and L. Zhang, "A low mutual coupling antenna array with gain enhancement using metamaterial loading and neutralization line structure," *Applied Computational Electromagnetics Society (ACES) Journal*, vol. 34, no. 3, pp. 411-418, Mar. 2019.
- [15] S. Zhang, X. Chen, and G. F. Pedersen, "Mutual coupling suppression with decoupling ground for massive MIMO antenna arrays," *IEEE Trans. Veh. Technol.*, vol. 68, no. 8, pp. 7273-7282, Aug. 2019.
- [16] S. Song, X. Chen, Y. Da, and A. A. Kishk, "Broadband dielectric resonator antenna array with enhancement of isolation and front-to-back ratio for MIMO application," *IEEE Antennas Wirel. Propag. Lett.*, vol. 21, no. 7, pp. 1487-1491, Jul. 2022.
- [17] K. Wu, C. Wei, X. Mei, and Z. Y. Zhang, "Array-antenna decoupling surface," *IEEE Trans. Antennas Propag.*, vol. 65, no. 12, pp. 6728-6738, Dec. 2017.

- [18] Y. Da, Z. Zhang, X. Chen, and A. A. Kishk, "Mutual coupling reduction with dielectric superstrate for base station arrays," *IEEE Antennas Wirel. Propag. Lett.*, vol. 20, no. 5, pp. 843-847, May 2021.
- [19] L. Gu, W. Yang, S. Liao, Q. Xue, and W. Che, "Novel coupling cancellation method by loading planar path for wideband high-isolation wide-scanning millimeter-wave phased array," *IEEE Trans. Antennas Propag.*, vol. 70, no. 11, pp. 10520-10530, Nov. 2022.
- [20] T. Dong and K. K. M. Cheng, "Compact antenna array with newly designed decoupling network," *Applied Computational Electromagnetics Society (ACES) Journal*, vol. 33, no. 11, pp. 1196-1200, Nov. 2018.
- [21] X. J. Zou, G. M. Wang, Y. W. Wang, and H.-P. Li, "An efficient decoupling network between feeding points for multielement linear arrays," *IEEE Trans. Antennas Propag.*, vol. 67, no. 5, pp. 3101-3108, May 2019.
- [22] Y. M. Zhang and S. Zhang, "A novel aperture-loaded decoupling concept for patch antenna arrays," *IEEE Trans. Microw. Theory Techn.*, vol. 69, no. 9, pp. 4272-4283, Sep. 2021.
- [23] M. V. Kuznetsov, S. K. Podilchak, A. J. McDermott, and M. Sellathurai, "Dual-polarized high-isolation antenna design and beam steering array enabling full-duplex communications for operation over a wide frequency range," *IEEE Open J. Antennas Propag.*, vol. 2, pp. 521-532, Mar. 2021.
- [24] M. V. Kuznetsov, S. K. Podilchak, A. J. McDermott, and M. Sellathurai, "Dual-polarized antenna with dual-differential integrated feeding for wideband full-duplex systems," *IEEE Trans. Antennas Propag.*, vol. 69, no. 11, pp. 7192-7201, Nov. 2021.
- [25] Y. M. Zhang, S. Zhang, J. L. Li, and G. F. Pedersen, "A dual-polarized linear antenna array with improved isolation using a slotline-based 180° hybrid for full-duplex applications," *IEEE Antennas Wirel. Propag. Lett.*, vol. 18, no. 2, pp. 348-352, Feb. 2019.
- [26] D. Wójcik, M. Surma, A. Noga, and M. Magnuski, "High port-to-port isolation dual-polarized antenna array dedicated for full-duplex base stations," *IEEE Antennas Wirel. Propag. Lett.*, vol. 19, no. 7, pp. 1098-1102, Jul. 2020.
- [27] N. W. Liu, L. Zhu, Z. X. Liu, Z. Y. Zhang, G. Fu, and Y. Liu, "Cross-polarization reduction of a shorted patch antenna with broadside radiation

using a pair of open-ended stubs," *IEEE Trans. Antennas Propag.*, vol. 68, no. 1, pp. 13-20, Jan. 2020.



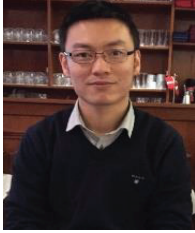
**Yiran Da** received the B.S. degree in Information Engineering from Xi'an Jiaotong University, Xi'an, China, in 2020, where she is currently pursuing the M.S. degree. Her research interests include base station antenna design and mutual coupling reduction.



**Jianjia Yi** (Member, IEEE) received the B.S. degree in Electrical Engineering from the Harbin Institute of Technology, Harbin, China, in 2009, the M.S. degree in Telecommunication Engineering from Politecnico di Torino, Turin, Italy, in 2012, and the Ph.D. degree in Physics from University Paris Saclay, Paris, France, in 2015. From 2016 to 2019, he was an Associate Professor with the State Key Laboratory of Integrated Services Networks, School of Telecommunications Engineering, Xi'dian University, Xi'an, China. He is currently an Associate Professor with Xi'an Jiaotong University, Xi'an. He has coauthored two book chapters and more than 60 articles in peer-reviewed international journals and conference proceedings. His research interests include theoretical and computational electromagnetics with applications to antenna theory and design, antennas, frequency-selective surfaces, transmitarray, and metagratings.



**Jianxing Li** (S'15-M'18) received the B.S. degree in Information and Communications Engineering, and the M.S. and Ph.D. degrees in Electromagnetic Field and Microwave Techniques, all from Xi'an Jiaotong University, Xi'an, China, in 2008, 2011, and 2016, respectively. From 2014 to 2016, he was a visiting researcher with the Department of Electrical and Computer Engineering, Duke University, Durham, NC, USA. He is currently an associate professor at Xi'an Jiaotong University. His research interests include microwave and mmWave circuits and antennas, wireless power transfer, and multi-functional mmWave antennas.



**Xiaoming Chen** (M'16–SM'19) received the B.Sc. degree in electrical engineering from Northwestern Polytechnical University, Xi'an, China, in 2006, and M.Sc. and PhD degrees in electrical engineering from Chalmers University of Technology, Gothenburg, Sweden, in 2007 and 2012, respectively. From 2013 to 2014, he was a postdoctoral researcher at the same University. From 2014 to 2017, he was with Qamcom Research & Technology AB, Gothenburg, Sweden. Since 2017, he has been a professor at Xi'an Jiaotong University, Xi'an, China. His research areas include MIMO antennas, over-the-air testing, reverberation chambers, and hardware impairments and mitigation. Prof. Chen serves as a Senior Associate Editor (AE) for IEEE Antennas and Wireless Propagation Letters and received the Outstanding AE Awards in 2018, 2019, 2020, and 2021. He received the URSI (International Union of Radio Science) Young Scientist Awards in 2017 and 2018.

# Wideband Decoupled 8-Element MIMO Mobile Phone Antenna for Sub-6GHz 5G NR Bands

Jiagang He, Shichao Zhu, Jie Yu, Hao Li, and Gaosheng Li

College of Electrical and Information Engineering  
Hunan University, Changsha, 410082, China  
Gaosheng7070@vip.163.com

**Abstract** – A broadband decoupled dual antenna pair suitable for sub-6G mobile terminal application is proposed and designed. The multiple input multiple output (MIMO) antenna pair is arranged on the metal frame of the mobile phone, with two antenna pairs on each metal frame. The slotted antenna element structure and defect ground decoupling structure are used to achieve wide band and high isolation. Based on the decoupled antenna pair, an eight-element MIMO antenna is designed. Similarly, the coupling between antenna pairs is effectively reduced by etching the decoupled defect structure of a zigzag shape on the system surface. The prototype of the antenna array is successfully fabricated and tested. Simulation and experimental results show that the proposed eight-element MIMO antenna can fully cover the n77/n78/n79 band of 5G New Radio and 5 GHz band of WLAN. The overall efficiency of the antenna is 50%-75%, the envelope correlation coefficient (ECC) is below 0.08, and the isolation between any two ports is better than 11 dB.

**Index Terms** – 5G New Radio (5G NR), metal-frame smartphone, multiple-input-multiple-output (MIMO) antenna, slot antenna, WLAN 5 GHz band.

## I. INTRODUCTION

Multiple input multiple output (MIMO) technology, as one of the core technologies of future fifth generation (5G) communication systems, can significantly improve spectral efficiency without increasing power and spectrum. Therefore, it is widely used in the design of terminal antennas to improve performance and adapt to 5G communication. The fourth generation (4G) mobile communication system, also known as LTE (Long Term Evolution), introduces MIMO technology to improve the transceiver efficiency of wireless mobile communication networks, and can effectively improve channel capacity and spectrum efficiency. As (5G) mobile communications enter the commercial phase, there will be greater data capacity, higher data transmission rates and lower

delays. In order to achieve these difficult goals, more challenging requirements are put on the corresponding antenna design.

According to technical specification 38.101 of the 3G Partner Program, FR1 is the 5G NR band operating below 6 GHz (or less), while FR2 is the 5G NR band operating in millimeter-wave [1]. The design of millimeter-wave antenna is mainly faced with the serious problem of spatial attenuation, which is not discussed here [2]. In bands below 6 GHz, 3G/4G mobile communication systems now use bands below 3 GHz, while bands between 5 and 6 GHz are now used in WLAN 5 GHz bands (5150-5825 MHz). For 5G networks, 5G NR bands for n77 (3300-4200 MHz), n78 (3300-3800 MHz) and n79 (4400-5000 MHz) are planned. At present, 5G antenna design in the band below 6 GHz faces the bottleneck of limited bandwidth and needs to be expanded. For mobile terminal applications, early antenna designs below 6 GHz were concentrated in 3.4-3.6 GHz or 3.3-3.8 GHz, with relatively limited bandwidth [3–7]. Dual-band antennas covering 3.3-3.8 GHz and other bands below 6 GHz are studied in [8–11]. Recently, [12–14] antennas have been proposed to fully cover 5G NR bands n77 (3300-4200 MHz), n78 (3300-3800 MHz), and n79 (4400-5000 MHz). Still, their bandwidth is expected to expand further.

A simple design scheme for 5G MIMO smartphone antennas is to place 4 or 8 antenna units in different areas of the smartphone [2–26]. Due to the limited space, the coupling effect between elements is usually the focus of attention, and it is difficult to achieve decoupling between them. In recent years, there has been much research on terminal antenna decoupling. For example, neutralization line [15] is a common decoupling technique, but it tends to work only in narrow bands. In [8], spatial orthogonal decoupling is achieved by placing units at four corners of the substrate. In addition, some other decoupling technologies, such as defective ground structure [16–17], decoupling unit [18] and self-isolation unit [19–22], lumped element loading [23], and differential feed [24], are also studied to further improve the

isolation performance. Although these various decoupling technologies improve the isolation performance of antenna elements, they also occupy a lot of space resources. Therefore, how to simplify the design of the decoupling structure so as to improve the isolation degree between units and reduce the occupation of space resources has become a topic worthy of study.

This paper proposes a decoupled dual antenna pair for sub-6G smartphone applications. According to the design requirements of the combination of modern smart phone antenna and metal frame, four antenna pairs are gathered on the mobile terminal to form a broadband eight-element MIMO antenna array. The prototype of MIMO antenna array is fabricated and tested. In addition to covering 5G NR n77/n78/n79 bands, the array can also work in the 5 GHz (5170-5835 MHz) band of WLAN. The isolation performance in the whole working band is better than 11 dB, which can well meet the requirements of 5G terminal antenna. The measured results agree well with the simulation results.

## II. ANTENNA DESIGN AND GEOMETRY

### A. Geometry of proposed antenna

Figure 1 is a schematic diagram of an eight-element MIMO mobile phone antenna proposed in this paper. All antenna elements are located on the two long frames of the mobile phone. The size of the main substrate of the system adopts the general specifications of mobile phones in the contemporary market, and the size is 150 mm x 75 mm. The size of the two small substrates is 150 mm x 7 mm, they are placed vertically on both sides of the main substrate, and four antenna units are placed

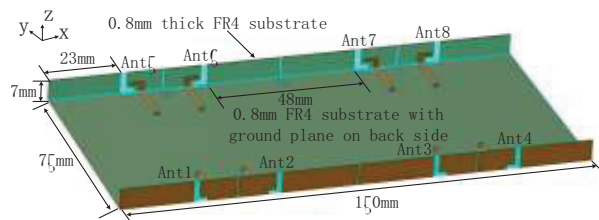


Fig. 1. Schematic diagram of eight-element MIMO mobile phone antenna.

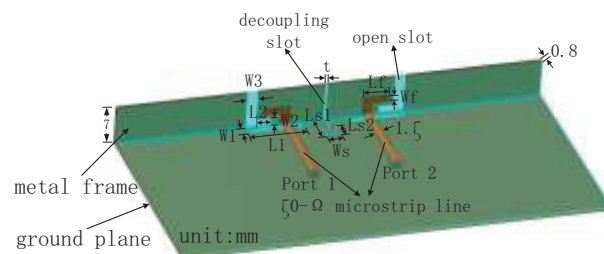


Fig. 2. Structure diagram of compact antenna pair.

on each small substrate. The material used for the main substrate and the small substrate are FR-4, the substrate thickness is 0.8 mm, the relative dielectric constant  $\epsilon_r$  is 4.3, and the loss angle tangent  $\tan \delta$  is 0.025. Figure 2 shows the structure diagram of the antenna pair in the mobile phone antenna. It can be seen from the figure that the antenna unit consists of an open slot in a small substrate and a slot in the floor. The antenna structure is fed by coupling L-shaped feeder branches on the substrate. The two antenna elements in the antenna pair are also arranged with respect to the decoupled structure. The decoupling between the compact antenna pairs is realized by a slotted structure designed with a zigzag shape. The values of each structural parameter in the antenna structure are given in Table 1. Each antenna is fed from the back of the substrate by an SMA connector through a hole connected to the microstrip line.

Table 1: Antenna element size / mm

W1	W2	W3	Ws	Wf	L1	L2
2	1.5	2	2.5	1	10	2.5
Ls1	Ls2	Lf	t			
5.5	3	4.5	0.5			

### B. Design process and analysis

The structural design comparison of MIMO mobile phone antenna designed in this paper is shown in Fig. 3. In order to clearly show the performance advantages brought by the antenna structure that we finally designed, Fig. 4 shows the comparison of S parameters under three different antenna design forms. Compared with the structure of antenna 1, the proposed antenna structure has one more rectangular slot on the side small substrate, and the antenna unit is an L-shaped slot when viewed from the side. Antenna 2 does not have a zigzag slot between two compact antenna pairs. As can be seen from the comparison of S parameters of the three antenna designs in Fig. 4, the  $-6$  dB impedance bandwidth of antenna 1 is relatively narrow, mainly reflected by the fact that the coverage range of the frequency band just covers the critical value of the low frequency band. Moreover, due to the existence of the decoupling structure in its design, the element isolation degree of antenna 1 is relatively ideal. The  $-6$  dB impedance bandwidth of antenna 2 is relatively wide, especially in the lower frequency band. However, due to the absence of a decoupling structure, the isolation degree between elements is relatively low, which is also a reason for its wide impedance bandwidth in the lower frequency band. It can be seen from the simulation results of S parameters that the  $-6$  dB impedance bandwidth of the proposed antenna is wider than that of antenna 1 without a rectangular slot on the small substrate. Compared with antenna 2 without the decoupling

structure, the isolation degree between elements of the proposed antenna is higher than 10 dB, which is about 5 dB higher.

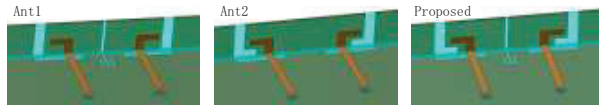


Fig. 3. Design evolution process of antenna structure.

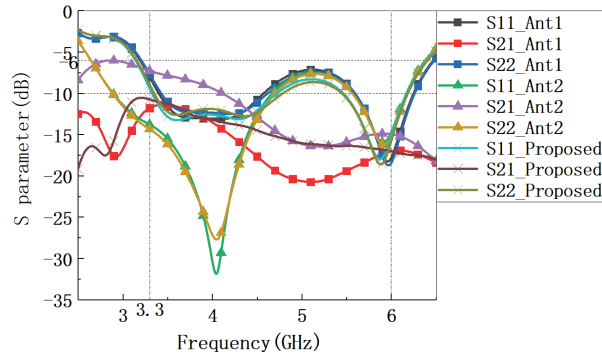


Fig. 4. Comparison of S parameters in structural design of antenna pairs.

### III. RESULTS AND DISCUSSION

#### A. Current distribution

In order to understand the decoupling principle of the proposed antenna more intuitively, Figs. 5 (a) and (b) show the electric field and current distribution of the open slot antenna at the resonant frequency 3.78 GHz and 5.85 GHz, respectively. It can be seen from Fig. 5 that there is a maximum electric field at the open end of the open slot antenna and a null electric field at the shorted end of the open slot antenna. It is obvious that a quarter-wavelength slot mode is excited within the open slot. At the two different resonant frequencies, the electric field direction in the open slot is opposite, and the current distribution is different. The current distribution at resonant frequency  $f_2=5.85$  GHz has a current null point, so different resonances are generated.

Figure 6 shows the comparison of surface current distribution between antenna pairs at 3.78 GHz with or without a decoupling structure. Similarly, the decoupling effect also exists in the whole operating frequency band of the antenna. As can be seen from Fig. 6, when there is no designed decoupling structure between compact antenna pairs, the current fed from one port will be coupled from antenna 1 to antenna 2, resulting in a large current flowing on antenna 2. However, when the designed decoupling structure exists, the coupling current basically flows through the designed decoupling structure

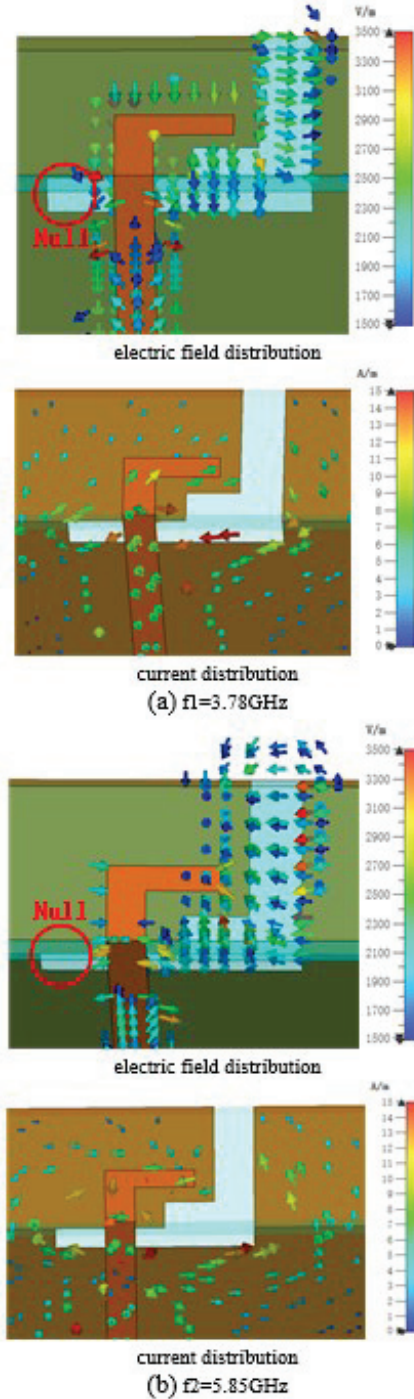


Fig. 5. Electric field distribution and current distribution of antenna element at (a)  $f_1=3.78$  GHz and (b)  $f_2=5.85$  GHz.

with a zigzag shape, making the coupling current on antenna 2 virtually absent, so as to achieve a better isolation effect between antenna pairs.

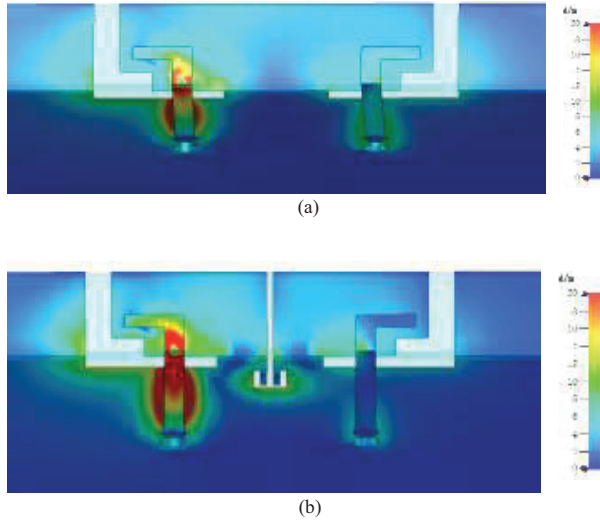


Fig. 6. Comparison of surface current distribution of antenna pairs at 3.78GHz. (a) There is no decoupling structure. (b) There are decoupling structures.

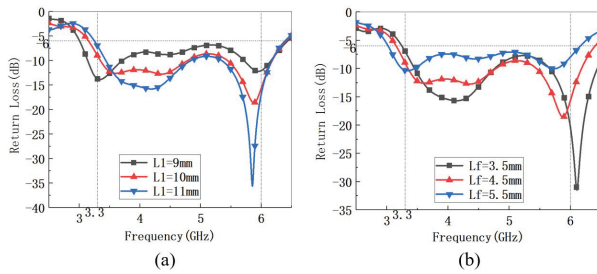


Fig. 7. The return loss of antenna unit varies with (a)  $L1$  and (b)  $Lf$ .

## B. Parameter analysis

In this section, the effects of some important parameters on the performance of the antenna are analyzed. The influence results of the length  $L1$  of antenna unit slot and L-type coupling feed branch length  $Lf$  on the return loss of the antenna unit are shown in Figs. 7 (a) and (b) respectively. As can be seen from the figure, with the increase of the length  $L1$  of the antenna unit slot, the corresponding lower resonant frequency point moves to the high frequency, and the  $-6$  dB impedance bandwidth is also reduced at this time. However, with the increase of L-type coupling feed branch length  $Lf$ , the overall resonant depth of the antenna decreases, that is, the Q value decreases, and the resonance point at the low frequency also moves to the lower frequency band. Therefore,  $L1=10$  mm and  $Lf=4.5$  mm are taken in combination with the effects of the two parameters on the overall performance of the antenna. Figures 8 (a) and (b) respectively show the influence of two key parameters  $Ls1$  and  $Ls2$  in the decoupling structure of

antenna pair on the return loss of antenna unit itself and the isolation degree between units. As can be seen from the figure, the impedance bandwidth of the corresponding low frequency band becomes wider with the increase of the length  $Ls1$  of the zigzag shape decoupling slot, but the isolation degree between the corresponding antenna pairs also decreases. Similarly, with the increase of the length  $Ls2$  of the zigzag shape decoupling slot, the impedance bandwidth of the corresponding low frequency band also becomes wider, while the isolation degree between the corresponding antenna pairs also decreases. Therefore,  $Ls1=5.5$  mm and  $Ls2=3$  mm in combination with the effects of the two parameters on the overall performance of the antenna.

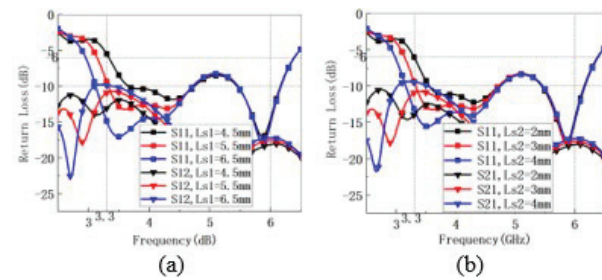


Fig. 8. The return loss of antenna unit varies with (a)  $Ls1$  and (b)  $Ls2$ .

## C. Test results

In order to better analyze the performance of the sub-6G MIMO mobile phone antenna proposed in this paper, according to the specific size of the antenna model given in Table 1, physical production and testing of the antenna model were carried out. Figure 9 is a physical picture of the antenna. The test results were compared with the simulation results, the comparison of simulation and test results of reflection coefficient  $S11$  and transmission coefficient  $S21$  of this eight-element MIMO antenna is shown in Figs. 10 and 11 respectively. Due to the symmetry of the antenna structure, only necessary results are given in the figure. As can be seen from Fig. 10, the antenna system can well cover the sub-6G (3.3-6 GHz) full frequency band, and the simulation results are in good agreement with the measured results. As can be seen from Fig. 11, the isolation degree between the eight antennas is all better than 10 dB, which basically meets the requirements of the antenna unit isolation degree of MIMO mobile phone antennas. The isolation degree of antenna units mainly depends on the isolation degree between antenna pairs and antenna pairs on the same frame small substrate and the isolation degree between antenna pairs.

Figure 12 shows the simulation and measured comparison results of the total efficiency of MIMO mobile

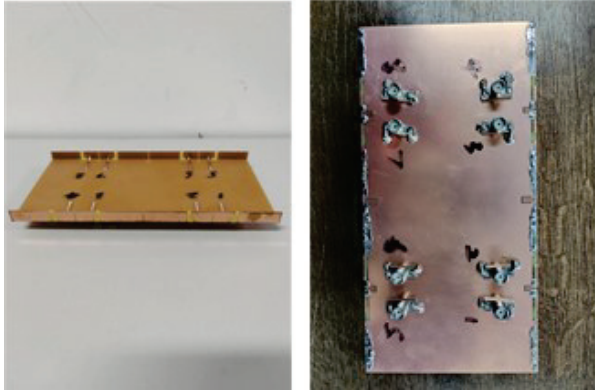


Fig. 9. Photograph of the fabricated prototype.

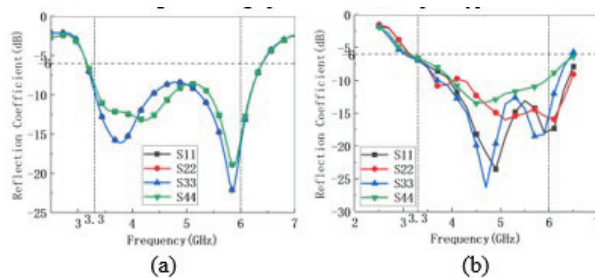


Fig. 10. Reflection coefficients of Ants1-4. (a) Simulated. (b) Measured.

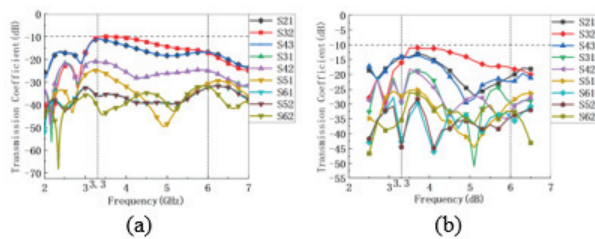


Fig. 11. Isolation levels between two antenna units. (a) Simulated. (b) Measured.

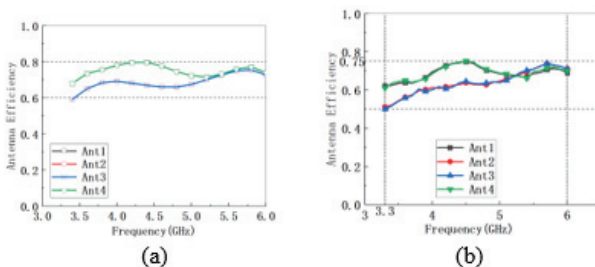


Fig. 12. Total antenna efficiencies of Ants1-4. (a) Simulated. (b) Measured.

phone antenna. The simulation results show that the total efficiency of the antenna is more than 60% in 3.3-6GHz

band, and the maximum efficiency reaches 80%. The measured results show that the total efficiency of the antenna is more than 50% in 3.3-6GHz band, and the maximum efficiency is 75%. Figures 13 and 14 show the 2D pattern of antenna 1 and antenna 2 at three different frequency points in xoy plane respectively. The results are obtained by CST simulation. It can be seen from the figure that the antenna unit has a certain directivity according to the position of distribution, and the results of simulation and measurement also have good consistency. The result of comprehensive testing shows that the eight-element antenna system has good radiation receiving performance.

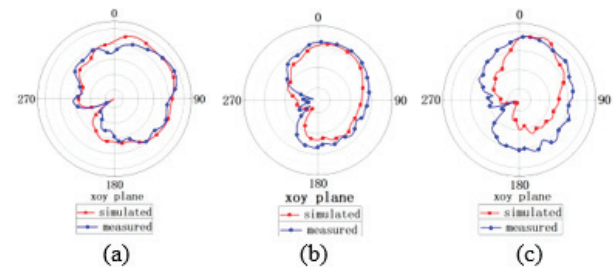


Fig. 13. Simulated and measured radiation patterns across the  $xy$  plane for Ant1. (a) at 3.6 GHz, (b) at 4.8 GHz, (c) at 5.6 GHz.

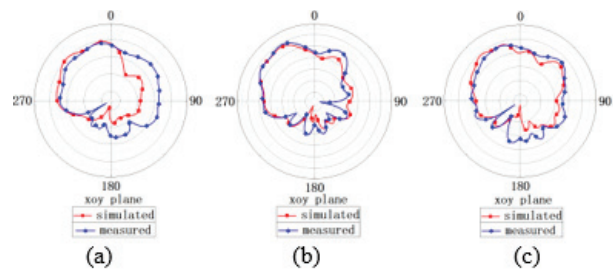


Fig. 14. Simulated and measured radiation patterns across the  $xy$  plane for Ant2. (a) at 3.6 GHz, (b) at 4.8 GHz, (c) at 5.6 GHz.

Figure 15 shows the Envelope Correlation Coefficient (ECC) simulation results of the antenna system [25–26]. Note that only necessary results are given in the figure. As can be seen from the figure, the ECC of the antenna system is all less than 0.08, indicating that each antenna unit of the antenna system has good channel independence. Table 2 compares the proposed eight-element MIMO array with some recently reported antenna designs. As can be seen, most designs cover only one or two narrow bands, and many broadband antennas are inefficient. In the antenna design proposed by us, on the premise that the isolation degree basically meets the requirements, not only the broadband design of the

antenna is realized, but also the overall efficiency and ECC of the antenna are ideal.

In order to realize the design of eight-element MIMO terminal antenna, reasonable spatial layout of the designed antenna pair is carried out, as shown in Fig. 16 (a). Since the two elements in the antenna pair are affected differently by the ground, the size of each element is fine-tuned to optimize the antenna pair. In addition, in order to reduce the coupling between antenna pairs on the same side, a zigzag-shaped decoupling gap is also designed between them. The size of the decoupling gap is given in Fig. 16 (a). Figure 16 (b) shows the comparison results of S32 antenna with or without the decoupling structure. As can be seen from the figure, after

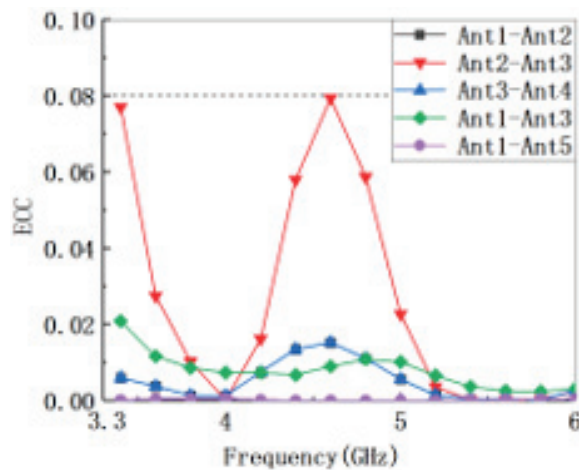


Fig. 15. The envelope correlation coefficient (ECC) of MIMO antenna.

Table 2: Performance comparison of the 5G MIMO terminal antennas

Design	AP	WB (GHz)	Isolation (dB)	Eff (%)	ECC
[5]	Y	3.4-3.6	>17	22-50	<0.1
[24]	Y	3.33-3.6	>14	52-65	<0.1
[9]	N	3.3-4.2 4.8-5	>12.5	LB 53-76 HB 62-79	<0.1
[10]	Y	3.3-3.6 4.8-5	>17.5	LB 49-68 HB 49-70	<0.1
[12]	Y	3.3-5	>12	31-88	<0.1
[21]	Y	3.3-7.5	>10	15-70	<0.0
Proposed	Y	3.3-6	>11	50-75	<0.8

Abbreviations: AP=Antenna Pair, WB=Working Band, Eff=Efficiency, LB=Low Band, HB=High Band.

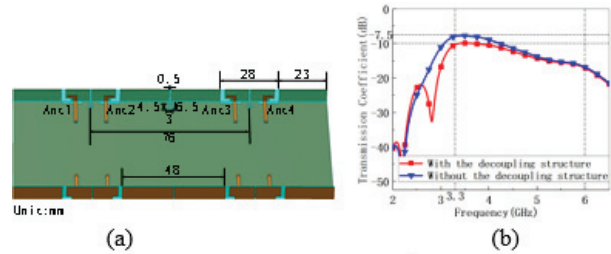


Fig. 16. Overall optimization design of antenna. (a) Spatial layout dimensions of antenna pairs. (b) Influence of decoupling structure on S32.

the decoupling structure is added, the isolation degree between antenna 2 and antenna 3 is improved to more than 10 dB.

#### IV. CONCLUSION

This paper presents an eight-element MIMO array for 5G terminals. The working bandwidth of the antenna ranges from 3.3 to 5.95 GHz (57.3%), fully covering n77/n78/n79 and WLAN 5 GHz band. According to the real antenna made and tested, the measured results are in good agreement with the simulation results. The isolation performance of the system is better than 11 dB, the total efficiency is higher than 50%, and the ECC is lower than 0.08. It has good MIMO performance and meets the performance requirements of modern mobile terminal antennas. It is a good MIMO antenna solution for 5G mobile terminals.

#### REFERENCES

- [1] 3GPP specification series: 38series, 3GPP TS 38.101-1 v15.0.0, 2017. Available online at: <http://www.3gpp.org/DynaReport/38-series.htm>
- [2] M. Ikram, N. Nguyen-Trong, and A. Abbosh, "Hybrid antenna using open-ended slot for integrated 4G/5G mobile application," *IEEE Antennas and Wireless Propagation Letters*, vol. 19, no. 4, pp. 710-714, Apr. 2020.
- [3] L. Sun, H. Feng, Y. Li, and Z. Zhang, "Compact 5G MIMO mobile phone antennas with tightly arranged orthogonal-mode pairs," *IEEE Trans. Antennas Propag.*, vol. 66, no. 11, pp. 6364-6369, Nov. 2018.
- [4] Y. Li, C. Sim, Y. Luo, and G. Yang, "High-isolation 3.5 GHz eight-antenna MIMO array using balanced open-slot antenna element for 5G smartphones," *IEEE Trans. Antennas Propag.*, vol. 67, no. 6, pp. 3820-3830, Jun. 2019.
- [5] Z. Ren, A. Zhao, and S. Wu, "MIMO antenna with compact decoupled antenna pairs for 5G mobile terminals," *IEEE Antennas and Wireless Propagation Letters*, vol. 18, no. 7, pp. 1367-1371, Jul. 2019.

- [6] H. Piao, Y. Jin, and L. Qu, "A compact and straight-forward self-decoupled MIMO antenna system for 5G applications," *IEEE Access*, vol. 8, pp. 129236-129245, Jul. 2020.
- [7] A. Ren, Y. Liu, H. Yu, Y. Jia, C. Sim, and Y. Xu, "A high-isolation building block using stable current nulls for 5G smartphone applications," *IEEE Access*, vol. 7, pp. 170419-170429, Nov. 2019.
- [8] D. Serghiou, M. Khalily, V. Singh, A. Araghi, and R. Tafazolli, "Sub-6 GHz dual-band  $8 \times 8$  MIMO antenna for 5G smartphones," *IEEE Antennas Wireless Propag. Lett.*, vol. 19, no. 9, pp. 1546-1550, Sep. 2020.
- [9] L. Cui, J. Guo, Y. Liu, and C. Sim, "An 8-element dual-band MIMO antenna with decoupling stub for 5G smartphone applications," *IEEE Antennas Wireless Propag. Lett.*, vol. 18, no. 10, pp. 2095-2099, Aug. 2019.
- [10] Z. Ren and A. Zhao, "Dual-band MIMO antenna with compact selfdecoupled antenna pairs for 5G mobile applications," *IEEE Access*, vol. 7, no. 10, pp. 82288-82296, Oct. 2019.
- [11] W. Hu, L. Qian, S. Gao, L.-H. Wen, Q. Luo, H. Xu, X. Liu, Y. Liu, and W. Wang, "Dual-band eight-element MIMO array using multi-slot decoupling technique for 5G terminals," *IEEE Access*, vol. 7, pp. 153910-153920, Oct. 2019.
- [12] L. Sun, Y. Li, Z. Zhang, and Z. Feng, "Wideband 5G MIMO antenna with integrated orthogonal-mode dual-antenna pairs for metal-rimmed smartphones," *IEEE Trans. Antennas Propag.*, vol. 68, no. 4, pp. 2494-2503, Apr. 2020.
- [13] C. Sim, H. Liu, and C. Huang, "Wideband MIMO antenna array design for future mobile devices operating in the 5G NR frequency bands n77/n78/n79 and LTE band 46," *IEEE Antennas Wireless Propag. Lett.*, vol. 19, no. 1, pp. 74-78, Jan. 2020.
- [14] L. Sun, Y. Li, and Z. Zhang, "Wideband decoupling of integrated slot antenna pairs for 5G smartphones," *IEEE Trans. Antennas Propag.*, vol. 69 no. 4, pp. 2386-2391, Apr. 2021.
- [15] J. Guo, L. Cui, C. Li, and B. Sun, "Side-edge frame printed eight-port dual-band antenna array for 5G smartphone applications," *IEEE Trans. Antennas Propag.*, vol. 66, no. 12, pp. 7412-7417, Dec. 2018.
- [16] W. Jiang, B. Liu, Y. Cui, and W. Hu, "High-isolation eight-element MIMO array for 5G smartphone applications," *IEEE Access*, vol. 7, pp. 34104-34112, Mar. 2019.
- [17] H. Chen, Y. Tsai, C. Sim, and C. Kuo, "Broadband eight-antenna array design for sub-6 GHz 5G NR bands metal-frame smartphone applications," *IEEE Antennas and Wireless Propagation Letters*, vol. 19, no. 7, pp. 1078-1082, Jul. 2020.
- [18] H. Xu, H. Zhou, S. Gao, H. Wang, and Y. Cheng, "Multimode decoupling technique with independent tuning characteristic for mobile terminals," *IEEE Trans. Antennas Propag.*, vol. 65, no. 12, pp. 6739-6751, Dec. 2017.
- [19] A. Zhao and Z. Ren, "Multiple-input and multiple-output antenna system with self-isolated antenna element for fifth-generation mobile terminals," *Microw. Opt. Technol. Lett.*, vol. 61, no. 1, pp. 20-27, Jan. 2019.
- [20] A. Zhao and Z. Ren, "Size reduction of self-isolated antenna MIMO antenna system for 5G mobile phone applications," *IEEE Antennas Wireless Propag. Lett.*, vol. 18, no. 1, pp. 152-156, Jan. 2019.
- [21] X.-T. Yuan, Z. Chen, T. Gu, and T. Yuan, "A wideband PIFA-pair-based MIMO antenna for 5G smartphones," *IEEE Antennas and Wireless Propagation Letters*, vol. 20, no. 3, pp. 371-375, Mar. 2021.
- [22] L. Chang, Y. Yu, K. Wei, and H. Wang, "Orthogonally polarized dual antenna pair with high isolation and balanced high performance for 5G MIMO smartphone," *IEEE Transactions on Antennas and Propagation*, vol. 68, no. 5, pp. 3487-3495, May 2020.
- [23] C. Deng, D. Liu, and X. Lv, "Tightly arranged four-element MIMO antennas for 5G mobile terminals," *IEEE Trans. Antennas Propag.*, vol. 67, no. 10, pp. 6353-6361, Oct. 2019.
- [24] Z. Xu and C. Deng, "High-isolated MIMO antenna design based on pattern diversity for 5G mobile terminals," *IEEE Antennas Wireless Propag. Lett.*, vol. 19, no. 3, pp. 467-471, Mar. 2020.
- [25] Y. Q. Hei, J. G. He, and W. T. Li, "Wideband decoupled 8-element MIMO antenna for 5G mobile terminal applications," *IEEE Antennas and Wireless Propagation Letters*, vol. 20, no. 8, pp. 1448-1452, Aug. 2021.
- [26] X.-T. Yuan, W. He, K.-D. Hong, C.-Z. Han, Z. Chen, and T. Yuan, "Ultra-wideband MIMO antenna system with high element-isolation for 5G smartphone application," *IEEE Access*, vol. 8, pp. 56281-56289, Mar. 2020.
- [27] M. O. Khalifa, A. M. Yacoub, and D. N. Aloï, "Compact 2x2 and 4x4 MIMO antenna systems for 5G automotive applications," *Applied Computational Electromagnetics Society (ACES) Journal*, vol. 36, no. 6, pp. 1943-5711, Nov. 2021.
- [28] J. Su, Z. Dai, and J. Du, "A compact dual-band MIMO antenna for 5G mobile communications,"

*Applied Computational Electromagnetics Society (ACES) Journal*, vol. 34, no. 11, pp. 1943-5711, Nov. 2019.



**Jiagang He** was born in Xiangtan, Hunan province, China, in 1997. He received his Bachelor's degree from the College of Electronic Science and Technology, Hunan University of Technology, Zhuzhou, China, in 2019. He is now studying for a post-graduate degree at the College of Electronic Science and Technology, Hunan University. His research interests are terminal antenna and EMC.



**Shichao Zhu** received his Bachelor's degree from the School of Electrical and Automation Engineering, East China Jiaotong University, Nanchang, China, in 2020. He is currently pursuing a Master's degree at the College of Electrical and Information Engineering, Hunan University, Changsha, China, under the supervision of Prof. G. S. Li. His research interests include reconfigurable antennas, electromagnetic metamaterials and their antenna applications.



**Jie Yu** was born in Xinyang, Henan province, China, in 1998. He received his Bachelor's degree in Optoelectronic Information Science and Engineering from Changsha University of Science and Technology, Changsha, China, in 2019. He is currently working as a post-graduate at Hunan University. His research interest is liquid antennas.



**Hao Li** is an associate professor at the College of Electrical and Information Engineering, Hunan University, Changsha, China. His research interests include microwave dielectric materials and devices for microwave communication.



**Gaosheng Li** (M'08, SM'19) received his B.S. degree in Electromagnetic Fields and Microwaves in 2002 from the National University of Defense Technology (NUDT), Changsha, China. His M.S. and Ph. D. degrees were in Electronic Science and Technology from the same university, in 2004 and 2013, respectively.

He was with NUDT as a Teaching Assistant from 2004 to 2006, as a Lecturer from 2006 to 2011, and then as an Associate Professor from 2011 to 2017. He joined Hunan University as a Professor in 2018. From 2014 to 2016, he was with Nanjing University of Aeronautics and Astronautics (NUAA) and Wuxi Huace Electronic Systems Co., Ltd., China as a postdoctoral Research Fellow. From 2016 to 2017, he was a Visiting Scholar at the University of Liverpool (UoL), United Kingdom, sponsored by the China Scholarship Council (CSC). He is a Senior Member of the IEEE. His research interests include antennas and propagation (AP), electromagnetic compatibility (EMC), and wireless propagation and microwave systems.

# A Simple Single-fed Left/Right-Hand Circular Polarization Antenna for GPS Applications

Lulu Meng<sup>1</sup>, Yingsong Li<sup>1,2</sup>, and Zhixiang Huang<sup>1,2</sup>

<sup>1</sup>School of Electronic and Information Engineering  
Anhui University, Hefei, 230601, China

<sup>2</sup>Key Laboratory of Intelligent Computing and Signal Processing  
Ministry of Education, Anhui University, Hefei, 230601, China  
liyingsong@ieee.org

**Abstract** – A simple single-feeding circular polarization (CP) antenna with controlled left/right-hand characteristics is proposed and investigated for GPS L2 band applications. To achieve the CP characteristics, four arc-shaped cutting corners with different sizes are removed from a circular patch to give 90° phase difference to implement CP. By adjusting the radius of the four arc-shaped cutting corners, the antenna can be controlled to get left/right-hand circular polarization (L/RHCP). The proposed CP antenna is modeled, simulated, fabricated and measured, and the results demonstrate that the antenna provides an axial ratio beamwidth over 180 MHz, and impedance bandwidth of 20 MHz for L/RHCP. Additionally, the devised CP antennas have good directional radiating patterns, making them suitable for GPS L2 band applications.

**Index Terms** – arc-shaped slots, GPS, left/right-hand circular polarization antenna, L2 band.

## I. INTRODUCTION

Circularly polarized (CP) antennas have been widely used in recent years due to their stable signal transmission and reception characteristics in bad weather, polarization rotation and flexible directionality between transmitter and receiver [1–19]. For satellite and global positioning system (GPS) applications, to improve the accuracy and flexibility of GPS systems, there is a high demand to get thin, lightweight and high gain CP antennas [5, 20, 21]. In the past few decades, a lot of research on various CP antennas including microstrip antennas, horn antennas and spiral antennas has been done [22, 23]. Microstrip antennas have been widely used in military and civil fields due to their advantages of small size, low cost, easy manufacturing and easy expansion into arrays [24, 25]. For developing patch antennas, a simple way to achieve CP operation is to feed

the patch in two orthogonal directions to excite two resonant modes [26]. The dual feed mechanism increases the antenna size, the geometric complexity of the antenna, and leads to additional losses that reduce the gain [27]. In order to overcome the complexity of double feed, the patch antenna with single feed is studied [28]. Single-fed microstrip antenna is the simplest structure to realize CP radiation. With the development of microstrip antennas, various single-fed CP microstrip antennas have been reported by adjusting the physical size of the patch or etching the slot [29, 30].

In [31], an antenna is fed by two L-shaped probes in the feed network with a 90° broadband balun. By inserting a small metal sheet between two probes, the current distribution on the patch is changed, and axial ratio (AR) can be adjusted flexibly and the bandwidth could be broadened. A single-fed high-gain CP antenna with loading of shorting pins is proposed in [32]. Two sets of pins are first symmetrically introduced and moved outward along the diagonals of a square patch. After that, two degenerate modes are properly split to produce CP radiation by means of perturbing the position of one pair of the pins.

The characteristics of broadband CP are studied by using the topological structure of antenna in [33]. Impedance and AR bandwidth are achieved by using a new vertically coupled resonator structure and inherent 90° phase difference between the two coupling paths. The neutralization line is then used to improve the isolation between the two polarities. The antenna can achieve CP characteristics due to the U-shaped slots etched on metal patches [34–36].

A microstrip CP antenna loaded with arc-shaped cutting corners is proposed with single feed, which uses four unequal arc-shaped cutting corners in its diagonal. The CP antenna can be used as left/right-hand circular polarization (L/RHCP) antenna by controlling the size of each of the arc-like cutting corners. The proposed

antenna is modeled, created, simulated and analyzed, and the results show that the modeled antenna has good CP characteristics, directional radiation patterns, which is suitable for GPS L2 band.

## II. ANTENNA GEOMETRY AND DESIGN

### A. Geometries of the proposed microstrip antenna

The geometry of the proposed CP microstrip antenna is drawn in Fig. 1, where the designed CP antenna resonates at the center frequency of 1.228 GHz. The circular patch is printed on RO5880 substrate with a dielectric constant of 2.2, height of 1.575 mm, and loss tangent of 0.0009. In addition, the circular patch is fed by a coaxial probe, which has the distance of  $x_0$  away from the center of the patch. Four arc-like cutting corners are loaded around the radiating patch, and their radius are  $r_1$ ,  $r_2$ ,  $r_3$  and  $r_4$  respectively. By slightly changing the radius of the four arc-like cutting corners, the proposed antenna can not only generate CP radiation, but also realize polarization for L/RHCP. The antenna has a radius of 67.5 mm, and the other parameters are listed in Table 1.

Table 1: Dimensions of the antenna (UNIT: mm)

Parameter	Polarization	
	LHCP	RHCP
$r_1$	13.4	9.7
$r_2$	9.7	13.4
$r_3$	8.45	13.55
$r_4$	13.55	8.45

### B. Operating principle of CP radiation

In order to understand the principle of CP antenna design, Fig. 2 shows the surface current on the radiating patch at 1.228 GHz. Before the arc-shaped corners are etched, there is only current vector in the horizontal direction. When the arc-shaped cutting corners are etched, the new current vector is observed in the vertical direction, as shown in Figs. 2 (a) and 2 (d). This clearly shows that due to the asymmetric arc-shaped corner structures, a second resonant mode is generated, which helps to achieve the CP design. In addition, the surface current vector rotates clockwise, which means that the proposed microstrip antenna is LHCP. By changing the radius of the arc-shaped corners, the CP of the antenna can be converted from LHCP to RHCP, as shown in Fig. 3.

For left-handed circular polarization, we have:

$$r_4 > r_1 > r_2 > r_3. \quad (1)$$

For right-handed circular polarization, we use:

$$r_3 > r_2 > r_1 > r_4. \quad (2)$$

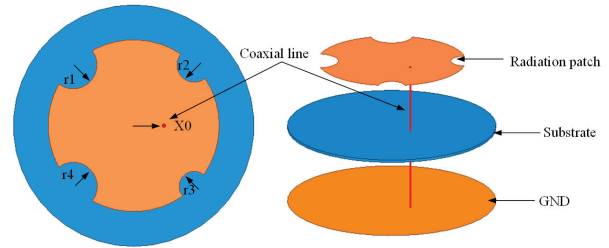


Fig. 1. Model of the CP antenna. (a) Top view. (b) 3-D view.

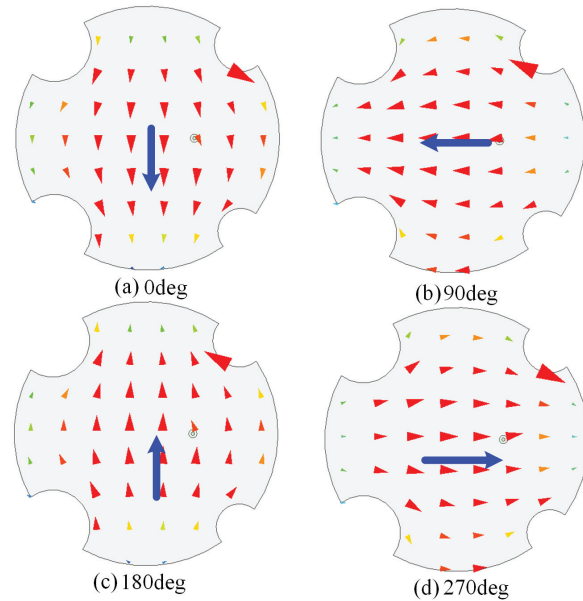


Fig. 2. Surface current distribution for the LHCP antenna at 1.228 GHz.

In the design, degeneracy mode can be eliminated by introducing appropriate asymmetry into antenna structure, where a mode increases with frequency and an orthogonal mode decreases by the same amount. Because the frequencies of the two modes are slightly different, with proper design, the field of one mode can produce a  $90^\circ$  phase difference required for circular polarization (CP). Herein, the asymmetric arc-shaped cutting corner helps to generate a second resonant mode, which has a slightly different frequency from the original resonant mode, with a phase difference of  $90^\circ$ . Therefore, CP radiation of the antenna is realized.

### C. 3-dB AR beamwidth

The 3 dB AR beamwidth of the two main planes (XOZ and YOZ planes) of the antenna at 1.228 GHz are plotted in Fig. 4, where the AR beamwidth is more than  $180^\circ$ . Therefore, the proposed antenna can cover the whole upper hemisphere and has a good application prospect.

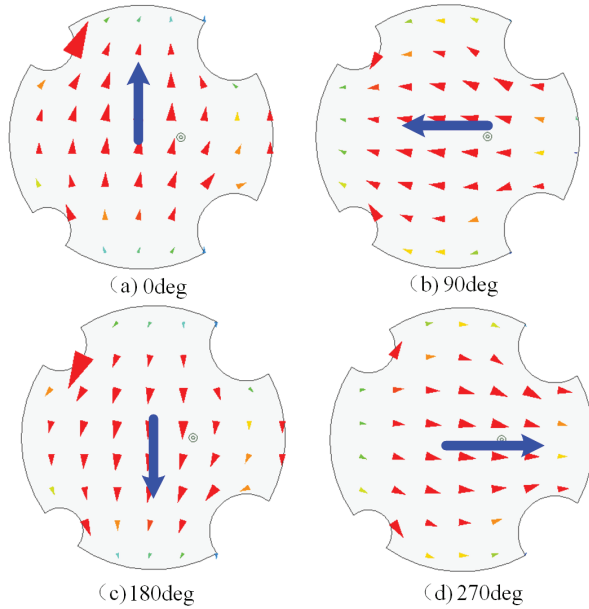


Fig. 3. Surface current distribution for the RHCP antenna at 1.228 GHz.

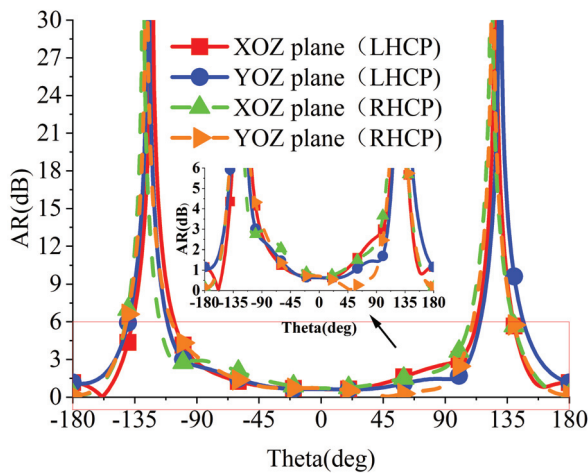


Fig. 4. AR beam-width for the L/RHCP antenna at XOZ and YOZ planes.

### III. ANTENNA PARAMETRIC ANALYSIS

In order to better explain how to realize CP operation of the antenna, the dimensions of arc-like cutting corners are studied. Only one parameter is changed each time, and the other parameters remain unchanged.

#### A. Different $r_1$

Figure 5 shows the S11 and AR of the designed CP antenna with different  $r_1$ , where the CP antenna is realized by the arc-like corners to get two resonant modes. As  $r_1$  increases, the working bandwidth becomes nar-

rower. By optimizing the radius, the two orthogonal resonant modes achieve the same amplitude and  $90^\circ$  phase difference to implement CP radiation of antenna. When the radius  $r_1$  is 13.4 mm, the antenna has the best CP performance.

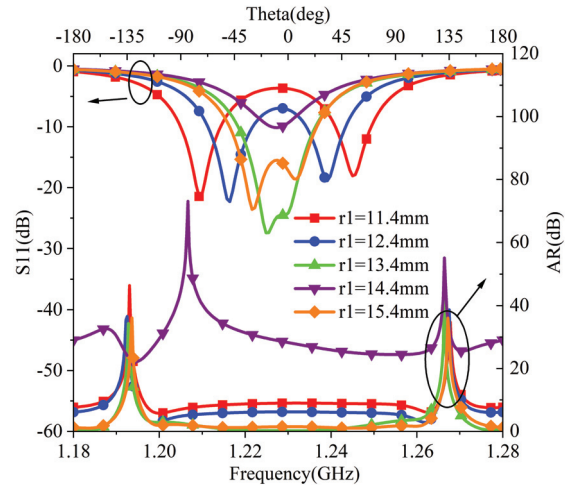


Fig. 5. S11 and AR with variation of  $r_1$ .

#### B. Different $r_2$

S11 and AR of the CP antenna is presented in Fig. 6 with different  $r_2$ . When  $r_2$  varies from 7.35 mm to 11.35 mm, the bandwidth gradually decreases. When  $r_2 = 10.35$  mm, the antenna achieves the widest working bandwidth, but the AR bandwidth does not meet the requirements. For good balance,  $r_2 = 9.7$  mm was selected. This time, the impedance bandwidth of the antenna is 20 MHz, and the 3 dB beam-width is about  $180^\circ$ .

#### C. Different $r_3$

The effects on S11 and AR with varying  $r_3$  are studied, and the results are presented in Fig. 7 for  $r_1 = 11.5$  mm,  $r_2 = 9.35$  mm, and  $r_4 = 13.55$  mm. From Fig. 7, it can be seen that once  $r_3$  increases, the antenna bandwidth gradually decreases. When  $r_3 = 8$  mm and 9 mm, the impedance bandwidth and AR meet the requirements. However, when  $r_3 = 8.45$  mm, the antenna has better resonance and axial ratio performance.

#### D. Different $r_4$

$r_4$  changes from 11.55 mm to 15.55 mm to optimize the antenna bandwidth, and the result is presented in Fig. 8. With the increase of  $r_4$ , the bandwidth gradually increases. For  $r_4 = 13.55$  mm, the antenna has the widest operating bandwidth and is able to generate two orthogonal modes for providing CP radiation.

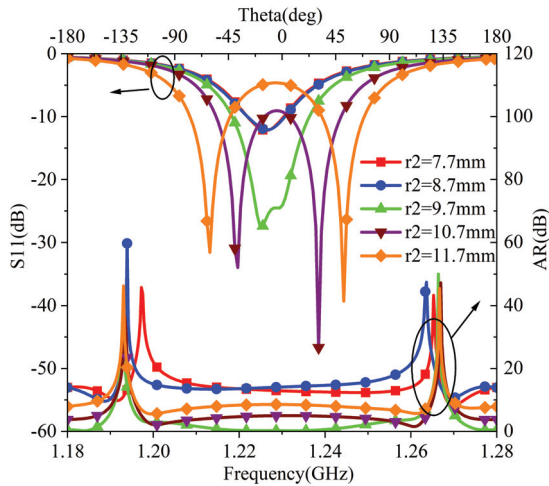
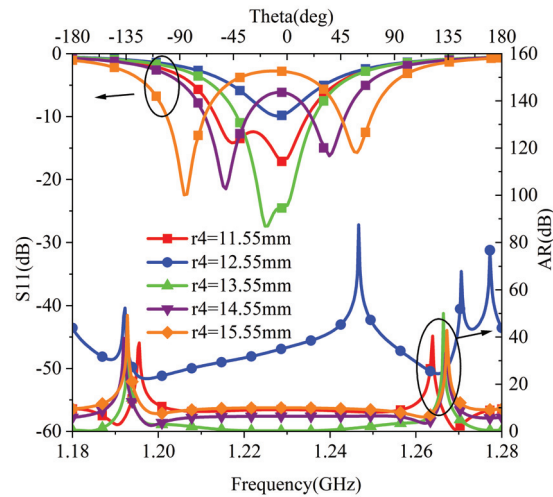
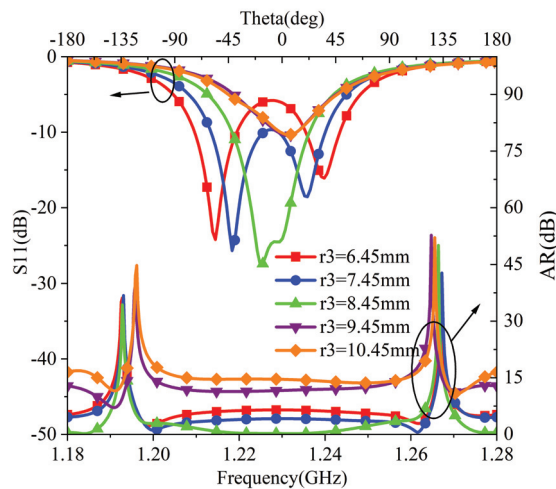
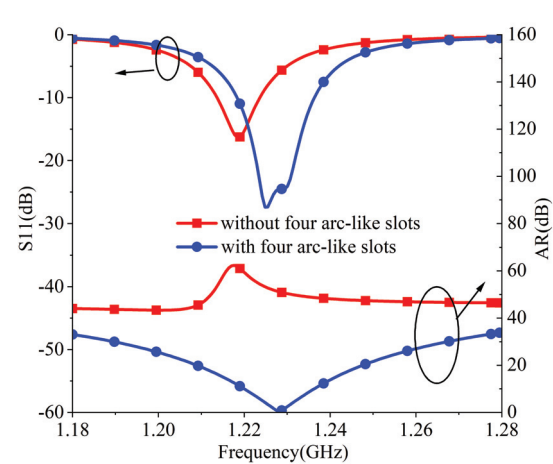
Fig. 6. S11 and AR with variation of  $r_2$ .Fig. 8. S11 and AR with variation of  $r_4$ .Fig. 7. S11 and AR with variation of  $r_3$ .

Fig. 9. The antenna S11 with and without the arc-like slots.

## IV. SIMULATION AND MEASUREMENT RESULTS

### A. Simulation comparisons with and without arc-like corners

S11 and AR of the antennas with and without arc-like corners are plotted in Fig. 9 for comparison. Before the addition of the arc-like slots, the bandwidth of the linearly polarized (LP) antenna is 10 MHz, and the AR is much larger than 3 dB. The antenna polarization changes from LP to CP and the AR is 0.18 dB at 1.228 GHz after the arc-like slots are added. In addition, the bandwidth of CP antennas extends to 20 MHz, which is wider than that of the LP antennas without arc-like slots. This shows that the added arc-like corners can effectively introduce

the second resonance to form CP radiation and expand the antenna bandwidth.

### B. Simulation and measurement comparisons

The prototypes of the devised CP antennas and the measurement setup are shown in Fig. 10. Figure 11 shows the simulated and measured S11 of the designed L/RHCP antenna, and the measured results are in good agreement with the simulation results. Simulation and measurement results show that the bandwidth of the designed antenna is 20 MHz, and mechanical errors in manufacture may lead to slight differences between the measurement and simulation results.

The proposed L/RHCP antenna has a peak gain of about 7.3 dBi and a 3-dB beam width of about  $180^\circ$ . The

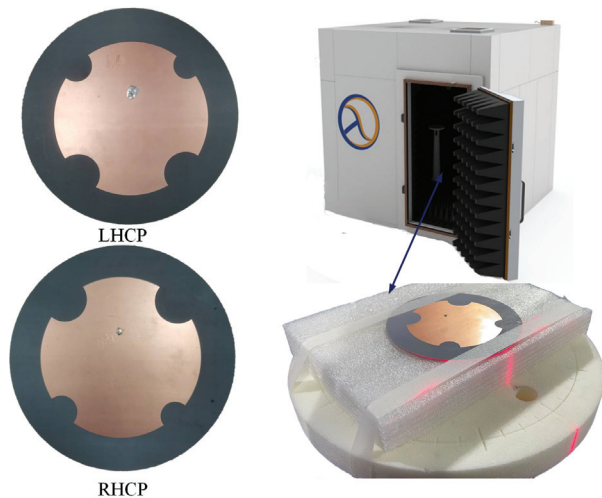


Fig. 10. Photographs of fabricated antennas.

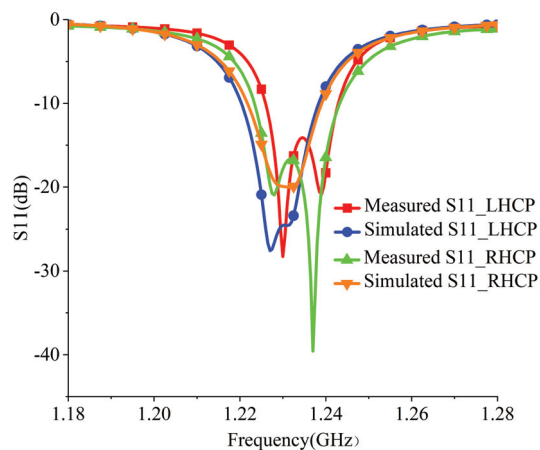


Fig. 11. The simulated and measured S11 of the L/RHCP microstrip antenna.

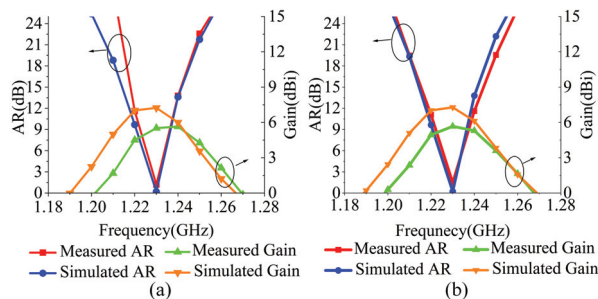


Fig. 12. The simulated and measured AR and gain of the antenna. (a) LHCP antenna. (b) RHCP antenna.

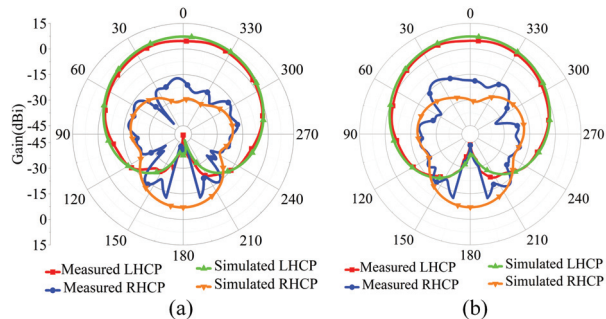


Fig. 13. Measured and simulated radiation patterns of LHCP antenna at the (a)  $\phi=0^\circ$ , and (b)  $\phi=90^\circ$  planes.

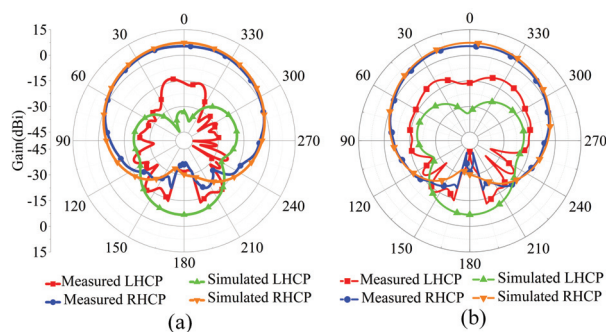


Fig. 14. Measured and simulated radiation patterns of RHCP antenna at the (a)  $\phi=0^\circ$ , and (b)  $\phi=90^\circ$  planes.

simulated and measured ARs and CP gains of L/RHCP antenna in relation to frequency are given in Fig. 12. The AR are in good agreement with the measurement results, while the measured gain is about 2 dB less than the simulated gain due to the feedline effects.

The proposed L/RHCP antenna is simulated and measured in XOZ and YOZ planes as placed in Figs. 13 and 14. The results show that the simulated radiation pattern is in good agreement with the measured radiation patterns. It is also clear that the antenna presents a good transverse radiation pattern. In the future, the proposed antenna can be used for MIMO system developments. Also, the size of the proposed antenna can be reduced using high dielectric constant substrate, and the antenna can be modeled to construct antenna array or MIMO antennas [37–44].

### V. CONCLUSION

Four arc-like corners are used to develop a circular polarized antenna using single feed. The antenna is modeled, simulated, and briefly discussed for GPS L2 band application. The antenna can be used as LHCP and RHCP applications by controlling the dimensions of the

four arc-like corners. The results show that the antenna has a good AR and, directional radiating, which is considered a good candidate for GPS applications.

### ACKNOWLEDGMENT

This work is also supported by the Joint Funds of the National Natural Science Foundation of China (U20A20164) and National Natural Science Foundation of China (61971001), and University Synergy Innovation Program of Anhui Province (GXXT-2020-050, GXXT-2020-051, GXXT-2021-027, GXXT-2021-037).

### REFERENCES

- [1] B. P. Kumar, D. Guha, and C. Kumar, "Reduction of beam squinting and cross-polarized fields in a wideband CP element," *IEEE Antennas and Wireless Propagation Letters*, vol. 19, no. 3, pp. 418-422, Mar. 2020.
- [2] Y. Shi and J. Liu, "A circularly polarized octagon-star-shaped microstrip patch antenna with conical radiation pattern," *IEEE Transactions on Antennas and Propagation*, vol. 66, no. 4, pp. 2073-2078, Apr. 2018.
- [3] Z. Wang, Y. Dong, and T. Itoh, "Miniaturized wideband CP antenna based on metaresonator and CRLH-TLs for 5G new radio applications," *IEEE Transactions on Antennas and Propagation*, vol. 69, no. 1, pp. 74-83, Jan. 2021.
- [4] Z. L. Zhang, K. Wei, J. Xie, J. Y. Li, and L. Wang, "The new c-shaped parasitic strip for the single-feed CP microstrip antenna design," *International Journal of Antennas and Propagation*, vol. 2019, pp. 1-9, Nov. 2019.
- [5] H. Yang, Y. Fan, and X. Liu, "A compact dual-band stacked patch antenna with dual CP for bei dou navigation satellite systems," *IEEE Antennas and Wireless Propagation Letters*, vol. 18, no. 7, pp. 1472-1476, Jul. 2019.
- [6] B. Liu, X. Chen, J. Tang, A. Zhang, and A. Kishk, "Co- and cross-polarization decoupling structure with polarization rotation property between linearly polarized dipole antennas with application to decoupling of circularly polarized antennas," *IEEE Transactions on Antennas and Propagation*, vol. 70, no. 1, pp. 702-707, Jan. 2022.
- [7] X. Yan, K. L. Chung, Y. Li, and Y. Li, "A Jia-shaped artistic patch antenna for dual-band circular polarization," *AEU - International Journal of Electronics and Communications*, vol. 120, ID:153207, Jun. 2020.
- [8] J. Li, J. Shi, L. Li, T. A. Khan, J. Chen, Y. Li, and A. Zhang, "Dual-band annular slot antenna loaded by reactive components for dual-sense circular polarization with flexible frequency ratio," *IEEE Access*, vol. 6, no. 1, pp. 64063-64070, Oct. 2018.
- [9] L. Meng, Z. Huang, and Y. Li, "A Da-shaped slotted circularly-polarization antenna for 5G applications," *International Applied Computational Electromagnetics Society (ACES-China) Symposium*, Xuzhou, 28-31 Jul. China, 2022.
- [10] W. Zhou, Y. Li, and Y. Xia, "A 5G hybrid circular polarization MIMO antenna," *IEEE 4th International Conference on Electronic Information and Communication Technology (ICEICT)*, 18-20, Aug. Xian, China, 2021.
- [11] W. Zhou, C. Yue, Y. Li, and Y. Xia, "A 5G gong-shaped circular-polarization antenna," *PIERS: Photonics and Electromagnetics Research Symposium, also known as Progress In Electromagnetics Research Symposium*, Hangzhou, 21-25, Nov., Hangzhou, China, 2021.
- [12] B. Qiu and Y. Li, "Gain-enhanced wideband circularly polarized antenna with a non-uniform metamaterial reflector," *Applied Computational Electromagnetics Society (ACES) Journal*, vol. 37, no. 3, pp. 281-286, Jul. 2022.
- [13] Y. Li and R. Mittra, "A three-dimensional circularly polarized antenna with a low profile and a wide 3-dB beamwidth," *Journal of Electromagnetic Waves and Applications*, vol. 30, no. 1, pp. 89-97, Jan. 2016.
- [14] B. Qiu, Y. Xia, Y. Li, C. Yue, and T. Jiang, "A compact wideband circularly polarized antenna for sub-6 GHz application," *IEEE 4th International Conference on Electronic Information and Communication Technology (ICEICT 2021)*, 18-20, Aug., Xian, China, 2021.
- [15] W. Zhou, C. Yue, Y. Li, Y. Xia, B. Qiu, and K. L. Chung, "A high gain Si-shaped circularly polarized patch antenna for 5G application," *IEEE 4th International Conference on Electronic Information and Communication Technology (ICEICT 2021)*, 18-20, Aug., Xian, China, 2021.
- [16] J. Jiang, C. Yue, Y. Xia, B. Qiu, and Y. Li, "A circularly-polarized Zhong-shaped MIMO antenna with meta-materials for WLAN application," *International Applied Computational Electromagnetics Society (ACES-China) Symposium*, 28-30, Jul., Chengdu, China, 2021.
- [17] B. Qiu, Y. Li, and Y. Xia, "Asymmetric CPW-fed wideband circularly polarized antenna for sub-6GHz application," *IEEE 3rd International Conference on Electronic Information and Communication Technology (ICEICT)*, 13-15, Nov., Shenzhen, China, 2020.
- [18] K. L. Chung, A. Cui, M. Ma, B. Feng, and Y. Li, "Central-symmetry decoupling technique

- for circularly-polarized MIMO system of tightly packed chinese-character-shaped patch antennas,” *Applied Computational Electromagnetics Society (ACES) Journal*, vol. 36, no. 9, pp. 1125-1131, Nov. 2021.
- [19] K. L. Chung, X. Yan, and Y. Li, “Circularly-polarized linear antenna array of non-identical radiating patch elements for WiFi/WLAN applications,” *AEU - International Journal of Electronics and Communications*, vol. 129, ID:153526, Feb. 2021.
- [20] W. He, Y. He, Y. Li, and L. Zhu, “A compact ultra-wideband circularly polarized antenna array with shared partial patches,” *IEEE Antennas and Wireless Propagation Letters*, vol. 20, no. 12, pp. 2280-2284, Dec. 2021.
- [21] J. Lin and Q. Chu, “Increasing bandwidth of slot antennas with combined characteristic modes,” *IEEE Transactions on Antennas and Propagation*, vol. 66, no. 6, pp. 3148-3153, Jun. 2018.
- [22] Q. S. Wu, X. Zhang, and L. Zhu, “A feeding technique for wideband CP patch antenna based on 90° phase difference between tapped line and parallel coupled Line,” *IEEE Antennas and Wireless Propagation Letters*, vol. 18, no. 7, pp. 1468-1471, Jul. 2019.
- [23] X. Zhang, L. Zhu, and N. Liu, “Pin-loaded circularly-polarized patch antennas with wide 3-dB axial ratio beamwidth,” *IEEE Transactions on Antennas and Propagation*, vol. 65, no. 2, pp. 521-528, Feb. 2017.
- [24] P. Nayeri, K. Lee, A. Z. Elsherbeni, and F. Yang, “Dual-band circularly polarized antennas using stacked patches with asymmetric U-slots,” *IEEE Antennas and Wireless Propagation Letters*, vol. 10, pp. 492-495, 2011.
- [25] Z. Zhao, F. Liu, J. Ren, Y. Liu and Y. Yin, “Dual-sense circularly polarized antenna with a dual-coupled line,” *IEEE Antennas and Wireless Propagation Letters*, vol. 19, no. 8, pp. 1415-1419, Aug. 2020.
- [26] M. K. Ray, K. Mandal, and N. Nasimuddin, “Low-profile circularly polarized patch antenna with Wide 3 dB beamwidth,” *IEEE Antennas and Wireless Propagation Letters*, vol. 18, no. 12, pp. 2473-2477, Dec. 2019.
- [27] Z. Zhao, J. Ren, Y. Liu, Z. Zhou, and Y. Yin, “Wideband dual-feed, dual-sense circularly polarized dielectric resonator antenna,” *IEEE Transactions on Antennas and Propagation*, vol. 68, no. 12, pp. 7785-7793, Dec. 2020.
- [28] J. Zeng, X. Liang, L. He, F. Guan, F. H. Lin, and J. Zi, “Single-fed triple-mode wideband circularly polarized microstrip antennas using characteristic mode analysis,” *IEEE Transactions on Antennas and Propagation*, vol. 70, no. 2, pp. 846-855, Feb. 2022.
- [29] C. S. Lee, Y. Fan, and M. Ezzat, “Single-feed circularly polarized microstrip antenna with bethe holes on the radiating patch,” *IEEE Transactions on Antennas and Propagation*, vol. 68, no. 6, pp. 4935-4938, Jun. 2020.
- [30] Y. S. Anjani and A. Alphones, “A Wide-beam circularly polarized asymmetric-microstrip antenna,” *IEEE Transactions on Antennas and Propagation*, vol. 63, no. 8, pp. 3764-3768, Aug. 2015, doi: 10.1109/TAP.2015.2438397.
- [31] J. Zhuang, Y. Zhang, W. Hong, and Z. Hao, “A broadband circularly polarized patch antenna with improved axial ratio,” *IEEE Antennas and Wireless Propagation Letters*, vol. 14, pp. 1180-1183, Jan. 2015.
- [32] X. Zhang and L. Zhu, “High-gain circularly polarized microstrip patch antenna with loading of shorting pins,” *IEEE Transactions on Antennas and Propagation*, vol. 64, no. 6, pp. 2172-2178, Jun. 2016.
- [33] C. X. Mao, S. S. Gao, Y. Wang, and J. T. S. Suman-tyo, “Compact broadband dual-sense circularly polarized microstrip antenna/array with enhanced isolation,” *IEEE Transactions on Antennas and Propagation*, vol. 65, no. 12, pp. 7073-7082, Dec. 2017.
- [34] R. Xu, J. Li, J. Yang, K. Wei, and Y. Qi, “A design of U-shaped slot antenna with broadband dual circularly polarized radiation,” *IEEE Transactions on Antennas and Propagation*, vol. 65, no. 6, pp. 3217-3220, Jun. 2017.
- [35] M. He, X. Ye, P. Zhou, G. Zhao, C. Zhang, and H. Sun, “A small-size dual-feed broadband circularly polarized U-slot patch antenna,” *IEEE Antennas and Wireless Propagation Letters*, vol. 14, pp. 898-901, Jan. 2015.
- [36] M. Khan and D. Chatterjee, “Analysis of reactive loading in a U-Slot microstrip patch using the theory of characteristic modes,” *IEEE Antennas and Propagation Magazine*, vol. 60, no. 6, pp. 88-97, Dec. 2018.
- [37] X. Chen, M. Zhao, H. Huang, Y. Wang, S. Zhu, C. Zhang, J. Yi, and A. A. Kishk, “Simultaneous decoupling and decorrelation scheme of MIMO arrays,” *IEEE Transactions on Vehicular Technology*, vol. 71, no. 2, pp. 2164-2169, Feb. 2022.
- [38] W. Shi, X. Liu, and Y. Li, “ULA fitting for MIMO radar,” *IEEE Communications Letters*, vol. 26, no. 9, pp. 2190-2194, Sep. 2022.
- [39] Y. Wang, X. Chen, X. Liu, J. Yi, J. Chen, A. Zhang, and A. Kishk, “Improvement of diversity

and capacity of MIMO system using scatterer array," *IEEE Transactions on Antennas and Propagation*, vol. 70, no. 1, pp. 789-794, Jan. 2022.

- [40] K. Yu, Y. Li, and X. Liu, "Mutual coupling reduction of a MIMO antenna array using 3-D novel meta-material structures," *Applied Computational Electromagnetics Society (ACES) Journal*, vol. 33, no. 7, pp. 758-763, Jul. 2018.
- [41] F. Liu, J. Guo, L. Zhao, G. L. Huang, Y. Li, and Y. Yin, "Dual-band metasurface-based decoupling method for two closely packed dual-band antennas," *IEEE Transactions on Antennas and Propagation*, vol. 68, no. 1, pp. 552-557, Jan. 2020.
- [42] L. Zhao, F. Liu, X. Shen, G. Jing, Y. Cai, and Y. Li, "A high-pass antenna interference cancellation chip for mutual coupling reduction of antennas in contiguous frequency bands," *IEEE Access*, vol. 6, pp. 38097-38105, Jul. 2018.
- [43] J. Li, X. Zhang, Z. Wang, X. Chen, J. Chen, Y. Li, and A. Zhang, "Dual-band eight-antenna array design for MIMO applications in 5G mobile terminals," *IEEE Access*, vol. 7, pp. 71636-71644, Apr. 2019.
- [44] F. Liu, J. Guo, L. Zhao, G. L. Huang, Y. Li, and Y. Yin, "Ceramic superstrate-based decoupling method for two closely packed antennas with cross-polarization suppression," *IEEE Transactions on Antennas and Propagation*, vol. 69, no. 3, pp. 1751-1756, Mar. 2021.



**Lulu Meng** was born in Henan, China. She received the B.S. degree in Electronics and Information Engineering from the Xinxiang University, Henan, China, in 2021. She is currently pursuing the M.S. degree in Communication and Information System with the Anhui University,

China. Her current research interests include circular polarization antenna design and metamaterials and its applications.



**Yingsong Li** received his B.S. degree in Electrical and Information Engineering and M.S. degree in Electromagnetic Field and Microwave Technology from Harbin Engineering University, 2006 and 2011, respectively. He received his Ph.D degree from both Kochi

University of Technology (KUT), Japan and Harbin Engineering University (HEU), China in 2014. He is currently a Full Professor with the School of Electronic

and Information Engineering of Anhui University from March 2022. He was a full Professor in Harbin Engineering University from 2014 to 2022 and a visiting scholar of University of California, Davis from March 2016 to March 2017, a visiting Professor of University of York, UK in 2018, a visiting Professor of Far Eastern Federal University (FEFU) and KUT. Now, he holds the visiting Professor position of School of Information of KUT from 2018. He is a Postdoc of Key Laboratory of Microwave Remote Sensing, Chinese Academy of Sciences from 2016 to 2021. Now, He is a Fellow of Applied computational Electromagnetics Society (ACES Fellow), and he is also a senior member of Chinese Institute of Electronics (CIE) and IEEE. He has authored and coauthored about 300 journal and conference papers in various areas of electrical and information engineering. His current research interests include signal processing, adaptive filters, metasurface designs and microwave antennas.

Dr. Li serves as an Area Editor of AEU-International Journal of Electronics and Communications from 2017 to 2020, and he is an Associate Editor of IEEE Access, Applied Computational Electromagnetics Society Journal (ACES Journal) and Alexandria Engineering Journal and Electromagnetic Science. He is the TPC Co-Chair of the 2019 IEEE International Workshop on Electromagnetics (iWEM 2019-2020), 2019 IEEE 2nd International Conference on Electronic Information and Communication Technology (ICEICT 2019), 2019 International Applied Computational Electromagnetics Society (ACES) Symposium-China, 2019 Cross Strait Quad-regional Radio Science and Wireless Technology Conference (2019 CSQRWC) and TPC Chair of ICEICT 2021-2022. He is also a General Co-Chair of ICEICT 2020 and a General Chair of IEEE 9th International Conference on Computer Science and Network Technology (ICCSNT 2021) and ICCSNT 2022. He is also a TCP member for many international and domestic conference. He also serves as a Session Chair or Organizer for many international and domestic conferences, including the WCNC, AP-S, ACES-China ect. He acts as a Reviewer of numerous IEEE, IET, Elsevier and other international journals and conferences.



**Zhixiang Huang** received his BS degree in Statistic and Probability and Ph.D. in Electromagnetic Field and Microwave Technology from Anhui University in 2002 and 2007, respectively. He is a Lecturer of Anhui University from 2007 to 2008 and is promoted to

Professor in 2008, and is a visiting scholar in Ames Laboratory, Iowa State University, from 2010 to 2011. Currently, he is a full Professor and the dean of the

School of Electronic Information Engineering of Anhui University, founder of Key Laboratory of Electromagnetic Environmental Sensing of Anhui Higher Education Institutes, director of the Young Scientists Club of Chinese Institute of Electronics (CIE), member of the Youth Working Committee of CIE. He is the recipient of the Outstanding Young Talent Project of National Natural Science Foundation of China (NSFC) in 2018 and the Chang Jiang Scholars Program of Ministry of Education of the People's Republic of China in 2022. He is a Senior Member of IEEE. He has more than 100 academic papers in peer-reviewed international/national journals. His current interests include theoretical and computational in electromagnetics and Microwave/RF circuit design, and multiphysics modeling.

# A Novel $4 \times 4$ MIMO Antenna Decoupled by T-Shaped Dummy Antenna with High Robustness for 5G Mobile Devices

Junlin Wang, Xiaomin Chen, Xin Wang, and Min Wei

School of Electronic Information Engineering  
Inner Mongolia University, Hohhot, 010021, China  
wangjunlin@imu.edu.cn, chenxiaomin\_ee@163.com  
wangxin219@imu.edu.cn, 18709836689@163.com

**Abstract** – It is challenging to design a compact antenna pair with isolation better than 20 db and with robustness to antenna position. In this paper, a T-shaped dummy antenna is adopted to decouple the tightly arranged antenna pair for 5G mobile devices. Working in the 3.8 GHz of N77 band, the proposed antenna pair is with an impedance bandwidth of 280 MHz. Isolation of the proposed antenna pair is enhanced from 13 db to 30 db by adding the T-shaped dummy antenna, and it is with high robustness even though the antenna position is altered. The calculation process of the loading requirement of T-shaped dummy antenna is shown. By duplicating the proposed antenna pair, a  $4 \times 4$  MIMO antenna with high isolation is proposed. The measured results show the MIMO antenna with isolation better than 31 db, and the average total efficiency is about 49%, and the Envelope Correlation Coefficient (ECC) is lower than 0.05 in the -6 db pass band. To the best of the authors' knowledge, compared to most of the reported antenna pairs, the proposed  $4 \times 4$  MIMO antenna is with the highest isolation while keeping a compact size.

**Index Terms** – compact antenna pair, decoupling, 5G, high isolation, T-shaped dummy antenna.

## I. INTRODUCTION

Multiple-input multiple-output (MIMO) technology is one of the most promising technologies in upcoming 5G mobile communication. One of the mid-bands of sub-6G, N77 (3.3-4.2 GHz), is a good candidate for 5G mobile devices. Recently, many researchers have focused on the MIMO antenna for 5G mobile devices, such as smartphones and tablets. In [1]-[10], many researchers have proposed MIMO antenna with isolation of about 10 db. However, due to the space limitation of the terminal devices, it is challenging to design a MIMO antenna with high isolation level and low envelope correlation coefficient (ECC). In [11], the isolation of the multi-band/UWB-MIMO antenna has been enhanced by insert-

ing an RSLR loaded T-shaped stub between two identical triple notch band antennas. But its isolation is only 15 db, which is not enough for high isolation equipment.

The techniques to enhance the isolation of MIMO antenna are varied, including defected ground structure (DGS) [14], electromagnetic band gap (EBG) [15], dielectric block (DB) [16], decoupling network [17], and neutralization line (NL) [18]. However, it is not recommended to introduce a sizable dielectric block into 5G mobile devices or disrupt the system's ground integrity. Utilizing the intrinsic high isolation between two antenna elements is a good choice for 5G mobile devices [19]-[22]. In [19], orthogonal-mode dual antenna pair with isolation of 20 db is proposed under the size of  $0.18 \lambda \times 0.08 \lambda$ ; in [20], a dipole antenna pair is designed with an isolation of 24 db under the size of  $0.33 \lambda \times 0.06 \lambda$  by using the differential/common mode; in [21], a tightly arranged orthogonal-mode pair is realized with isolation of 20 db under the size of  $0.14 \lambda \times 0.08 \lambda$ ; in [22], two asymmetrically mirrored gap-coupled loop antennas are proposed with isolation of 10 db under the size of  $0.12 \lambda \times 0.08 \lambda$ . However, controlling the orthogonal modes of the antenna is a very complex task, if not controlled, then the isolation of the antenna pair is only 10 db [22]. Another way to decouple the MIMO antenna is by adding the planar microstrip structure [23], [24]. In [23], by adding a series of microstrip lines, the isolation of the antenna pair is enhanced to 21 db under the volume  $0.80 \lambda \times 0.07 \lambda$  with independent tuning characteristics; in [16], neutralization line is adopted to decouple the adjacent antenna and the antenna pair is with isolation of 11.5 db under the volume of  $0.53 \lambda \times 0.08 \lambda$ . However, these MIMO antennas have occupied a large region along the two long side edges of the system circuit board, which may not be suitable for a smartphone with widescreen size.

More importantly, antenna isolation is related to the antenna position because of the ground effect, and it can be dramatically reduced when placing the antenna in a different position [19]. It will significantly improve

the antenna performance if isolation is highly robust to antenna position. So far, this problem has seldom been studied.

In this paper, a novel antenna pair decoupled by a T-shaped dummy antenna with high isolation and robustness is proposed. The loading requirement  $Z_L$  of the T-shaped dummy antenna is calculated, and the corresponding results are shown. Working in the 3.8 GHz of N77 band, the proposed decoupled antenna pair is within an impedance bandwidth of 280 MHz and isolation of 30 db. By duplicating the antenna pair, a 4×4 MIMO antenna is realized, and the measured results show that the isolation is better than 31 db. The measured average total efficiency is 49% and the Envelope Correlation Coefficient (ECC) is lower than 0.05. The proposed antenna has great potential to be applied in 5G mobile terminals.

## II. DECOUPLING PRINCIPLE AND THE PROPOSED ANTENNA PAIR

### A. Decoupling principle

In Fig. 1, the decoupling diagram of using dummy antenna is illustrated. Port 1 and Port 2 is connected to Antenna 1 and Antenna 2, respectively. When two antenna are placed closely, coupling current  $I_{couple1}$  (coupling current is out-of-phase compared to the original current) will exist through the coupling path#1. The performance of Antenna 2 will be deteriorated due to the out-of-phase coupling current. To counteract this coupling current, we introduce an additional coupling current by adding a dummy antenna. As shown at the top of Fig. 1, the dummy antenna is with impedance loading of  $Z_L$ . Antenna 1 couples the dummy antenna through path#2 and coupling current  $I_{couple2}$  is created

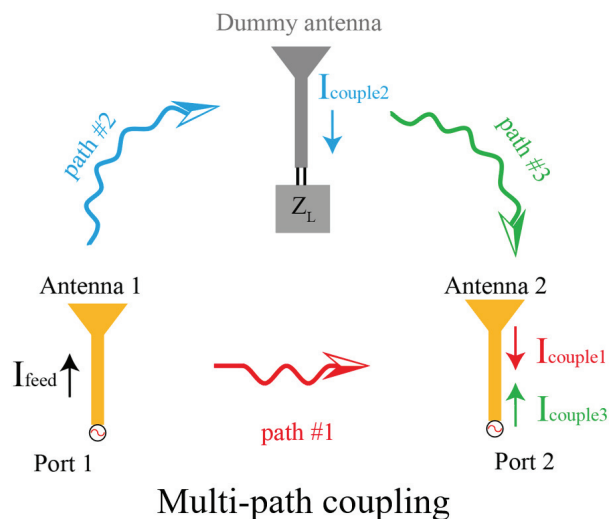


Fig. 1. Decoupling diagram by using dummy antenna.

correspondingly. Energy is then transmitted from the dummy antenna to Antenna 2 through path#3, resulting in  $I_{couple3}$ . It should be emphasized that  $I_{couple1}$  and  $I_{couple3}$  have opposite direction. If the amplitude of  $I_{couple1}$  is equal to the amplitude of  $I_{couple3}$ , they can cancel each other out.

$$R_L = \text{Re}\{Z_L\} = \text{Re}\left\{\frac{Z_{12}Z_{23}}{Z_{13}}\right\} - R_{22}, \quad (1)$$

$$X_L = \text{Im}\{Z_L\} = \text{Im}\left\{\frac{Z_{12}Z_{23}}{Z_{13}}\right\} - X_{22}. \quad (2)$$

It is demonstrated in [25] that the coupled antenna can realize zero-coupling condition when adding dummy antenna and loading the  $Z_L$  of Fig. 1 calculated by (1) and (2). The  $R_L$  and  $X_L$  represent the real part and imaginary part of the  $Z_L$ . When the real part and imaginary part of the  $Z_L$  is exactly the right size of (1) and (2), respectively, then Antenna 1 and 2 are isolated. For brevity, the detailed analysis will not be shown here. It should be noted that when calculating the  $R_L$  and  $X_L$ , the dummy antenna is terminated as Port 3 in CST 2021. Therefore, in (1) and (2), the number “3” indicates the parameter of dummy antenna, i.e.,  $Z_{n3}$  ( $n \neq 3$ ) represents the mutual impedance of the dummy antenna. After calculating the required loading impedance of the dummy antenna, a corresponding lumped element will be connected to the dummy antenna, so that the coupling current between Antenna 1 and Antenna 2 will be canceled, thus obtaining high isolation. This process will be shown later.

### B. Configuration of the 4×4 MIMO antenna

Figure 2 shows the geometry of the 4×4 MIMO antenna for 5G terminal devices. A 0.8-mm-thick FR4 substrate ( $\epsilon_r = 4.4$ ,  $\tan\delta = 0.02$ ) is used as the main circuit board and two 0.8-mm-thick FR4 substrates are adopted to imitate the realistic bezels. The mainboard is perpendicular to the two bezels. The dimension of the mainboard is 150×75 mm<sup>2</sup> and is with 1 mm ground clearance. The detailed size is shown in Fig. 2 (b), where the side plate is double-sided copper clad. Ant. 1, Ant. 2, and the T-shaped dummy antenna are etched on the outside of the side substrate, while the feeding point A, B, and shorting point C are etched on the inside. In the upper part of the motherboard, an inductor and resistor, which has the required  $Z_L$  loading calculated by (1) and (2), is connected to the dummy antenna through the metallic via marked as point D. To better illustrate the connecting relationship, the enlarged view of the fabricated prototype is shown in Fig. 2 (c).

### C. Performance of adding the T-shaped dummy antenna

First, the antenna pair in Fig. 3 (a) has no T-shaped dummy antenna, which is with the impedance bandwidth of 230 MHz and the isolation is about 13 db. However, this is obviously not enough for high isolation MIMO

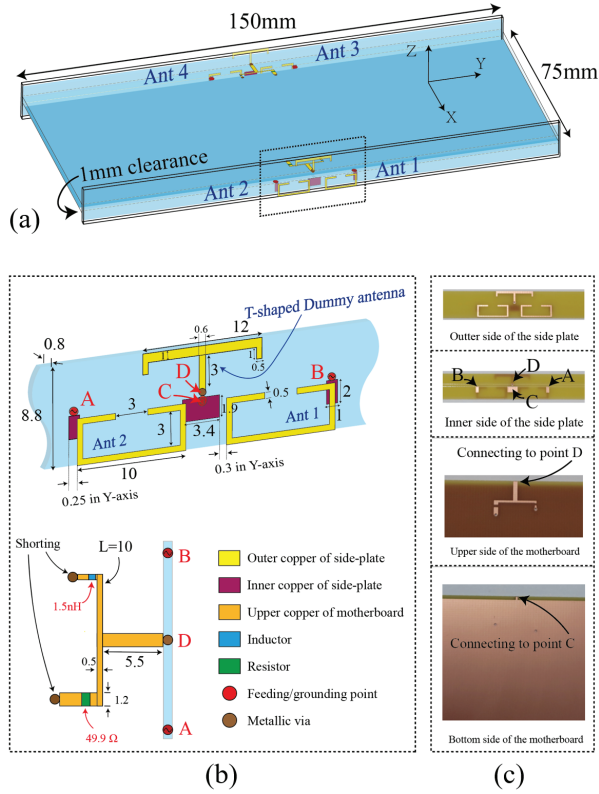


Fig. 2. (a) Configuration of the proposed 4×4 MIMO antenna, (b) zoom-in view of the proposed antenna pair and (c) photos of the fabricated substrate.

antennas [19]-[21]. The T-shaped dummy antenna is then added above the antenna pair. Here, we use CST 2021 to calculate the loading requirement of the dummy antenna. In Figs. 3 (b) and (c), it is observed that the required loading value is  $\{X_L, R_L\} = \{0.5 \text{ nH}, 50 \Omega\}$ . Shown in Fig. 3 (d), after adding the T-shaped dummy antenna and

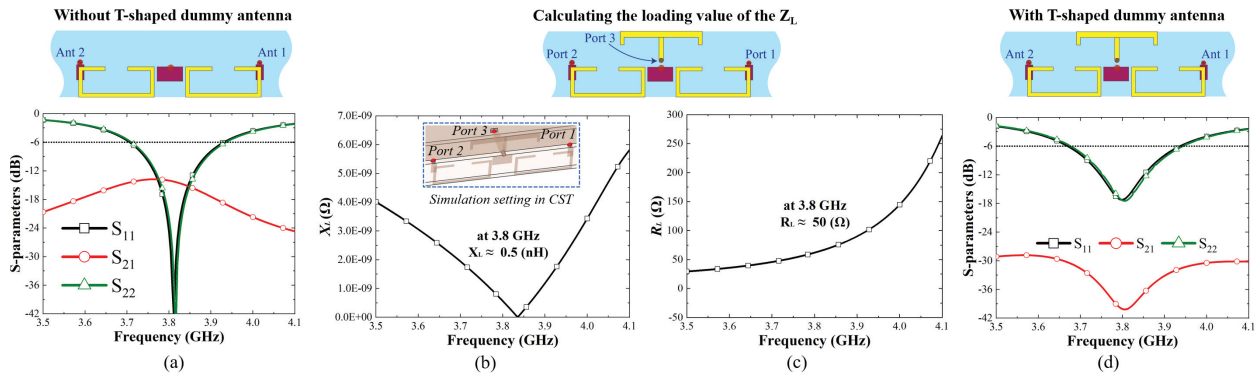


Fig. 3. (a) Simulated results of antenna pair without T-shaped dummy antenna; (b) and (c) is the simulated loading requirement of the T-shaped dummy antenna, and (d) is the simulated result of antenna pair with T-shaped dummy antenna.

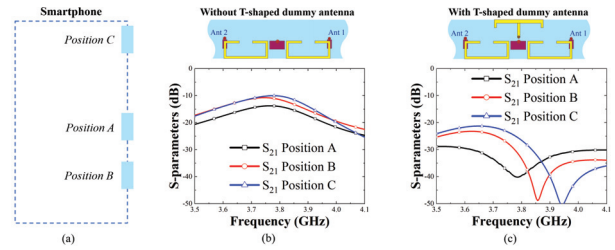


Fig. 4. S-parameter of proposed antenna pair located in different places, (a) antenna placing diagram, (b) S-parameters of the antenna pair without T-shaped dummy antenna and (c) S-parameters of antenna pair with T-shaped dummy antenna.

loading the lumped elements of 0.5 nH and 49.9 Ω, the isolation of the antenna pair is enhanced to -30 db and the impedance bandwidth is 270 MHz (17% better than before).

Furthermore, the T-shaped decoupled dummy antenna is with robustness. As shown in Fig. 4, when the antenna pair is in a different place, such as position A and B, and C, the isolation of the antenna will change dramatically. At position C, the isolation of the antenna without the T-shaped dummy antenna is only 9 db. After the decoupling of the T-shaped dummy antenna, the isolation is still better than at 22 db even at different positions. It should be noted that the reflection coefficient of Ant. 1 and 2 is almost unchanged when the antenna is in a different place.

### III. RESULTS OF THE PROPOSED 4×4 MIMO ANTENNA

#### A. Simulated results

By duplicating the antenna pair, a 4×4 MIMO antenna is realized. Figure 5 shows the simulated results

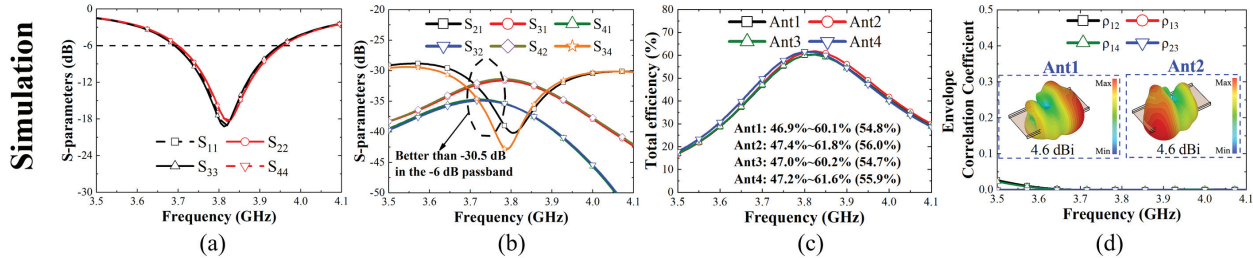


Fig. 5. Simulated results of (a) reflection coefficients, (b) transmission coefficients, (c) total efficiencies, and (d) envelope correlation coefficient.

Table 1: Performance comparison of the reported antenna pair

Ref.	Size/ $\lambda^2$	Design Difficulty	Isolation	Efficiency	Worst Isolation with Different Position
[19]	0.0144	Not easy	20 db	> 45%	14 db
[20]	0.0198	Not easy	24 db	> 61%	N.G.
[23]	0.0560	Not easy	21 db	> 50%	N.G.
[24]	0.0424	Easy tuning	12 db	> 40%	N.G.
Ours	0.0310	Easy for calculating	31 db	> 45%	22 db

“N.G.” means that the data is not given.

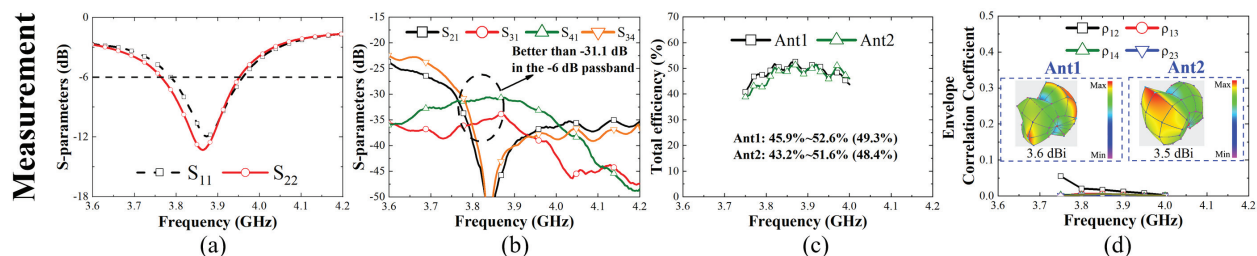


Fig. 6. Measured results of (a) reflection coefficients, (b) transmission coefficients, (c) total efficiencies, and (d) envelope correlation coefficient.

of the proposed 4×4 MIMO antenna. The impedance bandwidth of the antenna is 270 MHz. After the decoupling of the T-shaped dummy antenna, the performance of  $S_{21}$  and  $S_{43}$  are greatly improved, and the worst isolation of any two antennas is 30.5 db. The average total efficiency of the antenna is 55% and the ECC is lower than 0.01 in the -6 db pass band. The high isolation between two antenna blocks, such as  $S_{31}$  and  $S_{41}$ , is obtained by the characteristic of pattern diversity, which means that the Ant. 3 and 4 is located in the radiated null of Ant. 1 and 2.

## B. Measured results

To verify the feasibility, the proposed antenna is fabricated and measured by a Keysight 5071C vector network analyzer. The measured data is shown in Fig. 6. Because the antenna is symmetrical, we only show the data of Ant. 1 and 2. As shown in Fig. 6 (a), the center

frequency of Ant. 1 and 2 is shifted by about 50 MHz, which is mostly caused by hand-made error. The isolation of the MIMO antenna in the -6 db pass band is better than -31.1 db. The measured average total efficiency of the antenna is 49% and the ECC is lower than 0.05. In the illustration of Fig. 6 (d), we show the measured 3D pattern of the antenna. The measured results are in high agreement with the simulated ones.

The fabricated prototype and measurement setup is shown in Fig. 7. The proposed antenna pair is connected to a 50  $\Omega$  semi-rigid cable, where its outer side is connected to ground.

## C. Performance comparison

To show the superiority of the design strategy, performance comparison including electrical size, design difficulty, isolation, efficiency, and the worst isolation with different antenna position is given in Table 1. It

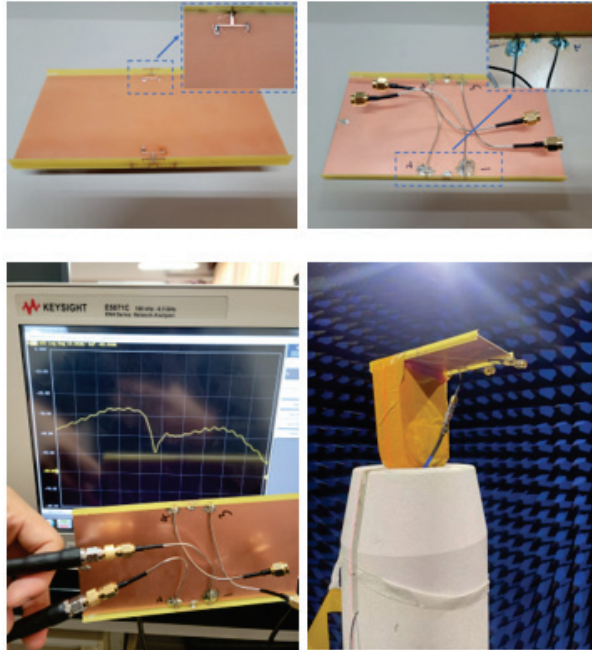


Fig. 7. Fabricated prototype and measurement setup.

is observed that the proposed antenna pair obtain the highest isolation of 31 db in a compact size. The tuning process is easy and relatively high antenna efficiency is obtained. More importantly, the proposed antenna pair still has high isolation when the antenna position changes. The proposed  $4 \times 4$  MIMO antenna has great potential to be applied in 5G mobile devices.

Furthermore, in [12], a method to miniaturize the aperture of a dual-polarized Quadruple-Folded-Dipole (QFD) antenna by bending its arms downward or upward is proposed. Both antennas can achieve relatively small apertures while ensuring good matching, isolation and radiation performances within the band of interest. In [13], a ceramic superstrate-based decoupling method (CSDM) is proposed to reduce the mutual coupling between two closely packed dipole antennas while maintaining cross-polarization suppression. However, they have one disadvantage: the decoupled dipole is relatively large in volume, and is placed vertically, which is suitable for application to base station antennas. Our design is mainly aimed at 5G terminal equipment, with small size, low height and high isolation. Based on practical applications, we think our design is more suitable for 5G terminal devices.

#### IV. CONCLUSION

In this paper, a compact antenna pair with high isolation and robustness to antenna position for 5G mobile devices is proposed and analyzed. The proposed antenna pair comprises of an antenna pair with pattern diversity

characteristics and a compact T-shaped decoupling structure. By duplicating the proposed antenna pair, a  $4 \times 4$  MIMO antenna is realized. The isolation and robustness of the MIMO antenna are improved by introducing an impedance-loaded T-shaped decoupling dummy antenna. The measurement results of the proposed MIMO antenna show that it is with isolation of 31 db. The measured average antenna efficiency is 49% and the ECC is below 0.05. The proposed MIMO antenna has great potential for application in 5G mobile devices.

#### REFERENCES

- [1] M.-Y. Li, Y.-L. Ban, Z.-Q. Xu, C.-Y. Sim, K. Kang, and Z.-F. Yu, "Eight-port orthogonally dual-polarized antenna array for 5G smartphone applications," *IEEE Trans. Antennas Propag.*, vol. 64, no. 9, pp. 3820-3830, Sep. 2016.
- [2] K. L. Wong, J.-Y. Lu, L.-Y. Chen, W.-Y. Li, and Y.-L. Ban, "8-antenna and 16-antenna arrays using the quad-antenna linear array as a building block for the 3.5-GHz LTE MIMO operation in the smartphone," *Microw. Opt. Technol. Lett.*, vol. 58, no. 1, pp. 174-181, Jan. 2016.
- [3] Y. Li, C.-Y.-D. Sim, Y. Luo, and G. Yang, "12-port 5G massive MIMO antenna array in sub-6 GHz mobile handset for LTE bands 42/43/46 applications," *IEEE Access*, vol. 6, no. 9, pp. 344-354, Oct. 2017.
- [4] Z. Qin, W. Geyi, M. Zhang, and J. Wang, "Printed eight-element MIMO system for compact and thin 5G mobile handset," *Electron. Lett.*, vol. 52, no. 6, pp. 416-418, Mar. 2016.
- [5] Y.-L. Ban, C. Li, C.-Y.-D. Sim, G. Wu, and K.-L. Wong, "4G/5G multiple antennas for future multi-mode smartphone applications," *IEEE Access*, vol. 4, pp. 2981-2988, Jul. 2016.
- [6] Y. H. Wang, X. Wang, J. L. Wang, and R. Shao, "Dual-band highly isolated eight-element MIMO antenna for 5G mobile phone," *Applied Computational Electromagnetics Society (ACES) Journal*, vol. 37, no. 5, pp. 588-596, Nov. 2022.
- [7] N. O. Parchin, O. M. Dardeer, A. S. Amar, C. H. See, and R. Abd-Alhameed, "Dual-band phased array 5G mobile-phone antenna with switchable and hemispherical beam pattern coverage for MIMO-diversity communications," *Applied Computational Electromagnetics Society (ACES) Journal*, vol. 36, no. 12, pp. 1602-1609, Mar. 2022.
- [8] G. We and Q. Feng, "Side-frame dual-band MIMO antennas for 5G smartphone applications," *Applied Computational Electromagnetics Society (ACES) Journal*, vol. 35, no. 11, pp. 1314-1315, Nov. 2020.
- [9] Z. An and M. He, "A multiband dual-antenna system for MIMO operation in mobile terminals,"

- Applied Computational Electromagnetics Society (ACES) Journal*, vol. 34, no. 10, pp. 1529-1534, Oct. 2019.
- [10] R. M. Asif, A. Aziz, M. Amjad, Majid N. Akhtar, A. Baqir, and M. N. Abbasi, "Analysis and design of an efficient and novel MIMO antenna for 5G smart phones using FDTD and FEM," *Applied Computational Electromagnetics Society (ACES) Journal*, vol. 36, no. 3, pp. 266-272, Mar. 2021.
- [11] Y. Li, W. Li, and W. Yu, "A multi-band/UWB MIMO/diversity antenna with an enhanced isolation using radial stub loaded resonator," *Applied Computational Electromagnetics Society (ACES) Journal*, vol. 28, no. 1, pp. 8-20, Jan. 2013.
- [12] H. Yang, G. Zhao, J. Jiang, T. Liu, L. Zhao, Y. Li, Y. Cai, and J. Yao. "Aperture reduction using downward and upward bending arms for dual-polarized quadruple-folded-dipole antennas," *IEEE Antennas and Wireless Propagation Letters*, vol. 22, no 3, pp. 645-649, Mar. 2023.
- [13] F. Liu, J. Guo, L. Zhao, G.-L. Huang, Y. Li, and Y. Yin, "Ceramic superstrate-based decoupling method for two closely packed antennas with cross-polarization suppression," *IEEE Trans. Antennas Propag.*, vol. 69, no. 3, pp. 1751-1756, Mar. 2021.
- [14] C.-Y. Chiu, C.-H. Cheng, R. D. Murch, and C. R. Rowell, "Reduction of mutual coupling between closely-packed antenna elements," *IEEE Trans. Antennas Propag.*, vol. 55, no. 6, pp. 1732-1738, Jun. 2007.
- [15] F. Yang and Y. Rahmat-Samii, "Microstrip antennas integrated with electromagnetic band-gap (EBG) structures: A low mutual coupling design for array applications," *IEEE Trans. Antennas Propag.*, vol. 51, no. 10, pp. 2936-2946, Oct. 2003.
- [16] M. Li, M. Y. Jamal, L. Jiang, and K. L. Yeung, "Isolation enhancement for MIMO patch antennas sharing a common thick substrate: Using a dielectric block to control space-wave coupling to cancel surface-wave coupling," *IEEE Trans. Antennas Propag.*, vol. 69, no. 4, pp. 1853-1863, Apr. 2021.
- [17] S. C. Chen, Y. S. Wang, and S. J. Chung, "A decoupling technique for increasing the port isolation between two strongly coupled antennas," *IEEE Trans. Antennas Propag.*, vol. 56, no. 12, pp. 3650-3658, Dec. 2008.
- [18] A. Diallo, C. Luxey, P. Le Thuc, R. Staraj, and G. Kossiavas, "Study and reduction of the mutual coupling between two mobile phone PIFAs operating in the DCS1800 and UMTS bands," *IEEE Trans. Antennas Propag.*, vol. 54, no. 11, pp. 3063-3074, Nov. 2006.
- [19] L. Chang, Y. Yu, K. Wei, and H. Wang, "Orthogonally polarized dual antenna pair with high isolation and balanced high performance for 5G MIMO smartphone," *IEEE Trans. Antennas Propag.*, vol. 68, no. 5, pp. 3487-3495, May 2020.
- [20] H. Xu, S. S. Gao, H. Zhou, H. Wang, and Y. Cheng, "A highly integrated MIMO antenna unit: Differential/common mode design," *IEEE Trans. Antennas Propag.*, vol. 67, no. 11, pp. 6724-6734, Nov. 2019.
- [21] L. Sun, H. Feng, Y. Li, and Z. Zhang, "Compact 5G MIMO mobile phone antennas with tightly arranged orthogonal-mode pairs," *IEEE Trans. Antennas Propag.*, vol. 66, no. 11, pp. 6364-6369, Nov. 2018.
- [22] K.-L. Wong, C.-Y. Tsai, and J.-Y. Lu, "Two asymmetrically mirrored gap-coupled loop antennas as a compact building block for eight-antenna MIMO array in the future smartphone," *IEEE Trans. Antennas Propag.*, vol. 65, no. 4, pp. 1765-1778, Apr. 2017.
- [23] H. Xu, H. Zhou, S. Gao, H. Wang, and Y. Cheng, "Multimode decoupling technique with independent tuning characteristic for mobile terminals," *IEEE Trans. Antennas Propag.*, vol. 65, no. 12, pp. 6739-6751, Dec. 2017.
- [24] J. Guo, L. Cui, C. Li, and B. Sun, "Side-edge frame printed eight-port dual-band antenna array for 5G smartphone applications," *IEEE Trans. Antennas Propag.*, vol. 66, no. 12, pp. 7412-7417, Dec. 2018.
- [25] B. K. Lau and J. B. Andersen, "Simple and efficient decoupling of compact arrays with parasitic scatterers," *IEEE Trans. Antennas Propag.*, vol. 60, no. 2, pp. 464-472, Feb. 2012.



**Junlin Wang** received his PhD degree in Instrument Science and Technology from North University of China. He is currently working at the School of Electronic Information Engineering, Inner Mongolia University, Hohhot, China. His research interests are in micro and nano RF devices (antennas, filters, couplers, etc.), and metamaterial antennas.



**Xiaomin Chen** received his B.E. degree in Electronic Information Science and Technology from Shaoguan University. He is currently pursuing a master's degree in Information and Communication Engineering at Inner Mongolia University, Hohhot, China. His research interest is in 5G mobile terminal antennas.



**Xin Wang** received her PhD degree in Instrument Science and Technology from North University of China. She is currently working at the School of Electronic Information Engineering, Inner Mongolia University, Hohhot, China. Her research interests are in micro and nano RF devices (antennas, filters, couplers, etc.), and metamaterial antennas.



**Min Wei** received her B.E. degree in Electronic Information Science and Technology from Hexi University. She is currently pursuing a master's degree in Information and Communication Engineering at Inner Mongolia University, Hohhot, China. Her current research interest is in 5G mobile terminal antennas.

# High-Isolated Full-Duplex Dongle Antenna Based on Even-Mode Suppression for B5G Communications

Yiran Da<sup>1</sup>, Xiaoming Chen<sup>1</sup>, Aofang Zhang<sup>2</sup>, Kunpeng Wei<sup>2</sup>, and Ahmed A. Kishk<sup>3</sup>

<sup>1</sup>School of Information and Communications Engineering  
Xi'an Jiaotong University, Xi'an, 710049, China  
dyr916@stu.xjtu.edu.cn, xiaoming.chen@mail.xjtu.edu.cn

<sup>2</sup>Honor Device Co. Ltd, Beijing, 100095, China  
aofangzhang@foxmail.com, weikunpeng\_2013@tsinghua.org.cn

<sup>3</sup>Concordia University, Montreal, QC H3G 1M8, Canada  
kishk@encs.concordia.ca

**Abstract** – A space-shared full-duplex antenna with high isolation is proposed for universal serial bus (USB) dongles. A compact antenna with a compact size of 22 mm × 4 mm comprises a loop and dipole antennas, working as a vertical monopole and a horizontal dipole, respectively. The dipole-type is fed by a microstrip-slotline transition with filtering characteristics of odd-mode bandpass and even-mode bandstop, avoiding the even-mode excitation for the loop antenna. The inherent isolation is caused by the orthogonality of the modes and the even-mode suppression (caused by the microstrip-slotline transition). Thus, high port isolation, low envelope correlation coefficients (ECC), and high efficiency are achieved across the 5G band of 3.4-3.6 GHz.

**Index Terms** – even-mode suppression, full-duplex dongle antenna, high isolation.

## I. INTRODUCTION

With the growing demands for mobile communication, the fifth-generation (5G) communication technology has become famous for its high capacity and low latency [1]. The 5G antennas have been extensively studied [2]. A universal serial bus (USB) dongle is an Internet access module with a USB interface that can provide a network connection for laptops. Full-duplex antennas could effectively multiply the spectrum efficiency by transmitting and receiving signals within the same frequency band and time slot [3, 4], making them a key enabler for beyond 5G (B5G) technology. Therefore, compact full-duplex antennas are highly desirable for USB dongles. For reliable full-duplex communications, a 100-dB isolation between the transmitter and receiver is typically

required. Such high isolation is usually achieved by a combination of antenna isolation enhancement, analog filtering, and digital interference cancellation [5]. Therefore, antennas with high isolations (> 25 dB) are desired to relieve the pressure on the sequential processing and improve the dynamic range of the wireless connectivity [6, 7].

Various isolation improvement methods have been proposed for closely arranged antennas [8–26]. The first type is the decoupling method based on partition, such as electromagnetic bandgap structure [8, 9], decoupling resonators [10, 11], and defected ground structures [12, 13]. The second type is the decoupling method based on neutralization, such as array decoupling surface [14], decoupling ground [15–17], dielectric superstrate [18, 19], and decoupling networks [20, 21]. The partition and neutralization based decoupling methods are combined in [22] to enhance the decoupling bandwidth. In these papers, the antenna elements are separated, and the additional decoupling structures occupy extra specified space, making them less suitable for USB dongles. In [23], good isolation is obtained by sharing one common grounding branch for two adjacent antennas. The orthogonal modes of the antenna pair are utilized to improve the isolation in [24, 25]. Although the self-decoupling is achieved within a compact space, spatial reuse is still not well addressed, and, more importantly, the resulting isolations are insufficient for full-duplex communications. The mode cancellation method has been proposed to decouple the patch antenna pair with the shared radiator [26]. However, the operating frequency band is narrow. It is necessary to enhance the port isolation further to meet the higher requirement of full-duplex communication. Performance comparisons of different terminal antennas are shown in Table 1.

Table 1: Performance comparison

Ref.	Freq. (GHz)	Ant. Size (mm <sup>2</sup> )	Isolation	Effi.	ECC
[23]	3.4-3.6	20×7	17 db	58%	0.1
[25]	3.4-3.6	12×7	20 db	51%/74%	0.06
[26]	4.8-4.9	15.4×15.5	25 db	80%	0.02
This work	3.4-3.6	22×4	30 db	79%/64%	0.003

For fairness, the size and isolation of the compact arranged antenna pair are compared instead of MIMO antennas.

The microstrip-slotline transition structures are usually employed for filtering antennas, whose inherent characteristic of common-mode suppression can simplify the design procedure of the filtering antennas (only differential-mode passband performance needs to be studied) [27, 28]. In this paper, and different from previous papers, the microstrip-slotline transition structure is utilized to improve the isolation of the full-duplex antenna pair.

Here, a high-isolated full-duplex antenna for USB dongles is proposed, which consists of a tightly arranged loop antenna (vertical monopole mode) and dipole antenna (horizontal dipole mode). The dipole is fed by a  $\Gamma$ -shaped microstrip-slotline transition, avoiding the even-mode excitation of the loop antenna and maintaining the odd-mode feeding for the dipole. High port isolation is obtained owing to the mode orthogonality of the elements and the even-mode suppression of the microstrip-slotline transition. Within the operating frequency band of 3.4-3.6 GHz, high isolation ( $> 30$  db) and low envelope correlation coefficient (ECC) ( $< 0.003$ ) are achieved, exhibiting superior performances.

## II. HIGH-ISOLATED FULL-DUPLEX DONGLE ANTENNA WITH MICROSTRIP-SLOTLINE TRANSITION

### A. Array configuration

The configuration of the proposed full-duplex antenna is shown in Fig. 1 (a), which is composed of a loop antenna (Antenna 1) and a dipole antenna (Antenna 2). The loop antenna and the  $\Gamma$ -shaped microstrip feeding line are printed on the top side of the F4B substrate (with a relative permittivity of 4.4, a loss tangent of 0.002, and a thickness of 1 mm), while the dipole-type antenna and the ground plane are printed on the bottom side of the F4B substrate. The arms of the dipole are bent to reduce the antenna size. The two independent elements are tightly arranged in a single board of 22 mm × 4 mm,

simultaneously serving as the receiving and transmitting antennas. As shown in Fig. 1 (b), one end of the loop antenna is shorted to the ground plane, and a coaxial cable directly feeds the other end (Port 1). A  $\Gamma$ -shaped microstrip-slotline transition feeds the dipole antenna. The slotline on the ground plane of the FR4 substrate intersects orthogonally with the  $\Gamma$ -shaped microstrip line on the opposite interface, forming a transition from the microstrip feeding line to the slotline.

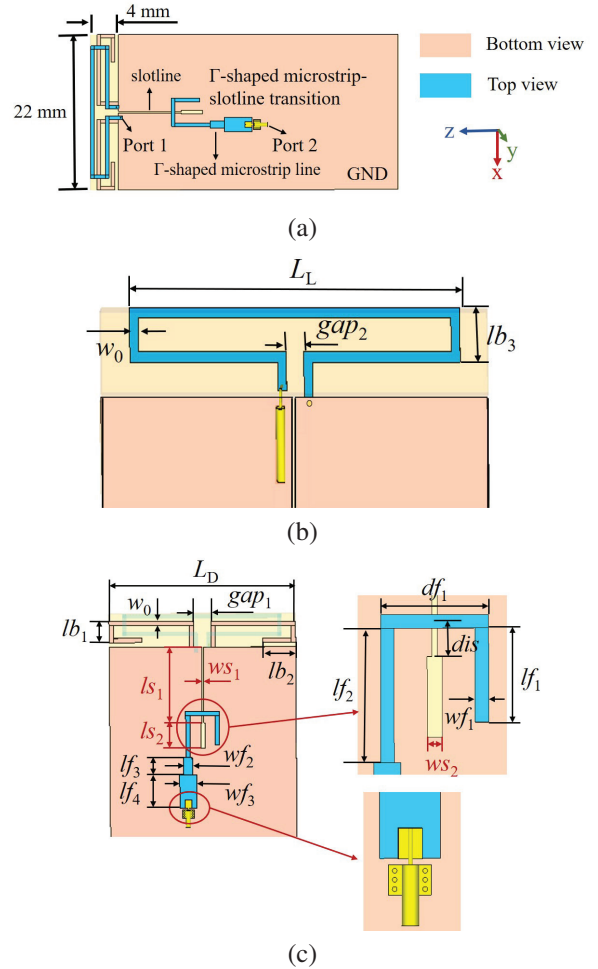


Fig. 1. Configurations of (a) Proposed full-duplex dongle antenna, (b) Loop antenna (Antenna 1), and (c) Dipole (Antenna 2). Optimized parameters are:  $L_D = 22$ ,  $L_L = 18.8$ ,  $w_0 = 0.5$ ,  $gap_1 = 2$ ,  $gap_2 = 1$ ,  $lb_1 = 2.5$ ,  $lb_2 = 3.9$ ,  $lb_3 = 2.6$ ,  $ls_1 = 9$ ,  $ls_2 = 3$ ,  $ws_1 = 0.2$ ,  $ws_2 = 0.55$ ,  $lf_1 = 3.5$ ,  $lf_2 = 5$ ,  $lf_3 = 2$ ,  $lf_4 = 4$ ,  $df_1 = 4$ ,  $wf_1 = 0.5$ ,  $wf_2 = 1$ ,  $wf_3 = 2$ ,  $dis = 1$  (all dimensions in mm).

The current distributions of Antennas 1 and 2 at the center frequency (3.5 GHz) are shown in Figs. 2 (a) and (b), respectively. On the dipole, the currents along the dipole arms parallel to the ground plane edge are in the same direction and at the feeding region are opposite

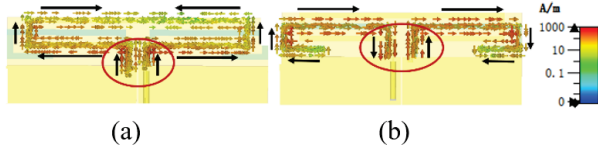


Fig. 2. Surface current distributions at 3.5 GHz. (a) Loop antenna excited by Port 1 (monopole mode). (b) Dipole antenna excited by Port 2 (dipole mode).

to each other (circled), exhibiting odd-mode excitation, while the currents flowing on the loop edges parallel to the ground plane edge are opposite to each other and at the feeding region are on the same direction exhibiting an even-mode excitation. Thus, the loop antenna operates as a vertical monopole. Therefore, the dipole antenna works as a horizontal dipole. Due to the orthogonal current mode of Antenna 1 (vertical monopole mode) and Antenna 2 (horizontal dipole mode), the mutual coupling between the two elements is reduced, thus, improving the port isolation of the full-duplex antenna. To further enhance the port isolation, the  $\Gamma$ -shaped microstrip-slotline transition is utilized to feed the dipole antenna, avoiding the even-mode excitation for the loop antenna and maintaining the odd-mode feeding for the dipole antenna.

**B. Microstrip-slotline transition**

Figure 3 illustrates the electric field distributions of the microstrip-slotline transition. Under the odd-mode excitation, two ends of the microstrip line are excited with equal amplitude and opposite phases. Thus, the electric fields distributed on both sides of the slotline are opposite, as shown in Fig. 3 (a). A virtual electric wall is produced at the center of the slotline, and a vertical electric field is generated through strong magnetic coupling. Therefore, the odd-mode signal flowing along the microstrip can be transformed into the slotline mode (vertical electric field) and transmitted to the antenna along the slot. Under the even-mode excitation, the two ends of the microstrip line are excited with equal amplitude and phase. Therefore, the directions of the electric fields on both sides of the slotline are the same,

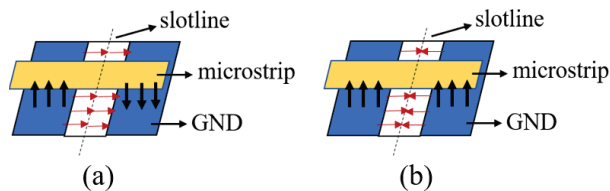


Fig. 3. Electric field distributions of the microstrip-slotline transition with (a) odd-mode excitation and (b) even-mode excitation.

as shown in Fig. 3 (b). A virtual magnetic wall is produced at the center of the slotline, and the vertical electric fields generated by the even-mode signals are canceled by each other on the slotline. Thus, there is nearly no vertical electric field passing through the slot, indicating that the even-mode signals are difficult to pass through the microstrip-slotline transition. It is concluded that the microstrip-slotline transition has good properties of odd-mode transmission and even-mode suppression.

To investigate the mechanism of the odd-mode transmission, the arms of the bent dipole are excited by odd-mode signals (Port-1), and Port-2 feeds the  $\Gamma$ -shaped microstrip-slotline transition, as shown in Fig. 4 (a). Figure 4 (b) shows the simulated reflection coefficients ( $S_{11}$ ), and coupling ( $S_{21}$ ) of the antenna as the length of the slotline ( $l_{s1}$ ) varies. When the length of the slotline is around a quarter wavelength, the odd-mode transmission coefficient of  $S_{12}$  will reach its maximum. Thus, the odd-mode transmission is optimal at this point. To investigate the principle of even-mode suppression, the ends of the loop antenna are excited by even-mode signals (Port-1), and the  $\Gamma$ -shaped microstrip-slotline transition is fed through Port-2, as illustrated in Fig. 5 (a). Figure 5 (b) shows the simulated reflection coefficients ( $S_{11}$ ) and coupling ( $S_{21}$ ) of the antenna with varying  $l_{s1}$ . When the slotline’s length is about a quarter wavelength, the curve of even-mode transmission coefficient  $S_{12}$  will produce a notch. Thus, the optimal even-mode suppression is achieved at this point. Moreover, the microstrip-slotline transition affects the reflection

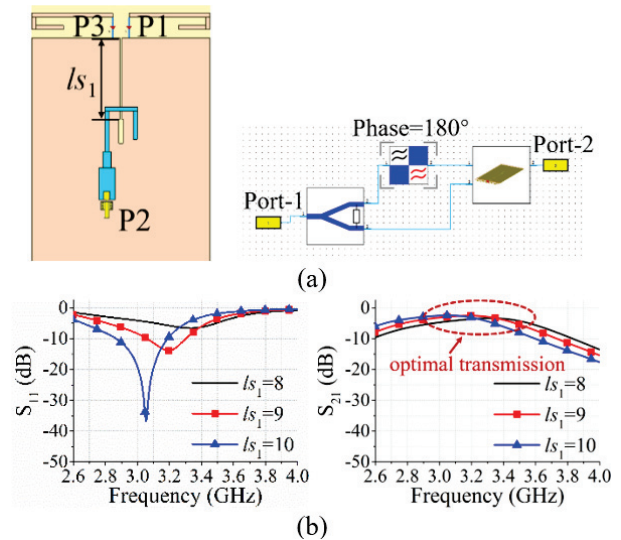


Fig. 4. Investigation of odd-mode transmission. (a) Odd-mode excitation for the dipole antenna. (b) Simulated reflection coefficients ( $S_{11}$ ) and coupling ( $S_{21}$ ) with varied  $l_{s1}$ . (Unit: mm).

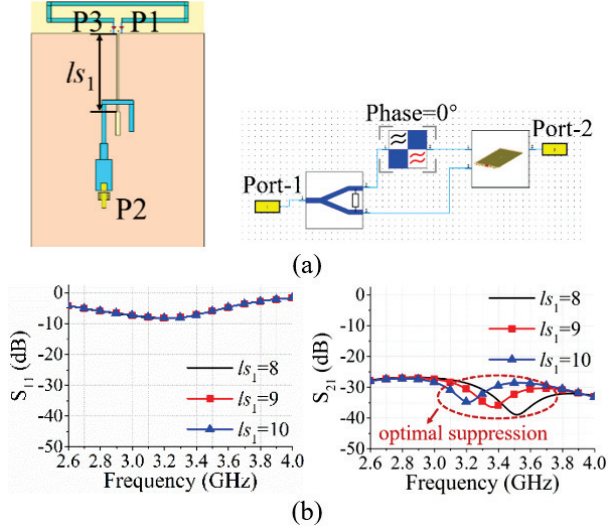


Fig. 5. Investigation of even-mode suppression. (a) Even-mode excitation for the loop antenna. (b) Simulated reflection coefficients ( $S_{11}$ ) and coupling ( $S_{21}$ ) with varied  $l_{s1}$ . (Unit: mm).

coefficient of the odd-mode excited antenna while not affecting the matching performance of the even-mode excited antenna.

Therefore, when the tightly arranged elements of the full-duplex antenna are excited by even-mode and odd-mode signals, respectively, the microstrip-slotline transition can be employed to achieve optimal odd-mode transmission and even-mode suppression. This results in a bandpass filtering characteristic for odd-mode excitation and a bandstop filtering characteristic for even-mode excitation, further improving the port isolation, which is different from the traditional decoupling methods based on mode cancellation method (MCM) [26, 29, 30].

### III. DESIGN PROCEDURE AND RESULTS DISCUSSION

#### A. Design procedure

To obtain high isolation and good impedance matching, the design parameters of the  $\Gamma$ -shaped microstrip-slotline transition of the proposed full-duplex antenna are studied. The stepped slotline helps to miniaturize the size, and the stepped microstrip feeding line contributes to impedance matching. Figure 6 shows the simulated reflection coefficient ( $S_{22}$ ) of the dipole and coupling ( $S_{21}$ ) of the antenna with varied  $l_{s1}$  and  $w_{s1}$ . Since the matching performance of the loop-type antenna is not affected by the  $\Gamma$ -shaped microstrip-slotline transition, the simulated reflection coefficients ( $S_{11}$ ) of the loop antenna are omitted here for clarity. As observed, the resonant frequency of the dipole-

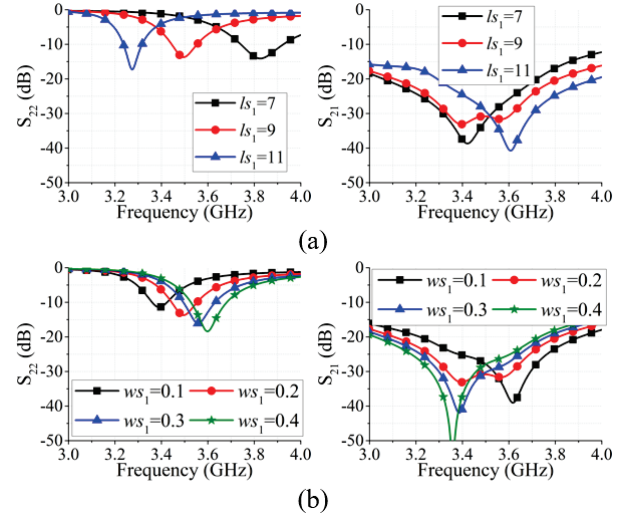


Fig. 6. Simulated reflection coefficient ( $S_{22}$ ) and coupling ( $S_{21}$ ) of the antenna with (a) varied  $l_{s1}$  and (b) varied  $w_{s1}$ . (Units: mm).

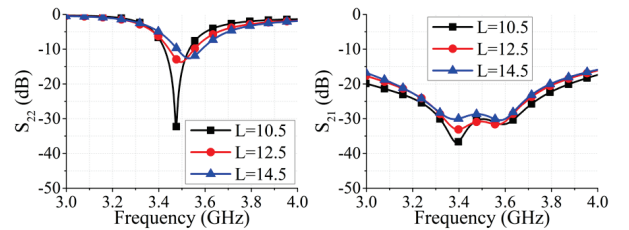


Fig. 7. Simulated reflection coefficient ( $S_{22}$ ) and coupling ( $S_{21}$ ) of the antenna with varied  $L$ . (Unit: mm).

type antenna decreases by increasing  $l_{s1}$  and decreasing  $w_{s1}$ , and the port isolation also changes accordingly. When the slotline's length is about a quarter wavelength, good impedance matching, and high isolation can be achieved. The impedance of the microstrip line is mainly determined by its width, and the length of the  $\Gamma$ -shaped microstrip line ( $L = lf_1 + df_1 + lf_2$ ) is studied in Fig. 7. It can be seen that the length of the  $\Gamma$ -shaped microstrip line mainly affects the impedance bandwidth, but has little effect on the resonant frequency of the dipole and the port isolation of the antenna. According to the parametric studies,  $L = 12.5$  mm (about a quarter wavelength) is selected to obtain a wider impedance bandwidth.

In conclusion, the matching performance (such as the resonant frequency and the impedance bandwidth) of the dipole antenna mainly depends on the sizes of the slotline and the microstrip line. The port isolation is determined by the even-mode suppression of the  $\Gamma$ -shaped microstrip-slotline transition, which mainly depends on the length and width of the slotline.

The optimized dimensions of the proposed full-duplex antenna are listed in the caption of Fig. 1.

**B. Results discussion**

Figure 8 shows the top and bottom views of the fabricated antenna. Two 50Ω coaxial cables are used to feed the two ports of the full-duplex antenna. The simulated and measured S-parameters of the antenna are shown in Fig. 9 (a). It can be seen that, across the desired frequency band of 3.4 to 3.6 GHz, the reflection coefficients

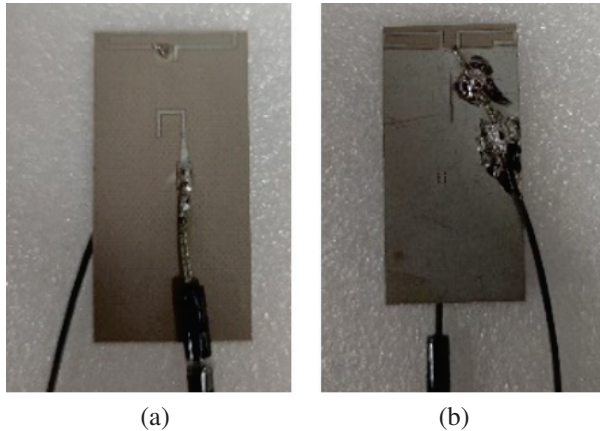
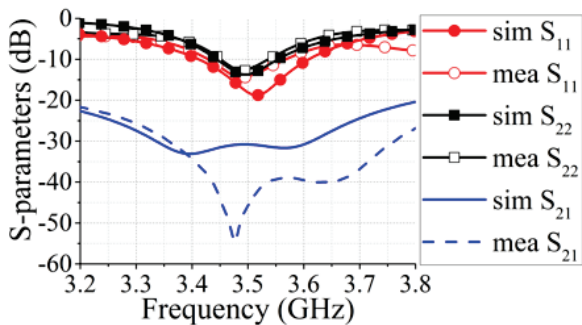
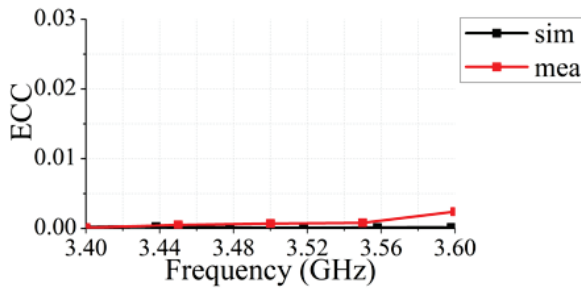


Fig. 8. Photographs of the prototype. (a) Top view. (b) Bottom view.



(a)



(b)

Fig. 9. Simulated and measured (a) S-parameters and (b) ECC of the antenna.

( $S_{11}$  and  $S_{22}$ ) of the loop (Antenna 1) and the dipole (Antenna 2) are maintained below -6 db, and the port isolation of the antenna is above 30 db over the entire good agreement. Figure 9 (b) illustrates the simulated and bandwidth. The simulation and measurement results are in measured envelope correlation coefficients (ECCs) from the simulated and measured radiation patterns [31]. The ECCs are less than 0.003 within the operating band, showing an excellent diversity performance. The normalized simulated and measured radiation patterns of Antenna 1 and Antenna 2 at the frequency of 3.5 GHz are shown in Fig. 10. The measured radiation patterns are consistent with the simulation results. In addition, the simulated and measured efficiencies at different frequencies are listed in Table 2. The simulation and measurement results are about the same, and the small discrepancies between them are mainly caused by manufacturing tolerance, imperfect soldering, and measurement errors. As observed, good efficiencies of 79% ~ 91% are achieved when fed through Port 1, and decent efficiencies of 64% ~ 83% are achieved when fed through Port 2, indicating satisfactory radiation performances of the proposed antenna.

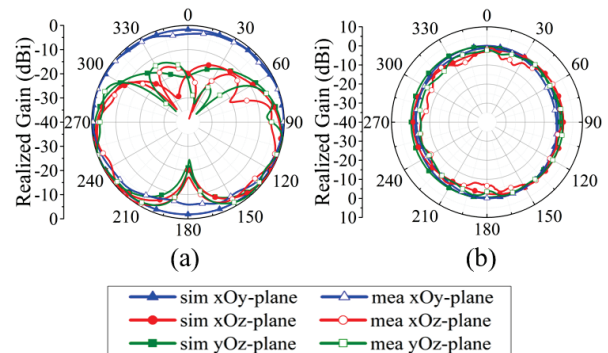


Fig. 10. Simulated and measured radiation patterns at 3.5 GHz of (a) Antenna 1 and (b) Antenna 2.

Table 2: Measured and simulated efficiencies of the antenna at different frequencies

Freq. (GHz)	3.40	3.45	3.50	3.55	3.60
Sim. Effi. (P1)	85%	92%	95%	91%	88%
Mea. Effi. (P1)	80%	87%	91%	85%	79%
Sim. Effi. (P2)	70%	82%	87%	84%	75%
Mea. Effi. (P2)	64%	80%	83%	81%	69%

#### IV. CONCLUSION

This article presents a full-duplex dongle antenna composed of a tightly arranged loop antenna and dipole antenna. High port isolation has been obtained thanks to the orthogonal modes of the elements and the even-mode suppression of the microstrip-slotline transition. The working mechanism and the design procedure of the  $\Gamma$ -shaped microstrip-slotline transition were well studied. The proposed antenna has been manufactured for experimental verification. The simulation and measurement results were in reasonable agreement. High isolation ( $>30$  db), low ECC ( $<0.003$ ), and high efficiency ( $>79\%/64\%$ ) were observed over the desired 5G frequency band from 3.4 to 3.6 GHz. Therefore, the proposed full-duplex dongle antenna with high isolation and compact size is suitable for B5G communications.

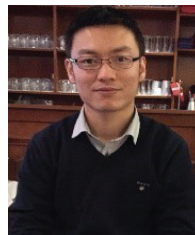
#### REFERENCES

- [1] A. Zaidi, F. Athley, J. Medbo, U. Gustavsson, and G. Durisi, *5G Physical Layer: Principles, Models and Technology Components*, Academic Press, London, U.K., 2018.
- [2] R. Hussain and M. S. Sharawi, "5G MIMO antenna designs for base station and user equipment: some recent developments and trends," *IEEE Antennas Propag. Mag.*, vol. 64, no. 3, pp. 95-107, Jun. 2022.
- [3] A. Sabharwal, P. Schniter, D. Guo, D. W. Bliss, S. Rangarajan, and R. Wichman, "In-band full-duplex wireless: Challenges and opportunities," *IEEE J. Sel. Areas Commun.*, vol. 32, no. 9, pp. 1637-1652, Sep. 2014.
- [4] D. Kim, H. Lee, and D. Hong, "A survey of in-band full-duplex transmission: From the perspective of PHY and MAC layers," *IEEE Commun. Surveys Tuts.*, vol. 17, no. 4, pp. 2017-2046, 4th Quart., 2015.
- [5] S. B. Venkatakrisnan, A. Hovsepian, A. D. Johnson, T. Nakatani, E. A. Alwan, and J. L. Volakis, "Techniques for achieving high isolation in RF domain for simultaneous transmit and receive," *IEEE Open J. Antennas Propag.*, vol. 1, pp. 358-367, Jul. 2020.
- [6] J. H. Zhang, F. M. He, W. Li, and Y. Li, "Self-interference cancellation: A comprehensive review from circuits and fields perspectives," *Electron.*, vol. 11, no. 2, pp. 172, Jan. 2022.
- [7] F. Peng, F. Peng, F. Yang, B. Liu, and X. Chen, "Experimental investigation of decoupling effect on the nonlinearity of power amplifiers in transmitter array," *Applied Computational Electromagnetics Society (ACES) Journal*, in press.
- [8] L. Zhao, Y. He, G. Zhao, X. Chen, G. L. Huang, and W. Lin, "Scanning angle extension of a millimeter wave antenna array using electromagnetic band gap ground," *IEEE Trans. Antennas Propag.*, vol. 70, no. 8, pp. 7264-7269, Aug. 2022.
- [9] X. Yang, Y. Liu, Y. X. Xu, and S. X. Gong, "Isolation enhancement in patch antenna array with fractal UC-EBG structure and cross slot," *IEEE Antennas Wireless Propag. Lett.*, vol. 16, pp. 2175-2178, May 2017.
- [10] M. Li, X. Chen, A. Zhang, W. Fan, and A. A. Kishk, "Split-ring resonator-loaded baffles for decoupling of dual-polarized base station array," *IEEE Antennas Wireless Propag. Lett.*, vol. 19, no. 10, pp. 1828-1832, Oct. 2020.
- [11] F. Faraz, X. Chen, Q. Li, J. Tang, J. Li, T. A. Khan, and X. Zhang, "Mutual coupling reduction of dual polarized low profile MIMO antenna using decoupling resonators," *Applied Computational Electromagnetics Society (ACES) Journal*, vol. 35, no. 1, pp. 38-43, Jan. 2020.
- [12] K. Wei, J. Li, L. Wang, Z. Xing, and R. Xu, "Mutual coupling reduction by novel fractal defected ground structure bandgap filter," *IEEE Trans. Antennas Propag.*, vol. 64, no. 10, pp. 4328-4335, Oct. 2016.
- [13] B. Qian, X. Chen, and A. A. Kishk, "Decoupling of microstrip antennas with defected ground structure using the common/differential mode theory," *IEEE Antennas Wireless Propag. Lett.*, vol. 20, no. 5, pp. 828-832, May 2021.
- [14] K. Wu, C. Wei, X. Mei, and Z. Zhang, "Array-antenna decoupling surface," *IEEE Trans. Antennas Propag.*, vol. 65, no. 12, pp. 6728-6738, Dec. 2017.
- [15] S. Zhang, X. Chen, and G. F. Pedersen, "Mutual coupling suppression with decoupling ground for massive MIMO antenna arrays," *IEEE Trans. Veh. Technol.*, vol. 68, no. 8, pp. 7273-7282, Aug. 2019.
- [16] S. Song, X. Chen, Y. Da, and A. Kishk, "Broadband dielectric resonator antenna array with enhancement of isolation and front-to-back ratio for MIMO application," *IEEE Antennas Wireless Propag. Lett.*, vol. 21, no. 7, pp. 1487-1491, Jul. 2022.
- [17] S. Song, Y. Da, B. Qian, S. Song, Y. Da, B. Qian, X. Huang, X. Chen, Y. Li, and A. A. Kishk, "Dielectric resonator magnetoelectric dipole arrays with low cross polarization, backward radiation, and mutual coupling for MIMO base station applications," *China Communications*, in press.
- [18] Y. Da, Z. Zhang, X. Chen, and A. A. Kishk, "Mutual coupling reduction with dielectric superstrate for base station arrays," *IEEE Antennas Wireless Propag. Lett.*, vol. 20, no. 5, pp. 843-847, May 2021.

- [19] Y. Da, X. Chen, and A. A. Kishk, "In-band mutual coupling suppression in dual-band shared-aperture base station arrays using dielectric block loading," *IEEE Trans. Antenna Propag.*, in press.
- [20] Y. M. Zhang and S. Zhang, "A novel aperture-loaded decoupling concept for patch antenna arrays," *IEEE Trans. Microw. Theory Techn.*, vol. 69, no. 9, pp. 4272-4283, Sept. 2021.
- [21] T. Dong, Y. Yu, M. Li, and H. Zeng, "Compact Antenna Array with Newly Designed Decoupling Network," *Applied Computational Electromagnetics Society (ACES) Journal*, vol. 33, no. 11, pp. 1196-1200, Nov. 2018.
- [22] B. Liu, Y. Da, X. Chen, and A. A. Kishk, "Hybrid decoupling structure based on neutralization and partition schemes for compact large-scale base station arrays," *IEEE Antennas Wireless Propag. Lett.*, vol. 21, no. 2, pp. 267-271, Feb. 2022.
- [23] Z. Ren, A. Zhao, and S. Wu, "MIMO antenna with compact decoupled antenna pairs for 5G mobile terminals," *IEEE Antennas Wireless Propag. Lett.*, vol. 18, no. 7, pp. 1367-1371, Jul. 2019.
- [24] L. Sun, H. Feng, Y. Li, and Z. Zhang, "Tightly arranged orthogonal mode antenna for 5G MIMO mobile terminal," *Microw. Opt. Technol. Lett.*, vol. 60, no. 7, pp. 1751-1756, Jul. 2018.
- [25] L. Sun, H. Feng, Y. Li, and Z. Zhang, "Compact 5G MIMO mobile phone antennas with tightly arranged orthogonal-mode pairs," *IEEE Trans. Antenna Propag.*, vol. 66, no. 11, pp. 6364-6369, Nov. 2018.
- [26] A. Zhang, K. Wei, Y. Hu, and Q. Guan, "High-isolated coupling-grounded patch antenna pair with shared radiator for the application of 5G mobile terminals," *IEEE Trans. Antennas Propag.*, in press.
- [27] F. Wei, X. B. Zhao, and X. W. Shi, "A balanced filtering quasi-Yagi antenna with low cross-polarization levels and high common-mode suppression," *IEEE Access*, vol. 7, pp. 100113-100119, Jul. 2019.
- [28] F. Wei, Z. J. Yang, P. Y. Qin, Y. J. Guo, B. Li, and X. W. Shi, "A balanced-to-balanced in-phase filtering power divider with high selectivity and isolation," *IEEE Trans. Microw. Theory Techn.*, vol. 67, no. 2, pp. 683-694, Feb. 2019.
- [29] L. Sun, Y. Li, Z. Zhang, and H. Wang, "Antenna decoupling by common and differential modes cancellation," *IEEE Trans. Antennas Propag.*, vol. 69, no. 2, pp. 672-682, Feb. 2021.
- [30] L. Sun, Y. Li, and Z. Zhang, "Decoupling between extremely closely spaced patch antennas by mode cancellation method," *IEEE Trans. Antennas Propag.*, vol. 69, no. 6, pp. 3074-3083, Jun. 2021.
- [31] X. Chen, P.-S. Kildal, J. Carlsson, and J. Yang, "MRC diversity and MIMO capacity evaluations of multi-port antennas using reverberation chamber and anechoic chamber," *IEEE Trans. Antennas Propag.*, vol. 61, no. 2, pp. 917-926, Feb. 2013.



**Yiran Da** received her B.S. degree in information engineering from Xi'an Jiaotong University, Xi'an, China, in 2020, where she is currently pursuing an M.S. degree. Her research interests include base station antenna design and mutual coupling reduction.



**Xiaoming Chen** (M'16-SM'19) received his B.Sc. degree in Electrical Engineering from Northwestern Polytechnical University, Xi'an, China, in 2006, and M.Sc. and PhD degrees in electrical engineering from Chalmers University of Technology, Gothenburg, Sweden, in 2007 and 2012, respectively. From 2013 to 2014, he was a postdoctoral researcher at the same university. From 2014 to 2017, he was with Qamcom Research & Technology AB, Gothenburg, Sweden. Since 2017, he has been a professor at Xi'an Jiaotong University, Xi'an, China. His research areas include MIMO antennas, over-the-air testing, reverberation chambers, and hardware impairments and mitigation. Prof. Chen serves as a Senior Associate Editor (AE) for *IEEE Antennas and Wireless Propagation Letters* and received the Outstanding AE Awards in 2018, 2019, 2020, and 2021. He received the URSI (International Union of Radio Science) Young Scientist Award in 2017 and 2018.



**Aofang Zhang** received his B.S. degree in Electromagnetic Wave Propagation and Antenna, and his Ph.D. degree in Electromagnetic Field and Microwave Technology from Xidian University, Xi'an, China, in 2014 and 2019, respectively. From 2019 to 2020, he was with the Consumer Business Group, Huawei Technologies Company Ltd., Xi'an. In 2021, he joined Honor Device Company Ltd., Xi'an, where he is currently a Senior Expert for the antenna design of smartphones, tablets, laptops, and routers. His current interests include antenna decoupling, multiband antennas, small size antennas, and MIMO antennas.



**Kunpeng Wei** received his B.S. degree in Electronic and Information Engineering from the Huazhong University of Science and Technology, Wuhan, China, in 2008, and his Ph.D. degree in electrical engineering from Tsinghua University, Beijing, China, in 2013. From July 2013 to December 2015, he was employed at the Radar Research Institute of the Chinese Air Force Research Laboratory, Beijing, conducting research in the areas of phased-array antenna design and radar system design. He joined the Consumer Business Group, Huawei Inc., Beijing, in 2016, where he was an Antenna Specialist and the Director of the Xi'an Antenna Team for five years. Since 2021, he has been with Honor Device Company Ltd., Beijing when this company split from Huawei; he is currently the Director of the Honor Antenna Team. He is also the leader of a large group of antenna engineers and is responsible for the research and development of antenna technologies to guarantee the market success of all Honor's mobile terminal products including smartphones, laptops, tablets, smartwatches, routers, smart screens, and earphones. He has authored over 50 refereed articles on consumer electronics antenna design. He holds over 15 granted U.S./Europe (EU)/Japan (JP)/China (CN) patents and has more than 30 patent applications pending. His current research interests include smartphone antenna design, small size 5G antenna systems in terminal devices, and millimeter-wave antenna array. Dr. Wei was a recipient of the Principal Scholarship of Tsinghua University in 2012, the Huawei Individual Gold Medal Award in 2018, the Huawei Team Gold Medal Award in 2017, and the Honor Team Gold Medal Award in 2021. He has been serving as an Associate Editor for *IET Electronics Letters* since October 2021.



**Ahmed A. Kishk** obtained his Ph.D. degrees in 1986 from the University of Manitoba, Canada. In 1986, he joined the University of Mississippi, first as an Assistant Professor and then as a Professor. Since 2011, he has been a Professor at Concordia University, Canada, as Tier 1 Canada Research Chair in Advanced Antenna Systems. He is a distinguished lecturer for the Antennas and Propagation Society (2013-2015). He was an Editor of *Antennas & Propagation Magazine* (1993-2014). He was an Editor-in-Chief of the *ACES Journal* from 1998 to 2001. He was a Guest Editor of the special issue on artificial magnetic conductors, soft/hard surfaces, and other complex surfaces, in *IEEE Transactions on Antennas and*

*Propagation*, 2005. He was the 2017 AP-S president. His research interests include millimeter wave antennas, beamforming network, dielectric resonator antennas, microstrip antennas, EBG, etc. He has published over 340-refereed journal articles and 450 conference papers. He is a co-author of four books, several book chapters, and the editor of three books. Prof. Kishk won the 1995 and 2006 outstanding paper awards for the *Applied Computational Electromagnetic Society Journal*. He received the 1997 Outstanding Engineering Educator Award from the Memphis section of the IEEE. He won the Outstanding Engineering Faculty Member of the Year in 1998 and 2009, and the Faculty Award for outstanding performance in research in 2001 and 2005. He received the Award of Distinguished Technical Communication for the entry of *IEEE Antennas and Propagation Magazine*, 2001. He also received The Valued Contribution Award for outstanding Invited Presentation from the Applied Computational Electromagnetic Society. He received the Microwave Theory and Techniques Society, Microwave Prize 2004 and 2013 Chen-To Tai Distinguished Educator Award from the IEEE Antennas and Propagation Society. He has been a Fellow of IEEE since 1998, Fellow of the Electromagnetic Academy, and a Fellow of the Applied Computational Electromagnetics Society (ACES).

# Wideband Single-Fed Circularly Polarized Stacked Patch Antenna With L-Shaped Stub

Wen Li<sup>1</sup>, Wei Xue<sup>1</sup>, Yingsong Li<sup>2</sup>, Xiang Xiong<sup>1</sup>, Kwok L. Chung<sup>3</sup>, and Zhixiang Huang<sup>2</sup>

<sup>1</sup>College of Information and Communication Engineering  
Harbin Engineering University, Harbin, 150001, China

<sup>2</sup>The Key Laboratory of Intelligent Computing and Signal Processing, Ministry of Education  
Anhui University, Hefei, Anhui, 230000, China  
liyingsong@ieee.org

<sup>3</sup>School of Computing Science and Engineering  
Huizhou University, Huizhou, 516007, China

**Abstract** – A wideband single-fed circularly polarized (CP) stacked patch antenna with an L-shaped stub is presented. The CP antenna is made up of the bottom gradient microstrip transmission line, middle driven patch and top square radiation patch. The driven patch with an L-shaped stub and opening slot can achieve a wideband CP radiation which is different from a conventional patch. The presented CP stacked patch antenna maintains good directional radiation, while featuring wideband CP radiation. The final tested results indicate that the presented CP antenna has significant performance with a  $-10$ -dB impedance bandwidth of 42.1% (4.26-6.53 GHz), a 3-dB AR bandwidth of 26.0% (4.36-5.66 GHz) and broadside peak gain of 8.6 dBic. Moreover, the fifth-generation (5G) N79 band (4.4-5.0 GHz) and 5G wireless local area network (WLAN) band (5.15-5.35 GHz) can be covered by the operating bandwidth of the presented CP antenna.

**Index Terms** – circularly polarized (CP), L-shaped stub, patch antenna, wideband antenna.

## I. INTRODUCTION

Circularly polarized (CP) stacked patch antenna have urgent application in modern wireless communication systems [1–3]. CP patch antennas, which are characterized by their compactness, ease of fabrication and resistance to multipath fading, have become the common schemes [4]. But the single-layer CP patch antenna has a high Q factor, which cannot meet the requirements of broadband. So, the study of the wideband CP patch antenna is an important topic.

Using parasitic patches in CP patch antenna is promising and is a common method to expand the axial ratio (AR) bandwidth [5–7]. In [5], the CP patch an-

tenna with capacitively coupled feed and rotated four parasitic strips achieve a wide AR bandwidth. In [6], the antenna composed of eight parasitic patches and feeding loop, which are placed on the same plane, is presented to yield a wide AR bandwidth. Compared with complete ground plane in [6], the ground plane with four crown slots in [7] is utilized to further expand AR bandwidth. Using stacked patches on radiation patches can also widen the AR bandwidth [8–13]. There are different shaped stacked patches, such as notched circular patch [8], hexagonal microstrip patch [9] and square patch [10], which realize 3-dB AR bandwidth of 10%, 13% and 11%. In [11], this CP antenna is fed by a corner-truncated ring, which can simplify the feeder structure. The CP patch antenna in [12] contains a stacked patch with pin-load, which can realize high gain. In addition to the above methods, many single-fed broadband CP antennas have recently been proposed [14–23]. In [14, 15], the L-shaped probe is employed to couple the patch and realize wide AR bandwidth. The near-field resonant parasitic CP patch antenna for radio frequency identification (RFID) reader applications yields an AR bandwidth of 9% [16]. In [17], three-dimensional split-ring resonators are used to achieve compact wideband CP antenna for fifth-generation (5G) new radio applications.

Multi-fed is command method to expand the AR bandwidth [24–33]. In [24], the single circular patch excited by dual capacitively coupled feeds with  $90^\circ$  phase shift features a wide AR bandwidth of 35%. This CP antenna array in [25], which has three centrosymmetric  $120^\circ$  phase shift feeds, can realize broadband CP radiation. A novel CP antenna consisting of four probes and parasitic patches is designed for the global positioning system [26]. Typically, four-port feed CP antenna array consists of four sequential rotation antenna elements

and four-port power divider, which provide the phases of  $0^\circ$ ,  $90^\circ$ ,  $180^\circ$ ,  $270^\circ$ . In [27], a wideband Wang-shaped CP patch antenna array, which has unidirectional radiation, is introduced and final measured results show AR bandwidth. As mentioned above, multi-feed antenna array can realize the advantages of high gain while maintaining wideband AR bandwidth and unidirectional radiation, but the antenna array requires complicated feed network, which reduces the final efficiency [34].

In this article, a wideband CP stacked patch antenna is introduced. For achieving the circular polarization, the opening slot and L-shaped stub are adopted to the conventional stacked patch antenna. In the final design, the proposed CP antenna has good directional radiation with front-to-back ratio of 23.48 dB at 5 GHz, while featuring wide AR bandwidth. The final tested results indicate that the final CP antenna has significant performances with a  $-10$ -dB impedance bandwidth of 42.1% (4.26-6.53 GHz), a 3-dB AR bandwidth of 26.0% (4.36-5.66 GHz) and peak broadside gain of 8.6 dBic. Moreover, the measured AR bandwidth, which achieved good agreement with simulation results, can cover 4.4-5.0 GHz of the 5G N79 band and 5.15-5.35 GHz band of 5G WLAN at the same time, which can be utilized for different applications.

## II. ANTENNA DESIGN AND PERFORMANCE

### A. Antenna geometry

As shown in Fig. 1, four-layer dielectric substrates are adopted to fabricate the proposed wideband single-fed CP patch antenna. Three different substrates are adopted, in which Layer\_1 and Layer\_3 have a dielectric permittivity  $\epsilon_r$  3, a loss tan  $\delta$  of 0.0027, and a thickness  $h1$  of 1 mm, Layer\_2 for the driven patch has a dielectric permittivity  $\epsilon_r$  of 3.5, a loss tan  $\delta$  of 0.0027, and a thickness  $h3$  of 1.5 mm, Layer\_4 for the ground plane and feeding line has a dielectric permittivity  $\epsilon_r$  of 4.4, a loss tan  $\delta$  of 0.025 and a thickness  $h4$  of 0.8 mm. Figure 1 (a) shows the radiation patch on the top of Layer\_1. The driven patch consists of rectangular patch with opening slot and L-shaped stub on the Layer\_2, which provides the CP mode. Figure 1 (b) shows the air gap between Layer\_1 and Layer\_2 with a thickness of 4 mm. The gradient feeding line, which provides the good impedance matching, is fabricated on the bottom of Layer\_4. This antenna was optimized by CST microwave software. The optimized antenna parameters are:  $L_g = 60$ ,  $W1 = 17$ ,  $W2 = 17$ ,  $W3 = 0.2$ ,  $W4 = 2.0$ ,  $Slotw = 6$ ,  $Cpw = 7$ ,  $d = 1.2$ ,  $r = 1$ ,  $L1 = 3$ ,  $G1 = 6$ ,  $G2 = 3$ ,  $s = 1$ ,  $W5 = 3$ ,  $W6 = 1.5$ ,  $L2 = 8$ ,  $L3 = 8$ . Unit: mm.

### B. Design process

With reference to Fig. 2, three prototypes are given for exploring the mechanism of wideband CP, which

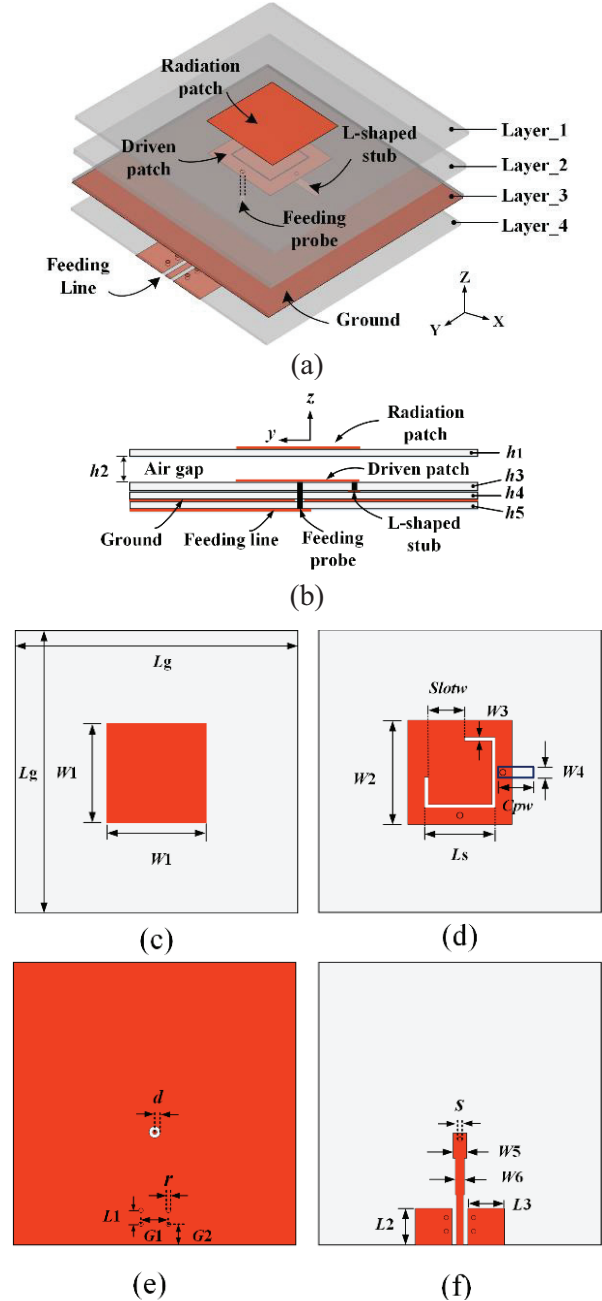


Fig. 1. Structure of the presented CP antenna. (a) three-dimensional view. (b) Side view. (c) Top view of Layer\_1. (d) Top view of Layer\_2. (e) Top view of Layer\_4. (f) Bottom view of Layer\_4.

have the same radiation patch. Ant. 1 is the conventional stacked patch antenna, which enables wide impedance bandwidth and high gain. Some researchers have proposed high-gain filtering antenna [35], ultra-wideband microstrip patch antenna [36] and wideband CP antenna [10] based on this stacked patch antenna. The L-shaped stub is employed to realize the circular polarization in

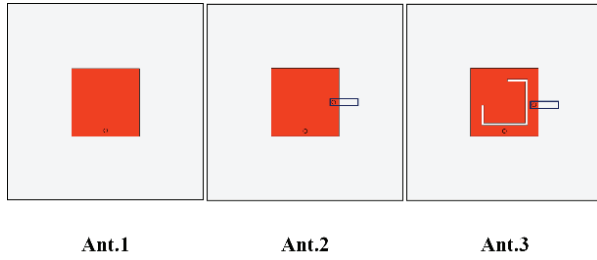


Fig. 2. Evolution of the presented antenna.

Ant. 2. The open slot is added to Ant. 3 when compared with Ant. 2. The same substrate type and height is used in all three antennas.

The driven patch is fed by a probe and has the same width of 17 mm as the radiation patch. With reference to Fig. 3, the Ant. 1 has two resonances near to 4.8 and 5.6 GHz and achieves linear polarization. For improving the CP performance, the L-shaped stub is utilized in Ant. 2. In Fig. 3, the resonance frequency at high frequency moves from 5.6 to 6 GHz, the AR of Ant. 2 is below 20 at 4 to 6 GHz and especially below 3 at 5.7 GHz. It is

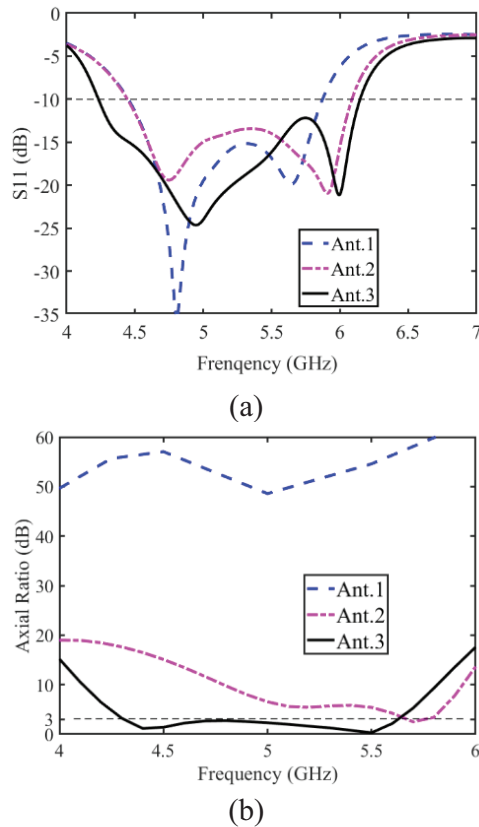


Fig. 3. Simulated results of the presented antenna in different antennas. (a) Reflection coefficient and (b) AR.

noteworthy that the CP radiation of the original stacked patch antenna is apparently improved because of the L-shaped stub structure, but the 3-dB AR bandwidth is narrow. As shown in Fig. 2, the opening slot, which can extend the AR bandwidth, is etched on the driven patch in Ant. 3. It is obvious that the AR of Ant. 3 decreases compared to Ant. 2. In Fig. 3, the Ant. 3 has a simulated 3-dB AR bandwidth of 27% (4.29–5.63 GHz) and –10-dB impedance bandwidth of 37% (4.23–6.15 GHz).

Figure 4 shows the simulated surface current contributions at 5 GHz, which can achieve the verification

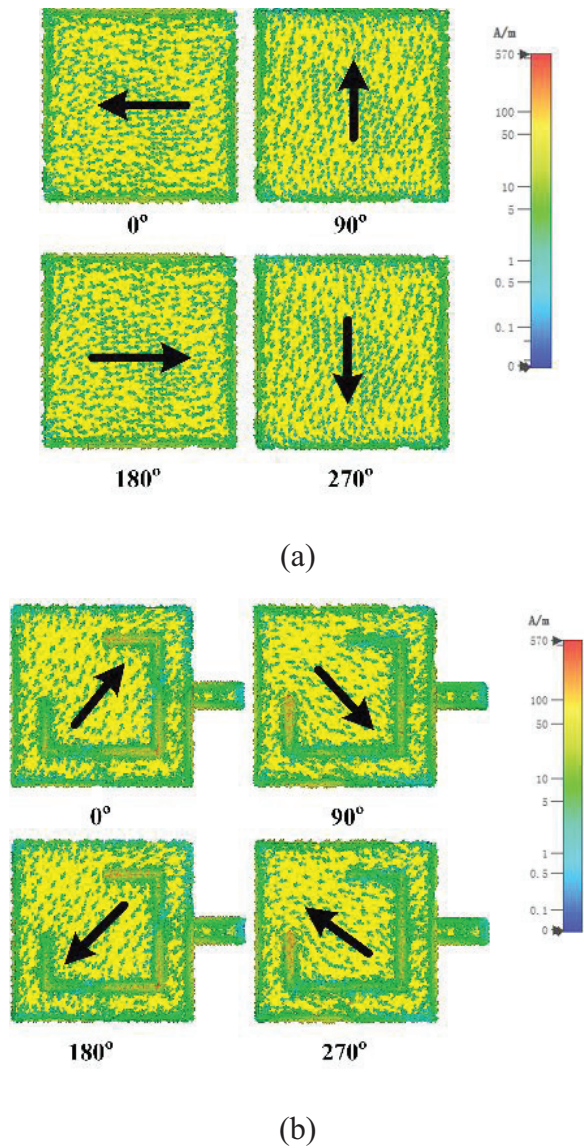


Fig. 4. Surface current distributions on the radiation patch and driven patch of the proposed antenna at 5 GHz in 0°, 90°, 180°, and 270° phase. (a) Radiation patch and (b) Driven patch.

of circularly polarized radiation. In Fig. 4, the surface current contributions of the square radiation patch and driven patch with L-shaped stub and opening slot are provided. In Fig. 4 (a), the current of the radiation patch flows in the direction of the black arrow at the phase of  $0^\circ$ , whereas the current rotates  $90^\circ$  in a clockwise direction at the phase of  $90^\circ$ . The direction of the surface current in the driven patch is different from the direction of the radiation because the radiation patch is fed by a driven patch coupling. It is found that the direction of surface current, which is represented by the black arrow, is clockwise with a phase change. The left-hand CP radiation is produced based on the direction of current rotation.

Parametric studies are implemented for determining the final dimensions. The proposed antenna performance including the reflection coefficient and AR is influenced by the numerous parameters. Here, two key parameters  $C_{pw}$  (the L-shaped stub length) and  $Slotw$  (the opening slot length) have been selected for study. Figure 5 demonstrates the effect of the L-shaped stub  $C_{pw}$  on the reflection coefficient and AR. Two resonant frequency

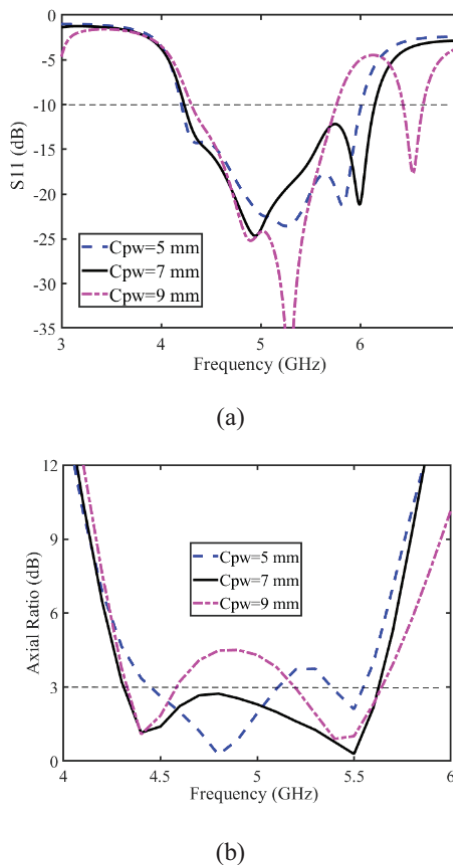


Fig. 5. Effect of the L-shaped stub length  $C_{pw}$  of driven patch on (a) reflection coefficient and (b) AR.

points are generated on the reflection coefficient curve and two minimum points in the AR curve. The high resonant frequency shifts to higher frequencies as  $C_{pw}$  increases, but when  $C_{pw}$  equals 9 mm the reflection coefficient of 5.46 to 5.92 GHz between the two resonance points is higher than  $-10$  dB in Fig. 5 (a). AR is significantly influenced by  $C_{pw}$  and a 3-dB AR bandwidth of 27% is exhibited, when  $C_{pw}$  equals 7 mm. Figure 6 demonstrates the influence of the opening slot length  $Slotw$  on reflection coefficient and AR. It is found that the resonance frequencies change significantly and the minimum value of AR decreases and then rises with  $Slotw$  increasing from 4 to 8 mm. So, a  $Slotw$  value of 6 mm is chosen as the final dimension.

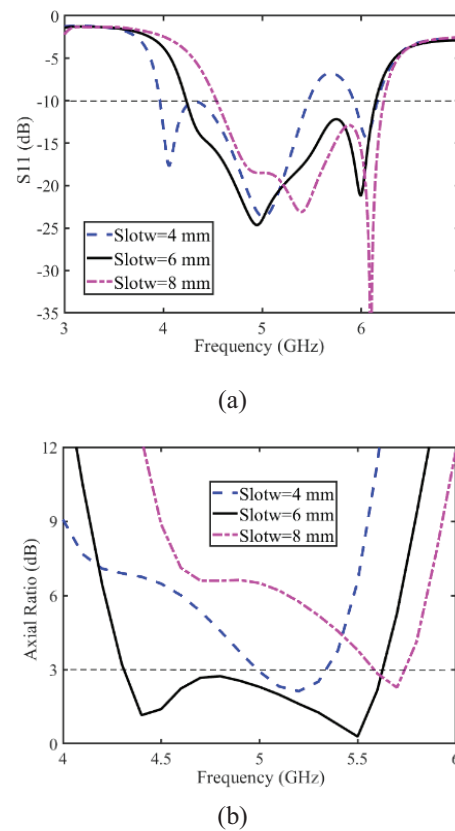


Fig. 6. Effect of the opening slot length  $Slotw$  of driven patch on (a) reflection coefficient and (b) AR.

### III. EXPERIMENTAL VERIFICATION

The prototype has been fabricated for achieving validation of the presented antenna. Agilent N5062A Network Analyzer was adopted to measure the reflection coefficient. With reference to Fig. 7, an anechoic chamber was utilized to test the radiation characteristics including the gains and ARs. Figure 8 demonstrates the simulated and measured results including reflection coefficient, AR, and gain. A  $-10$ -dB simulated impedance

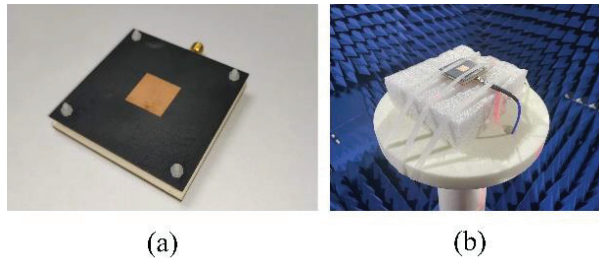
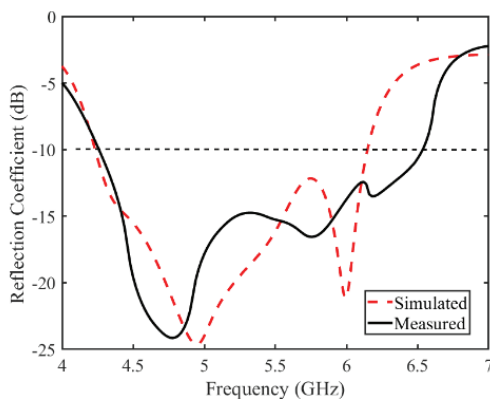
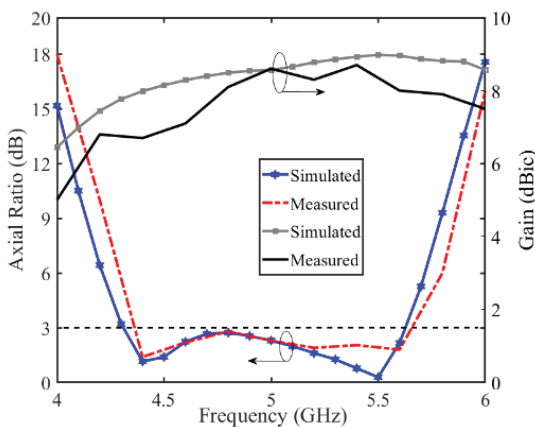


Fig. 7. (a) Photograph of the fabricated prototype. (b) Photograph of anechoic chamber testing.

bandwidth of 37.0% (4.23-6.15 GHz) is obtained, while the measured impedance bandwidth is 42.1% (4.26-6.53 GHz). A 3-dB simulated AR bandwidth is 26.0% covering 4.36 to 5.66 GHz. The measured broadside gain at 5 GHz is 8.6 dBic and the measured gain is a little lower than the simulated gain from 4 to 6 GHz. This is because substrate material suffers from instability in dielectric constant and loss.



(a)



(b)

Fig. 8. Simulated and measured results of the presented CP patch antenna. (a) Reflection coefficient. (b) AR and peak gain.

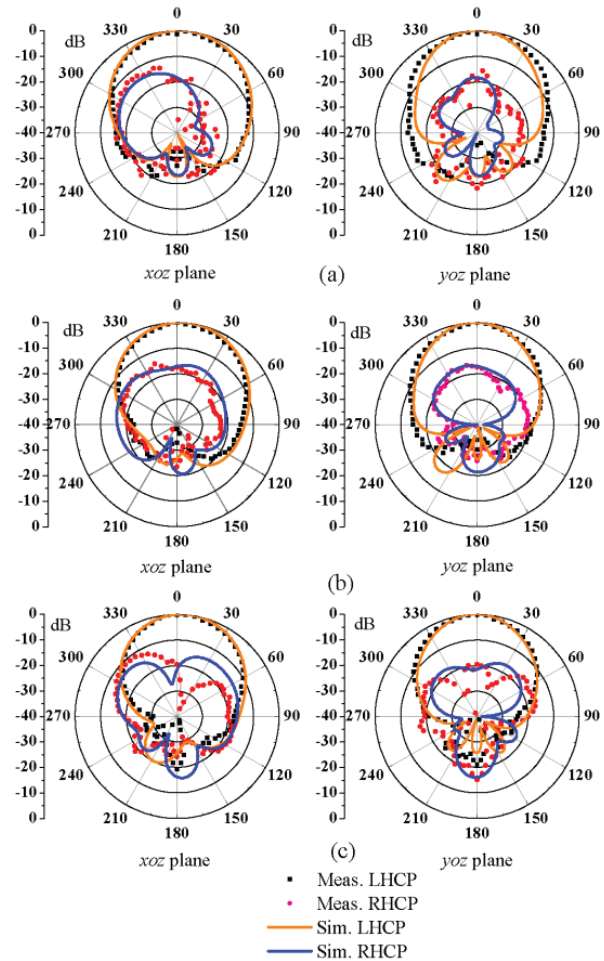


Fig. 9. Simulated and measured radiation patterns of the final tested antenna. (a) At 4.5 GHz, (b) at 5 GHz, (c) at 5.5 GHz.

Figure 9 demonstrates the normalized radiation patterns at the significant frequencies of 4.5, 5, and 5.5 GHz. The normalized left-hand CP has a value of 0 dB, which is clearly greater than the normalized right-hand CP in  $z$ -axis direction. The measured radiation patterns maintain a high degree of similarity to the simulated patterns. The proposed antenna records half-power beamwidths of  $53^\circ$  and  $52^\circ$  in the two principal planes, and a front-to-back ratio of 23.48 dB.

#### IV. PERFORMANCE COMPARISON

Table 1 illustrates a comparison of various parameters including numerous key parameters. The compact CP patch antenna in [6] with feeding loop produced a high gain of about 9.8 dBic, but have the narrow AR bandwidth of 12.9. Incomplete ground plane is utilized in [7] to expand the AR bandwidth but the radiation of this CP patch antenna is non-directional radiation. In

Table 1: Comparison to the performance of other CP antennas

References	Size ( $\lambda_0^3$ )	Freq (GHz)	-10-dB Impedance Bandwidth (%)	3-dB AR Bandwidth (%)	Peak Gain (dBic)
Ref. [6]	$0.92 \times 0.92 \times 0.028$	5.13~6.24	19.5	12.9	9.8
Ref. [7]	$1.02 \times 1.02 \times 0.028$	5.20~6.40	25.9	20.6	8.0
Ref. [8]	$1 \times 1 \times 0.15$	3.3~6.4	63.9	10.0	<8.0
Ref. [11]	$0.65 \times 0.65 \times 0.066$	3.6~6.0	20.6	6.9	7.0
Ref. [13]	$0.8 \times 0.8 \times 0.09$	2.08~2.62	22.9	17.9	8.5
Ref. [16]	$0.45 \times 0.45 \times 0.074$	0.83~0.96	32.4	9.0	7.3
Ref. [17]	$0.277 \times 0.277 \times 0.03$	3.3~3.8	14.1	14.2	5.1
Proposed design	$1 \times 1 \times 0.122$	4.26~6.53	42.1	26.0	8.6

[8, 11, 16] and [17], the peak gain of the antennas is lower than 8 dBic. The antenna in [13] with a horizontal L-shaped strip exhibits the peak gain of 8.5 dBic and a 3-dB AR bandwidth of 17.9%. The proposed CP stacked patch antenna with an L-shaped stub produces a wide operation bandwidth 26% (4.36-5.66 GHz) and a high broadside gain of 8.6 dBic.

## V. CONCLUSION

A wideband CP patch antenna with an L-shaped stub is presented. Based on conventional stacked antenna, the opening slot and L-shaped stub are added to expand the AR bandwidth. The effect of length of the L-shaped stub and the opening slot on the reflection coefficient and AR is studied. The final measured results exhibit a -10-dB impedance bandwidth of 42.1% (4.26-6.53 GHz), a 3-dB AR bandwidth of 26% (4.36-5.66 GHz) and a peak broadside gain of 8.6 dBic. This wideband CP patch antenna has significant directional radiation with front-to-back ratio of 23.48 dB at 5 GHz. Owing to the advantage of broadband CP radiation and high gain, the presented CP patch antennas have a wide range of 5G applications.

## REFERENCES

- [1] F. Zhu, Q. Luo, and S. Gao, *Circularly Polarized Antennas*, Wiley, New York, USA, 2013.
- [2] N. Yan, K. Ma, and Y. Luo, "An SISL sequentially rotated feeding circularly polarized stacked patch antenna array," *IEEE Transactions on Antennas and Propagation*, vol. 68, no. 3, pp. 2060-2067, 2020.
- [3] B. Feng, L. Li, K. L. Chung, and Y. Li, "Wideband widebeam dual circularly polarized magnetoelectric dipole antenna/array with meta-columns loading for 5G and beyond," *IEEE Transactions on Antennas and Propagation*, vol. 69, no. 1, pp. 219-228, 2021.
- [4] K. L. Wong, *Compact and Broadband Microstrip Antennas*, Wiley, New York, USA, 2002.
- [5] J. Wu, Y. Yin, Z. Wang, and R. Lian, "Broadband circularly polarized patch antenna with parasitic strips," *IEEE Antennas and Wireless Propagation Letters*, vol. 14, pp. 559-562, 2015.
- [6] K. Ding, C. Gao, D. Qu, and Q. Yin, "Compact broadband circularly polarized antenna with parasitic patches," *IEEE Transactions on Antennas and Propagation*, vol. 65, no. 9, pp. 4854-4857, 2017.
- [7] L. Wang, Z. Zhu, and Y. En, "Performance enhancement of broadband circularly polarized slot-microstrip antenna using parasitic elements," *IEEE Antennas and Wireless Propagation Letters*, vol. 20, no. 12, pp. 2255-2259, 2021.
- [8] Y. Guo and D. C. H. Tan, "Wideband single-feed circularly polarized patch antenna with conical radiation pattern," *IEEE Antennas and Wireless Propagation Letters*, vol. 8, pp. 924-926, 2009.
- [9] N. Nasimuddin, X. Qing, and Z. N. Chen, "A wideband circularly polarized stacked slotted microstrip patch antenna," *IEEE Antennas and Propagation Magazine*, vol. 55, no. 6, pp. 84-99, 2013.
- [10] T. Mondal, S. Samanta, R. Ghatak, and S. R. B. Chaudhuri, "A novel hexagonal wideband circularly polarized stacked patch microstrip antenna," *Microw. Opt. Technol. Lett.*, vol. 57, no. 11, pp. 2548-2554, 2015.
- [11] C. Deng, X. Lv, and Z. Feng, "Low-profile circularly polarised patch-ring antenna with compact feeding network," *IET Microwaves Antennas & Propagation*, vol. 12, no. 3, pp. 410-415, 2017.
- [12] Z.-X. Liu, L. Zhu, and X. Zhang, "A low-profile and high-gain CP patch antenna with improved AR bandwidth via perturbed ring resonator," *IEEE Antennas and Wireless Propagation Letters*, vol. 18, no. 2, pp. 397-401, 2019.

- [13] J. Wu, X. Ren, Z. Wang, and Y. Yin, "Broadband circularly polarized antenna with L-shaped strip feeding and shorting-pin loading," *IEEE Antennas and Wireless Propagation Letters*, vol. 13, pp. 1733-1736, 2014.
- [14] K. L. Chung, A. Cui, and B. Feng, "A Guo-shaped patch antenna for hidden WLAN access points," *International Journal of RF and Microwave Computer-Aided Engineering*, vol. 31, no. 2, 2021.
- [15] W. K. Lo, J. L. Hu, C. H. Chan, and K. M. Luk, "Circularly polarized patch antenna with an L-shaped probe fed by a microstrip line," *Microwave and Optical Technology Letters*, vol. 24, no. 6, pp. 412-414, 1999.
- [16] J. Li, H. Liu, S. Zhang, M. Luo, Y. Zhang, and S. He, "A wideband single-fed, circularly-polarized patch antenna with enhanced axial ratio bandwidth for UHF RFID reader applications," *IEEE Access*, vol. 6, pp. 55883-55892, 2018.
- [17] Z. Wang, Y. Dong, and T. Itoh, "Miniaturized wideband CP antenna based on metaresonator and CRLH-TLs for 5G new radio applications," *IEEE Transactions on Antennas and Propagation*, vol. 69, no. 1, pp. 74-83, 2021.
- [18] K. L. Chung, "A wideband circularly polarized H-shaped patch antenna," *IEEE Transactions on Antennas and Propagation*, vol. 58, no. 10, pp. 3379-3383, 2010.
- [19] H. L. Zhu, S. W. Cheung, K. L. Chung, and T. I. Yuk, "Linear-to-circular polarization conversion using metasurface," *IEEE Transactions on Antennas and Propagation*, vol. 61, no. 9, pp. 4615-4623, 2013.
- [20] K. L. Chung, S. Xie, Y. Li, R. Liu, S. Ji, and C. Zhang, "A circular-polarization reconfigurable Meng-shaped patch antenna," *IEEE Access*, vol. 6, pp. 51419-51428, 2018.
- [21] B. Feng, L. Li, K. L. Chung, and Y. Li, "Wideband widebeam dual circularly polarized magneto-electric dipole antenna/array with meta-columns loading for 5G and beyond," *IEEE Transactions on Antennas and Propagation*, vol. 69, no. 1, pp. 219-228, 2021.
- [22] Y. Li and R. Mittra, "A three-dimensional circularly polarized antenna with a low profile and a wide 3-dB beamwidth," *Journal of Electromagnetic Waves and Applications*, vol. 30, no. 1, pp. 89-97, 2016.
- [23] B. Qiu and Y. Li, "Gain-enhanced wideband circularly polarized antenna with a non-uniform metamaterial reflector," *Applied Computational Electromagnetics Society (ACES) Journal*, vol. 37, no. 3, pp. 281-286, 2022.
- [24] K.-L. Wong and T.-W. Chiou, "Broad-band single-patch circularly polarized microstrip antenna with dual capacitively coupled feeds," *IEEE Transactions on Antennas and Propagation*, vol. 49, no. 1, pp. 41-44, 2001.
- [25] C. Lin, F. Zhang, Y. Jiao, F. Zhang, and X. Xue, "A three-fed microstrip antenna for wideband circular polarization," *IEEE Antennas and Wireless Propagation Letters*, vol. 9, pp. 359-362, 2010.
- [26] S. Fu, Q. Kong, S. Fang, and Z. Wang, "Broadband circularly polarized microstrip antenna with coplanar parasitic ring slot patch for L-band satellite system application," *IEEE Antennas and Wireless Propagation Letters*, vol. 13, pp. 943-946, 2014.
- [27] K. L. Chung, Y. Li, and C. Zhang, "Broadband artistic antenna array composed of circularly-polarized Wang-shaped patch elements," *AEU-International Journal of Electronics and Communications*, vol. 74, pp. 116-122, 2017.
- [28] K. L. Chung, W. Li, Y. Li, R. Liu, and P. Zhang, "Chinese character-shaped artistic patch antenna," *IEEE Antennas and Wireless Propagation Letters*, vol. 18, no. 8, pp. 1542-1546, 2019.
- [29] K. L. Chung, X. Yan, A. Cui, and Y. Li, "Circularly-polarized linear antenna array of non-identical radiating patch elements for WiFi/WLAN applications," *AEU-International Journal of Electronics and Communications*, vol. 129, 2020.
- [30] K. L. Chung and A. S. Mohan, "A circularly polarized stacked electromagnetically coupled patch antenna," *IEEE Transactions on Antennas and Propagation*, vol. 52, no. 5, pp. 1365-1369, 2004.
- [31] K. L. Chung, "High-performance circularly polarized antenna array using metamaterial-line based feed network," *IEEE Transactions on Antennas and Propagation*, vol. 61, no. 12, pp. 6233-6237, 2013.
- [32] K. L. Chung and S. Kharkovsky, "Mutual coupling reduction and gain enhancement using angular offset elements in circularly polarized patch array," *IEEE Antennas and Wireless Propagation Letters*, vol. 12, pp. 1122-1124, 2013.
- [33] B. Liu, X. Chen, J. Tang, A. Zhang, and A. A. Kishk, "Co- and cross-polarization decoupling structure with polarization rotation property between linearly polarized dipole antennas with application to decoupling of circularly polarized antennas," *IEEE Transactions on Antennas and Propagation*, vol. 70, no. 1, pp. 702-707, 2022.
- [34] X. Chen, M. Zhao, H. Huang, Y. Wang, S. Zhu, C. Zhang, J. Yi, and A. Kishk, "Simultaneous decoupling and decorrelation scheme of MIMO arrays," *IEEE Transactions on Vehicular Technology*, vol. 71, no. 2, pp. 2164-2169, 2022.
- [35] X. Y. Zhang, W. Duan, and Y. Pan, "High-gain filtering patch antenna without extra circuit," *IEEE*

*Transactions on Antennas and Propagation*, vol. 63, no. 12, pp. 5883-5888, 2015.

- [36] M. A. Matin, B. S. Sharif, and C. C. Tsimenidis, "Dual layer stacked rectangular microstrip patch antenna for ultra wideband applications," *IET Microwaves, Antennas & Propagation*, vol. 1, no. 6, pp. 1192-1196, 2007.



**Wen Li** was born in Shandong, China. He received his M.S. degree in Qingdao University of Technology, Shandong, China, in 2020. He is currently pursuing a Ph.D. degree in Information and Communication Engineering at the Harbin Engineering University, China. His current research interests include circularly polarized antennas and MIMO antennas.



**Wei Xue** received his B.S. and M.S. degrees in Communication and Information Systems from Harbin Engineering University, Harbin, China, in 1995 and 2001, respectively. He received his Ph.D. degree from St. Petersburg State Polytechnical University, Russia, in 2007. He is currently a Professor with the Department of Information and Communication Engineering, Harbin Engineering University. His current research interests include underwater and underground current field communications, efficient spectrum modeling, and simulation.



**Yingsong Li** received his B.S. degree in Electrical and Information Engineering, and M.S. degree in Electromagnetic Field and Microwave Technology from Harbin Engineering University, 2006 and 2011, respectively. He received his Ph.D. degree from both Kochi University of Technology (KUT), Japan and Harbin Engineering University (HEU), China in 2014. Since March 2022 he has been a full Professor at the School of Electronic and Information Engineering at Anhui University. From 2014 to 2022 he was a full Professor at HEU and a visiting scholar at the University of California, Davis from March 2016 to March 2017, a visiting Professor at the University of York, UK in 2018, and a visiting Professor at the Far Eastern Federal University (FEFU) and KUT. Since 2018, he has held a visiting professorship at the School of Information of KUT. He is a Fel-

low of the Applied Computational Electromagnetics Society, and is also a senior member of the Chinese Institute of Electronics (CIE) and IEEE. He has authored and coauthored about 300 journal and conference papers in various areas of electrical and information engineering. His current research interests include signal processing, adaptive filters, metasurface designs and microwave antennas.

Dr. Li served as an Area Editor of *AEÜ-International Journal of Electronics and Communications* from 2017 to 2020, he is an Associate Editor of *IEEE Access*, the *Applied Computational Electromagnetics Society Journal (ACES) Journal*, the *Alexandria Engineering Journal* and *Electromagnetic Science*. He was the TPC Co-Chair of the 2019 IEEE International Workshop on Electromagnetics (iWEM 2019-2020), 2019 IEEE 2nd International Conference on Electronic Information and Communication Technology (ICEICT 2019), 2019 International Applied Computational Electromagnetics Society (ACES) Symposium-China, 2019 Cross Strait Quad-regional Radio Science and Wireless Technology Conference (2019 CSQRWC). He acts as a reviewer for numerous IEEE, IET, Elsevier and other international journals and conferences.



**Kwok L. Chung** (Ph.D., Senior Member, IEEE) was a research professor and a supervisor of Ph.D. students with Qingdao University of Technology (QUT) from Dec. 2005 to Jan. 2021. He was a Director of Civionics Research Laboratory at QUT, where he led a cross-disciplinary research team for structural health monitoring. In April 2021, he joined Huizhou University as a distinguished professor. He has authored and coauthored about 180 publications [science citation index (SCI) and engineering index (EI)] in various areas of electrical and civil engineering. His current research interests include passive wireless sensors, cement-based materials design and characterization, clothing antennas, and intelligent reconfigurable surfaces.

Prof. Chung has been classified as the world's top 2 % scientists in the 2020 and 2021 lists released by Stanford University. He is the Founding Chair of the IEEE Qingdao AP/MTT/COM joint chapter (CN10879) with Beijing Section. He has been an Associate Editor of IEEE ACCESS and an Associate Editor of ELSEVIER ALEXANDRIA ENGINEERING JOURNAL since 2016 and 2020, respectively. He is an active reviewer for numerous international journals from IEEE, Elsevier, IOP science, and many others.



**Zhixiang Huang** received his BS degree in Statistic and Probability and Ph.D. in Electromagnetic Field and Microwave Technology from Anhui University in 2002 and 2007, respectively. He is a Lecturer of Anhui University from 2007 to 2008 and is promoted to Professor in 2008, and is a visiting scholar in Ames Laboratory, Iowa State University, from 2010 to 2011. Currently, he is a full Professor and the dean of the School of Electronic Information Engineering of Anhui University, founder of Key Laboratory of Electromagnetic Environmental

Sensing of Anhui Higher Education Institutes, director of the Young Scientists Club of Chinese Institute of Electronics (CIE), member of the Youth Working Committee of CIE. He is the recipient of the Outstanding Young Talent Project of National Natural Science Foundation of China (NSFC) in 2018 and the Chang Jiang Scholars Program of Ministry of Education of the People's Republic of China in 2022. He is a Senior Member of IEEE. He has more than 100 academic papers in peer-reviewed international/national journals. His current interests include theoretical and computational in electromagnetics and Microwave/RF circuit design, and multi-physics modeling.

# A Circularly Polarized Patch Antenna Array with Reduced Mutual Coupling Using the Aperture-Loading Decoupling Technique

Xin Cheng, Bingyi Qian, Le Chang, Jinlin Liu, and Xiaoming Chen

School of Information and Communications Engineering  
Xi'an Jiaotong University, Xi'an, 710049, China  
changle@mail.xjtu.edu.cn

**Abstract** – An aperture-loaded decoupling strategy for  $1 \times 8$  circularly polarized (CP) patch antenna array is presented in this article. By introducing an additional coupling path, the mutual coupling between adjacent antennas is cancelled. The result shows that more than 20-dB isolation enhancement is obtained by applying this strategy at the center frequency of 3.38 GHz. Mutual coupling between both adjacent and non-adjacent elements are suppressed to less than -25 dB. Moreover, the impedance bandwidth and axial ratio (AR) is also improved with decoupling. Compared with conventional CP antenna decoupling methods, the proposed approach has the characteristics of low profile, compact size, and low impact for the ground plane. It is shown that the AR bandwidth can be enhanced using the proposed decoupling method.

**Index Terms** – array antenna, circular polarization, decoupling aperture, mutual coupling reduction.

## I. INTRODUCTION

In the past few years, attributed to the advantages of large system capacity and high spectral efficiency, 5G communication systems are universally applied in wireless communication systems. It is generally recognized that multiple-input multiple-output (MIMO) is a crucial technology for 5G wireless communications since it can significantly enhance channel capacity and spectrum efficiency [1, 2]. In a MIMO system, multiple antenna elements need to be packed in a restricted space, so that the separations between adjacent antennas are quite limited. However, mutual coupling effects between antenna elements severely deteriorates the performance of system. An inter-element spacing less than half a wavelength will make the influence of mutual coupling more devastating [3–5].

Recently, the suppression of mutual coupling in MIMO antenna arrays has attracted great interest in academia and industry. Typically, an in-band isolation of -17 dB is normally sufficient for small-scale MIMO

transmission [6–9]. Nevertheless, a lower mutual coupling level is critical since the efficiency of power amplifiers and active voltage standing wave ratio (VSWR) of array elements would also be influenced by mutual coupling in massive MIMO [3]. For instance, an active VSWR of the MIMO antennas would be higher than 6 at 15 dB isolation, and if the isolation is improved to more than 25 dB, the VSWR can be less than 2 [10–12]. Moreover, strong coupling in communication systems impacts radiation patterns of antenna elements and will cause nonlinear effects that decrease the amplifier efficiency [13, 14]. Therefore, the isolation level among massive MIMO elements is recommended to be better than 25 dB [15–17].

In the past decade, plentiful accomplishments have been published on the suppression of mutual coupling. For instance, Wu et al. proposed the concept of an antenna-array decoupling surface [12], which can introduce additional reflected electromagnetic waves to counteract the mutual coupling between adjacent elements. A similar technique is the decoupling ground [18]. Decoupling dielectric stubs can reduce mutual coupling of dual-polarized by localizing the electromagnetic field emitted by antenna elements, thus weakening the electromagnetic couplings to adjacent antenna elements [19]. Nevertheless, these methods inevitably increase the antenna profile.

Inserting dummy elements between antenna elements is a prevalent decoupling method. Chiu et al. proposed defective ground structures (DGS) to improve the isolation between planar inverted F antennas, patches, and monopoles [20]. However, conventional DGSs break the ground plane, increasing backward radiation. Besides, DGS is designed to be useful only for specific coupling situations. To improve the applicability of DGS design, Zhang et al. proposed a novel pixelated surface ground structure which can be utilized to various antenna designs [21]. Yang et al. introduced electromagnetic bandgap (EBG) structures between two patch antennas as a band-stop filter to reduce mutual coupling by 8 dB [22]. Yu et al. proposed a 3-D meta-material structure

(3DMMS), which prevents surface wave propagation through negative permeability and achieves isolation enhancement of more than 18 dB [23]. Nevertheless, EBG structures require large areas and therefore cannot be applied to compact arrays. Apropos of 3DMMS, its decoupling bandwidth is relatively limited. Neutralization lines (NL), counteracting the original coupling wave by introducing an extra coupling path, is an efficient method for decoupling dual-element antenna systems [24]. In [25], Luo et al. reported a MIMO antenna array with both metamaterial and neutralization line technology, which achieves gain and isolation enhancement of about 3dB and 30dB respectively. Otherwise, sparse MIMO arrays designed with the strategy of uniform linear array fitting principles can mitigate the mutual coupling [26]. Unfortunately, their complexity increases drastically for large antenna arrays.

More applicable for microstrip antenna than above works, adding a decoupling structure at feeding layer has preferences of low profile and small impact on antennas' radiation performance. For closely coupled binary arrays, lumped decoupling technologies have been investigated in detail in [7] and [27]. However, LC components may introduce parasitic effects, reducing the radiation efficiency. Alternatively, transmission line-based decoupling methods are more attractive. For instance, Cheng et al. designed a microstrip line-based decoupling network for two strongly coupled, asymmetric and unmatched antenna elements [8], where an analytical design formula has been provided. Decoupling networks for patch antenna arrays with single linear polarization were fabricated in [28] and [29]. Zhang et al. first applied the transmission line-based decoupling network to dual-polarized MIMO antenna arrays, eliminating mutual coupling between the vertical, horizontal, and diagonal pairs of elements without degrading the isolation of cross-polarized ports [10]. Furthermore, a decoupling method with filtering response based on T-shaped transmission line is applied to  $4 \times 4$  patch antenna array [30]. Despite that the isolations in these designs are higher than 30 dB, their network configurations are complex. Recently, a novel aperture loading decoupling concept has been reported in [31]. By introducing an additional coupling path between adjacent elements through the feeding line and coupling aperture, the mutual coupling between two adjacent antennas can be reduced to less than -25 dB. Since no additional impedance matching network is required, this method is more convenient for large-scale dual polarization microstrip antennas.

Circularly polarized (CP) antennas are widely applied in navigation and communication systems due to their superior ability to suppress multipath fading and polarization mismatch. However, studies on reducing coupling between large-scale circularly polarized

microstrip antennas are quite rare [32–34]. In general, decoupling of CP arrays are more difficult than that for dual-linear-polarized arrays because the former require both linearly polarized components to be equally suppressed by the decoupling technique [33].

In this paper, we apply the aperture-loaded decoupling concept to CP array antennas. By etching small apertures at the ground plane, the feeding line of an element can generate additional coupling path with its adjacent antenna element through an aperture. With appropriate dimensions, these coupling apertures will cancel out the original coupling. Compared with existing decoupling methods of CP microstrip antennas, the proposed scheme features simple structure, higher decoupling efficiency, and low profile.

## II. ANALYSIS OF THE CIRCULARLY POLARIZED DECOUPLING STRATEGY

In this section, the principle of decoupling approach is illustrated analytically. Figure 1 indicates the proposed CP patch antennas decoupling method, which consists of three identical elements, labelled as Antennas 1, 2, and 3. The operating frequency of patch antennas in this work is 3.38 GHz. The centre distance between adjacent patches is  $0.5 \lambda_0$ , where  $\lambda_0$  is the free-space wavelength at the centre frequency. In particular, a chamfer length  $L_c$  provides two slightly separated resonant frequencies to achieve circular polarization with single-feed structure. Below the edge of each antenna element, two coupling apertures are etched into the ground layer. For comprehensive consideration, we take Antenna 2 as the reference antenna for analysis. The feeding line of Antenna 2 passes through the apertures loaded under Antennas 1 and 3 successively, generating extra coupling paths with

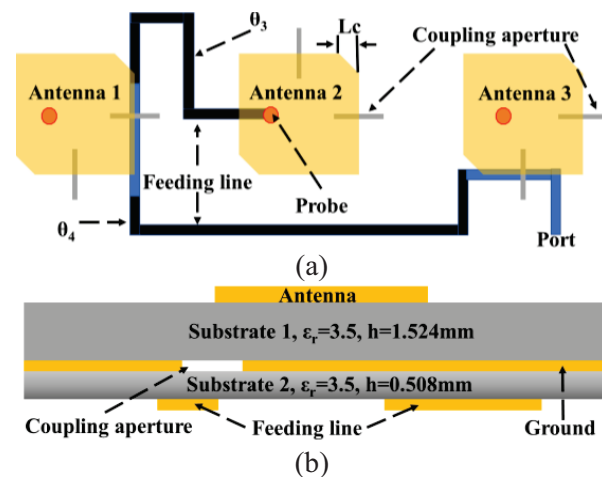


Fig. 1. Geometries of the proposed CP patch antenna decoupling method. (a) Top view. (b) Lateral view. ( $L_c=2.4\text{mm}$ ,  $\theta_3=470^\circ$  and  $\theta_4=860^\circ$ .)

its adjacent antennas. By adjusting the size of the coupling aperture, the level of the new coupling path between two antennas can be optimized. When those two couplings have similar magnitudes and opposite phases, high isolation can be achieved.

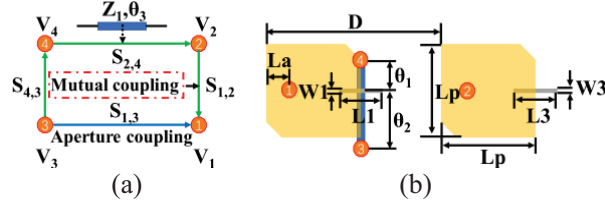


Fig. 2. Configuration of the decoupling between Antennas 1 and 2. (a) Signal flow diagram. (b) Simplified four-port model. ( $\theta_1=45^\circ$ ,  $\theta_2=90^\circ$ , and  $L_a=6.8$  mm,  $L_1=4.6$  mm,  $L_3=4$  mm,  $W_1=W_3=0.2$  mm,  $L_p=22.7$  mm.)

For single-feed CP antenna, each element needs to be decoupled from the adjacent antennas on the right and left sides through a single microstrip line. Subsequently, the decoupling process of the CP array can be divided into two similar and related steps, as shown in Figs. 2 and 3. The signal flow diagram for the decoupling between Antennas 1 and 2 is shown in Fig. 2 (a), where two different coupling paths are indicated by green and blue arrows, respectively. The corresponding simplified four-port model is given in Fig. 2 (b). Define  $V_3$  as the input voltage of Node 3. At Node 1, the output voltage is determined by these two paths, which can be written separately as:

$$V_{1,B} = S_{1,3}V_3, \quad (1.a)$$

$$V_{1,G} = S_{4,3}S_{2,4}S_{1,2}V_3, \quad (1.b)$$

where  $S_{1,3}$  indicates the coupling through the loaded aperture, while the mutual coupling between radiation elements is denoted as  $S_{1,2}$ . According to transmission line theory,

$$S_{2,4} = \frac{2Z_0Z_1}{2Z_0Z_1\cos\theta_3 + j(Z_0^2 + Z_1^2)\sin\theta_3}. \quad (2)$$

For Nodes 3 and 1, we can write the decoupling condition as:

$$V_1 = V_{1,G} + V_{1,B} = 0. \quad (3)$$

Combining (1)-(3), the design condition can be obtained as follows:

$$S_{1,3} + \frac{2Z_0Z_1S_{4,3}S_{1,2}}{2Z_0Z_1\cos\theta_3 + j(Z_0^2 + Z_1^2)\sin\theta_3} = 0. \quad (4)$$

As for  $S_{4,3}$ ,  $S_{1,3}$  and  $S_{1,2}$ , it can be conveniently obtained through full-wave simulations. Meanwhile, the impedance matching from Node 3 to Node 2 should also be properly considered.

Figure 3 (a) illustrates the decoupling signal flow diagram of Antennas 2 and 3, with the condition that An-

tennas 1 and 2 are already decoupled. The corresponding simplified model is given in Fig. 3 (b). By repeating the above derivation and analysis, the value of  $\theta_4$  and the aperture parameters can be determined. Attributed to non-centrosymmetric antenna elements, the decoupling parameters of odd-positioned elements are different to those of even-positioned. A four-element array decoupled by the proposed method is depicted in Fig. 3 (c). After that, the  $xoz$  and  $yoz$  planes of each radiating element are decoupled with the  $xoz$  and  $yoz$  planes of its adjacent elements, respectively. This indicates that after decoupling, when a port is excited, its adjacent radiation patch apertures are in the voltage null. The area around the adjacent antenna elements can be considered as the quasi-voltage-zero region, thus suppressing the electromagnetic propagation. For ease of analysis, the characteristic impedance of all the transmission lines is chosen to be  $50 \Omega$ .

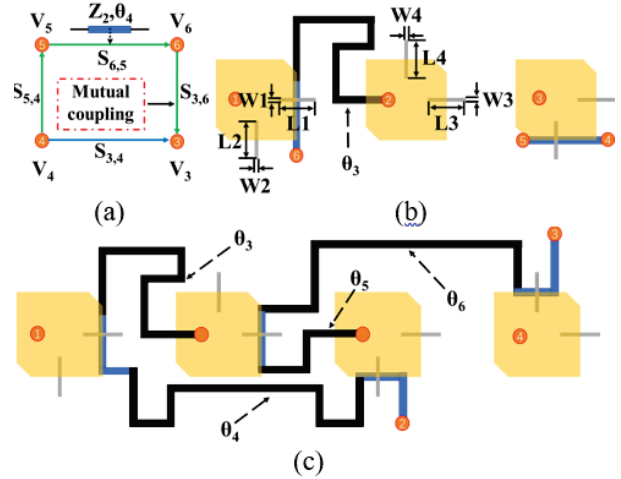


Fig. 3. Decoupling configuration of multiple antenna elements. (a) Signal flow diagram of the decoupling between Antennas 2 and 3. (b) Simplified six-port model. (c) Configuration of a four-element array with the proposed decoupling method. ( $\theta_5=258.3^\circ$ ,  $\theta_6=662.2^\circ$ , and  $L_2=4$  mm,  $L_4=4.8$  mm,  $W_2=W_4=0.2$  mm.)

### III. MEASUREMENT RESULTS AND DISCUSSION

To demonstrate the decoupling performance of the proposed prototype, an 8-element CP microstrip antenna array was fabricated and measured, as shown in Fig. 4. Both the ground plane, microstrip patch and feeding line are printed on F4B with a loss tangent of 0.002 and a dielectric constant of 3.5. The array antenna is fixed with some screws, of which metal screws are used at the outmost sides and nylon screws are used for the parts close to the patch. All screws have been taken into account during electromagnetic simulations. The overall

size of this antenna array is  $440 \times 90 \text{ mm}^2$ . The radiation performance and S-parameters of the proposed array are measured.

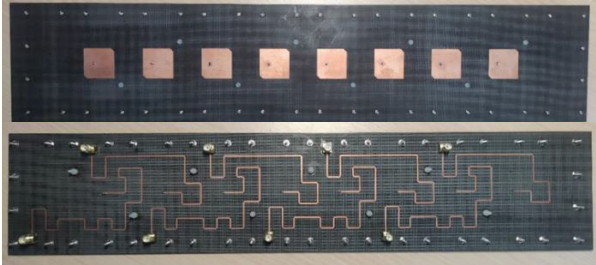


Fig. 4. Photograph of the fabricated  $1 \times 8$  antenna array.

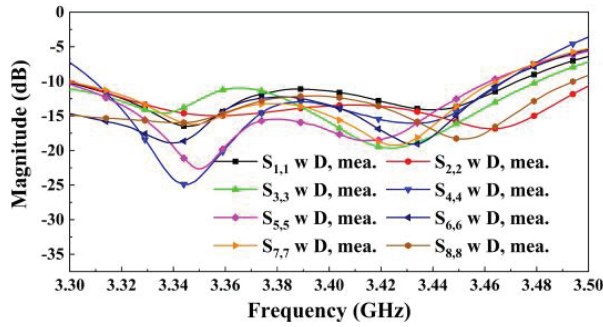
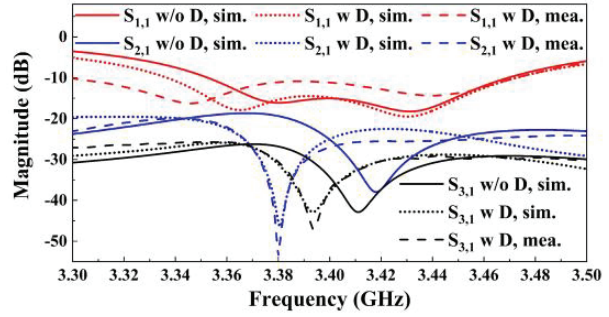


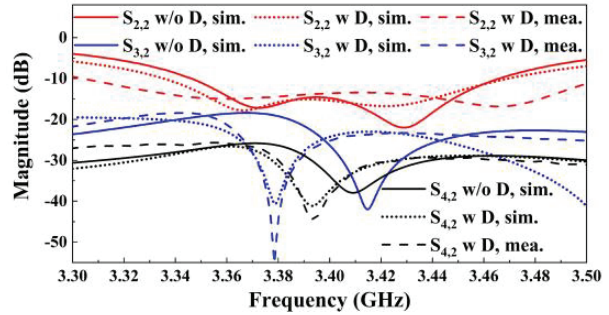
Fig. 5. Measured scattering parameters of the fabricated  $1 \times 8$  array.

The measured reflection coefficients of the fabricated patch antenna array are depicted in Fig. 5. One can immediately see that the reflection coefficients of the 8 ports are better than  $-10 \text{ dB}$  in the frequency range of  $3.31\text{-}3.45 \text{ GHz}$ . The reflection coefficients and ports isolations of some representative ports are plotted in Fig. 6. It demonstrates that the maximum mutual coupling level occurs between adjacent ports, and ports isolation are remarkably enhanced after decoupling, increasing from  $18.7 \text{ dB}$  to more than  $30 \text{ dB}$  at around  $3.38 \text{ GHz}$  (where the axial ratio is below than  $3 \text{ dB}$ ). It is worth mentioning that the measured impedance bandwidth is wider than the simulated one. This may be caused by air gaps due to assembly tolerances and non-ideal contacts.

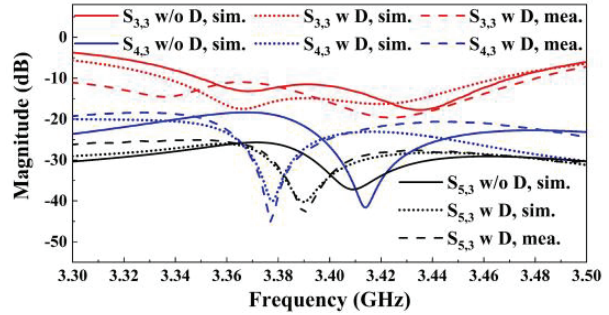
Figure 7 depicts the comparison of axial ratio (AR) of the CP antenna array with and without decoupling of Ports 1-4. It is observed that the AR of all ports improves after decoupling. A  $3\text{-dB}$  AR bandwidth from  $3.36$  to  $3.4 \text{ GHz}$  is achieved for all four ports, which is slightly better than the simulation one. It suggests that the antenna array has excellent CP characteristics, and the reduction of coupling can significantly improve the AR of the patch antenna elements.



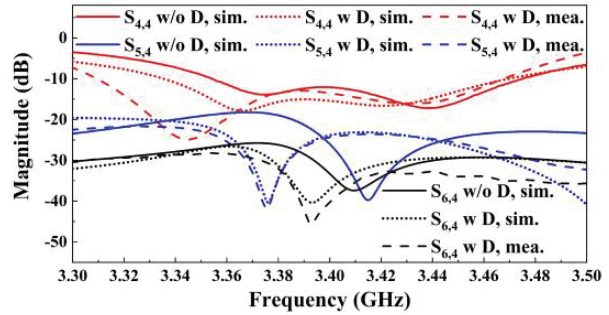
(a)



(b)



(c)



(d)

Fig. 6. Measured and simulated S-parameters of representative ports. (a) Port 1. (b) Port 2. (c) Port 3. (d) Port 4.

Figure 8 plots the simulated and measured radiation patterns of LHCP and RHCP of Ports 2-4 at  $3.38 \text{ GHz}$  with and without decoupling. It can be found that the radiation patterns of three elements are almost the same as the ones before decoupling. This

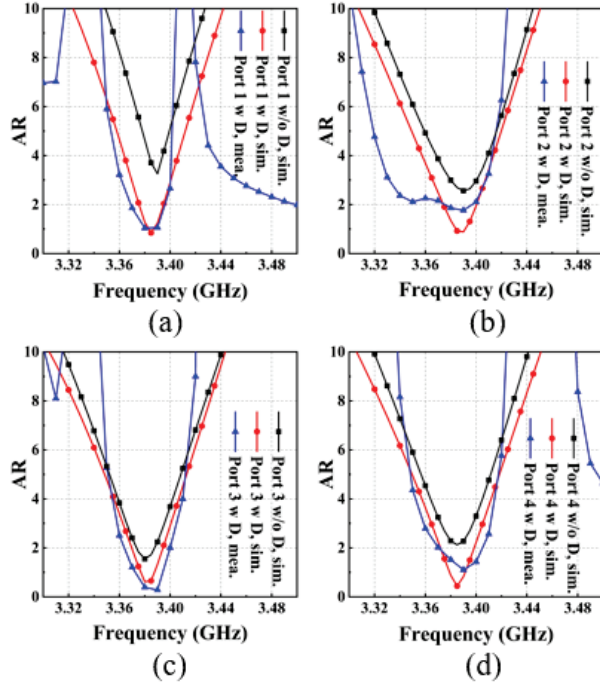


Fig. 7. Measured and simulated AR of representative ports. (a) Port 1. (b) Port 2. (c) Port 3. (d) Port 4.

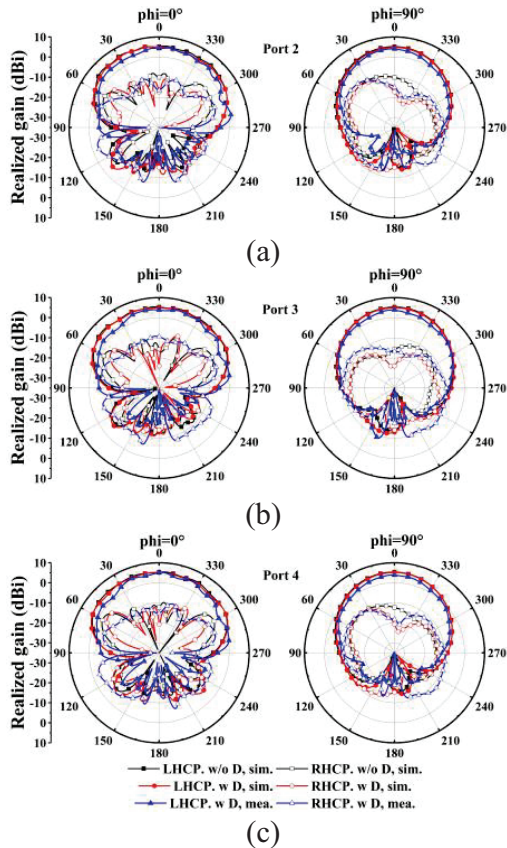


Fig. 8. Measured and simulated radiation patterns of representative ports. (a) Port 2. (b) Port 3. (c) Port 4.

demonstrates that the proposed decoupling strategy has faint effect on the radiation patterns of array antenna. As for the measurement results, they are marginally deteriorating than the simulation results. The discrepancy is mainly caused by measurement error and manufacturing tolerance.

Table 1: Performance comparison with published decoupling methods

Ref.	No. of Antennas	Polarization	Isolation	Profile
[10]	16	Dual-linear	$\geq 25$ dB	$0.09 \lambda_0$
[31]	16	Dual-linear	$\geq 25$ dB	$0.08 \lambda_0$
[19]	16	Dual-linear	$\geq 25$ dB	$0.47 \lambda_0$
[32]	4	Circular	$\geq 19$ dB	$0.09 \lambda_0$
[34]	2	Circular	$\geq 50$ dB	$0.012 \lambda_0$
This work	8	Circular	$\geq 25$ dB	$0.02 \lambda_0$

A detailed comparison of recently published decoupling works for linearly polarized and circularly polarized patch antenna array is summarized in Table 1. We are concerned with the polarization mode, antenna profile, and isolation between two ports. Compared to [10], our proposed decoupling scheme is of low complexity and superior in design simplicity. The proposed decoupling methods in [10] and [19] are only validated for antenna arrays with dual-linear-polarizations. The mutual coupling between antennas in [32] does not decrease below  $-20$  dB, thus its applications in massive MIMO are limited. Moreover, the profile of the proposed prototype in this work is only  $0.02 \lambda_0$ , which is far less than those in [10, 19, 31, 32]. In [34], on account of appreciable damage to the ground plane, the backward radiation is deteriorated distinctly. The decoupling bandwidth of the antenna proposed in this work is comparable to its 3-dB AR bandwidth, which is usually small for single-feed CP antennas. In general, the presented decoupling strategy shows overall superiority to the previous works.

#### IV. CONCLUSION

CP antennas have been heavily employed in satellite communications and navigation systems, yet there are few papers about the decoupling of CP patch antennas. Focusing on the status quo, a compact and low-profile decoupling strategy to enhance the isolation within  $1 \times 8$

CP microstrip antenna array has been proposed in this paper. An additional coupling path could be generated through a coupling aperture to counteract the mutual coupling, which considerably enhances the isolation between antenna elements. Furthermore, both impedance bandwidth and AR could be improved using the proposed scheme.

### ACKNOWLEDGMENT

This work was supported by the National Key Research and Development Program of China under Grant 2022YFB3902400.

### REFERENCES

- [1] A. Zaidi, F. Athley, J. Medbo, U. Gustavsson, and G. Durisi, *5G Physical Layer: Principles, Models and Technology Components*, Academic Press, London, U.K., 2018.
- [2] H. Pei, X. Chen, X. Huang, X. Liu, X. Zhang, and Y. Huang, "Key issues and algorithms of multiple-input-multiple-output over-the-air testing in the multi-probe anechoic chamber setup," *Sci. China: Inf. Sci.*, vol. 65, no. 3, 131302, Mar. 2022.
- [3] X. Chen, S. Zhang, and Q. Li, "A review of mutual coupling in MIMO systems," *IEEE Access*, vol. 6, pp. 24706-24719, Apr. 2018.
- [4] J. W. Wallace and M. A. Jensen, "Mutual coupling in MIMO wireless systems: A rigorous network theory analysis," *IEEE Trans. Wireless Commun.*, vol. 3, no. 4, pp. 1317-1325, Jul. 2004.
- [5] Y. Da, X. Chen, and A. A. Kishk, "In-band mutual coupling suppression in dual-band shared-aperture base station arrays using dielectric block loading," *IEEE Trans. Antenna Propag.*, vol. 70, no. 10, pp. 9270-9281, Oct. 2022.
- [6] K. Qian, L. Zhao, and K. Wu, "An LTCC coupled resonator decoupling network for two antennas," *IEEE Trans. Microw. Theory Techn.*, vol. 63, no. 10, pp. 3199-3207, Oct. 2015.
- [7] H. Meng and K. Wu, "An LC decoupling network for two antennas working at low frequencies," *IEEE Trans. Microw. Theory Techn.*, vol. 65, no. 7, pp. 2321-2329, Jul. 2017.
- [8] Y. Cheng and K. M. Cheng, "A novel dual-band decoupling and matching technique for asymmetric antenna arrays," *IEEE Trans. Microw. Theory Techn.*, vol. 66, no. 5, pp. 2080-2089, May 2018.
- [9] B. Qian, X. Chen, and A. A. Kishk, "Decoupling of microstrip antennas with defected ground structure using the common/differential mode theory," *IEEE Antennas Wireless Propag. Lett.*, vol. 20, no. 5, pp. 828-832, May 2021.
- [10] Y. Zhang, S. Zhang, J. Li, and G. F. Pedersen, "A transmission-line-based decoupling method for MIMO antenna arrays," *IEEE Trans. Antennas Propag.*, vol. 67, no. 5, pp. 3117-3131, May 2019.
- [11] M. Li, X. Chen, A. Zhang, W. Fan, and A. A. Kishk, "Split-ring resonator-loaded baffles for decoupling of dual-polarized base station array," *IEEE Antennas Wireless Propag. Lett.*, vol. 19, no. 10, pp. 1828-1832, Oct. 2020.
- [12] K. Wu, C. Wei, X. Mei, and Z. Zhang, "Array-antenna decoupling surface," *IEEE Trans. Antennas Propag.*, vol. 65, no. 12, pp. 6728-6738, Dec. 2017.
- [13] C. Fager, X. Bland, K. Hausmair, J. C. Cahuana, and T. Eriksson, "Prediction of smart antenna transmitter characteristics using a new behavioral modeling approach," *IEEE MTT-S Int. Microw. Symp. Dig.*, Tampa, FL, USA, pp. 1-4, Jun. 2014.
- [14] F. Peng, F. Yang, B. Liu, and X. Chen, "Experimental investigation of decoupling effect on the nonlinearity of power amplifiers in transmitter array," *Applied Computational Electromagnetics Society (ACES) Journal*, in press.
- [15] B. Wang, Y. Chang, and Y. Sun, "Performance of the large-scale adaptive array antennas in the presence of mutual coupling," *IEEE Trans. Antennas Propag.*, vol. 64, no. 6, pp. 2236-2245, Jun. 2016.
- [16] Y. Da, Z. Zhang, X. Chen, and A. A. Kishk, "Mutual coupling reduction with dielectric superstrate for base station arrays," *IEEE Antennas Wireless Propag. Lett.*, vol. 20, no. 5, pp. 843-847, May 2021.
- [17] Y. Zhang, S. Zhang, J. Li, and G. F. Pedersen, "A wavetrap-based decoupling technique for 45° polarized MIMO antenna arrays," *IEEE Trans. Antennas Propag.*, vol. 68, no. 3, pp. 2148-2157, Mar. 2020.
- [18] S. Song, Y. Da, B. Qian, X. Huang, X. Chen, Y. Li, and A. A. Kishk, "Dielectric resonator magnetoelectric dipole arrays with low cross polarization, backward radiation, and mutual coupling for MIMO base station applications," *China Communications*, in press.
- [19] P. Mei, Y. Zhang, and S. Zhang, "Decoupling of a wideband dual-polarized large-scale antenna array with dielectric stubs," *IEEE Trans. Veh. Technol.*, vol. 70, no. 8, pp. 7363-7374, Aug. 2021.
- [20] C. Chiu, C. Cheng, R. D. Murch, and C. R. Rowell, "Reduction of mutual coupling between closely-packed antenna elements," *IEEE Trans. Antennas Propag.*, vol. 55, no. 6, pp. 1732-1738, Jun. 2007.
- [21] Y. Zhang, S. Shen, Z. Han, C. Chiu, and R. Murch, "Compact MIMO systems utilizing a pixelated surface: capacity maximization," *IEEE Trans. Veh. Technol.* vol. 70, no. 9, pp. 8453-8466, Sep. 2021.

- [22] F. Yang and Y. Rahmat-Samii, "Microstrip antennas integrated with electromagnetic band-gap (EBG) structures: A low mutual coupling design for array applications," *IEEE Trans. Antennas Propag.*, vol. 51, no. 10, pp. 2936-2946, Oct. 2003.
- [23] K. Yu, Y. Li, and X. Liu, "Mutual coupling reduction of a MIMO antenna array using 3-D novel meta-material structures," *Applied Computational Electromagnetics Society (ACES) Journal*, vol. 33, no. 7, pp. 758-763, Mar. 2018.
- [24] A. Diallo, C. Luxey, P. L. Thuc, R. Staraj, and G. Kossiavas, "Study and reduction of the mutual coupling between two mobile phone pifas operating in the DCS1800 and UMTS bands," *IEEE Trans. Antennas Propag.*, vol. 54, no. 11, pp. 3063-3074, Nov. 2006.
- [25] S. Luo, Y. Li, Y. Xia, and L. Zhang, "A low mutual coupling antenna array with gain enhancement using metamaterial loading and neutralization line structure," *Applied Computational Electromagnetics Society (ACES) Journal*, vol. 34, no. 3, pp. 411-418, Mar. 2019.
- [26] W. Shi, X. Liu, and Y. Li, "ULA fitting for MIMO radar," *IEEE Commun Lett.*, vol. 26, no. 9, pp. 2190-2194, Sep. 2022.
- [27] C. Wu, C. Chiu, and T. Ma, "Very compact fully lumped decoupling network for a coupled two-element array," *IEEE Antennas Wireless Propag. Lett.*, vol. 15, pp. 158-161, 2016.
- [28] R. Xia, S. Qu, P. Li, D. Yang, S. Yang, and Z. Nie, "Wide-angle scanning phased array using an efficient decoupling network," *IEEE Trans. Antennas Propag.*, vol. 63, no. 11, pp. 5161-5165, Nov. 2015.
- [29] X. Zou, G. Wang, Y. Wang, and H. Li, "An efficient decoupling network between feeding points for multielement linear arrays," *IEEE Trans. Antennas Propag.*, vol. 67, no. 5, pp. 3101-3108, May 2019.
- [30] Y. Zhang, Q. Ye, G. F. Pedersen, and S. Zhang, "A simple decoupling network with filtering response for patch antenna arrays," *IEEE Trans. Antennas Propag.*, vol. 69, no. 11, pp. 7427-7439, Nov. 2021.
- [31] Y.-M. Zhang and S. Zhang, "A novel aperture-loaded decoupling concept for patch antenna arrays" *IEEE Trans. Microw. Theory Techn.*, vol. 69, no. 9, Sep. 2021.
- [32] C. Mao, S. Gao, Y. Wang, and J. T. S. Sumantho, "Compact broadband dual-sense circularly polarized microstrip antenna/array with enhanced isolation," *IEEE Trans. Antennas Propag.*, vol. 65, no. 12, pp. 7073-7082, Dec. 2017.
- [33] B. Liu, X. Chen, J. Tang, A. Zhang, and A. A. Kishk, "Co- and cross-polarization decoupling structure with polarization rotation property between linearly polarized dipole antennas with application to decoupling of circularly polarized antennas," *IEEE Trans. Antennas Propag.*, vol. 70, no. 1, pp. 702-707, Jan. 2022.
- [34] D. Gao, Z. Cao, S. Fu, X. Quan, and P. Chen, "A novel slot-array defected ground structure for decoupling microstrip antenna array," *IEEE Trans. Antennas Propag.*, vol. 68, no. 10, pp. 7027-7038, Oct. 2020.



**Xin Cheng** received his Bachelor's degree in Optical Information Science and Technology from Shaanxi University of Science & Technology, Xi'an, China, in 2016. He is currently pursuing a Ph.D. degree in Electronic Science and Technology with Xi'an Jiaotong University,

Xi'an, China. His current research interests include antenna array decoupling techniques and gap waveguide technology.



**Bingyi Qian** received his B.S. degree in Electronics and Information Engineering from Xidian University, Xi'an, China, in 2020, where he is currently pursuing an M.S. degree in Electronics Science and Technology from Xi'an Jiaotong University, Xi'an. His current research interests

include microstrip antenna design, mutual coupling reduction, and 5G mobile antennas.



**Le Chang** received his B.S. degree in Electronics and Information Engineering from Xidian University, Xi'an, China, in 2012, and his Ph.D. degree in Electrical Engineering from Tsinghua University, Beijing, China, in 2017. From 2017 to 2020, he was with the Antenna and

RF Group, Huawei Device Ltd., Beijing, where he worked as a Senior Engineer. Since 2021, he has been a Special Appointed Researcher with Xi'an Jiaotong University, Xi'an. His current research interests include 5G mobile antennas, millimeter-wave antennas, and phased arrays.



**Jinlin Liu** received his B.Sc. degree in communications engineering from the University of Electronic Science and Technology of China, Chengdu, China, in 2005. He received the Vordiploma degree from the Munich University of Technology, Munich, Germany, in 2011, and the Swedish Licentiate degree and Ph.D. degree from the Chalmers University of Technology, Gothenburg, Sweden, in 2016 and 2019, respectively. From 2005 to 2007, he was with Intel, Chengdu branch, as a Test Engineer. From 2013 to 2014, he was with Eurodesign GmbH, Munich, as a PCB Test Engineer. His current research interests include fundamental electromagnetic theory, millimeter-wave planar antennas in general, gap waveguide technology, and frequency-selective surfaces. He received the Best Student Paper Award First Place at the 2017 International Symposium on Antennas and Propagation. He serves on the Review Board for several journals, including the *IEEE Transactions on Antennas and Propagation*, the *IEEE Transactions on Microwave Theory and Techniques*, the *IEEE Transactions on Components, Packaging, and Manufacturing*, the *IEEE Antennas and Wireless Propagation Letters*, the *IEEE Microwave and Wireless Components Letters*, and the *Journal of Electromagnetic Waves and Applications*.



**Xiaoming Chen** received his B.Sc. degree in electrical engineering from Northwestern Polytechnical University, Xi'an, China, in 2006, and his M.Sc. and Ph.D. degrees in electrical engineering from the Chalmers University of Technology, Gothenburg, Sweden, in 2007 and 2012, respectively. From 2013 to 2014, he was a Post-Doctoral Researcher with the Chalmers University of Technology. From 2014 to 2017, he was with Qamcom Research and Technology AB, Gothenburg, Sweden. Since 2017, he has been a Professor at Xi'an Jiaotong University, Xi'an. His current research interests include multi-in multi-out (MIMO) antennas, over-the-air (OTA) testing, reverberation chambers, and hardware impairments and mitigation. Prof. Chen serves as a Senior Associate Editor (AE) for *IEEE Antennas and Wireless Propagation Letters*. He received the Outstanding AE Award in 2018, 2019, 2020, 2021, and 2022. He received the URSI (International Union of Radio Science) Young Scientist Award in 2017 and 2018.

# Simultaneous Transmit and Receive Phased Array System Architecture and Prototype Comprehensive Verification

Jie Zhang and Hongchao Wu

Nanjing Research Institute of Electronics Technology  
Nanjing, 210039, China  
zjwj2011@sina.com

**Abstract** – In the future multi-functional detection sensing and communication integrated systems, as well as 5G/6G systems, simultaneous transmit and receive technology, as an important key technology, is an important supporting measure to achieve the simultaneous work of different functions. Looking at the problem of strong self-interference in the simultaneous multi-function application of a phased array transceiver, this paper presents the integrated cancellation architecture and corresponding method of integrated transmission domain, RF domain and digital domain, and completes principle experiment verification of interference suppression and elimination by constructing the principle experiment system. Experimental results show that in the actual hardware system 0.5 db amplitude quantification and 6-bit phase quantization control conditions, through joint using passive and active beam transfer of the domain space optimization form, at the same time in the digital domain application of the adaptive system identification interference cancellation method for further interference cancellation, above 150 dB for interference suppression can be achieved. This research will provide a certain reference for the application of simultaneous transceiver technology in future 5G/6G phased array antenna systems.

**Index Terms** – prototype verification, self-interference suppression, simultaneous transmit and receive, system architecture.

## I. INTRODUCTION

Current radio systems, including radar, communications, and various electronic warfare (EW) measures, are mainly in half-duplex (HD) mode with transmit and receive functions. In order to utilize time effectively, and frequency and space resources with the development of radio hardware systems, especially adaptive signal processing, innovative full-duplex (FD) methods are proposed to make up for the shortcomings of HD. FD is considered a breakthrough technology for 5G and 6G. Although FD can bring many benefits, a serious

problem in practical implementation is the strong self-interference when both transmitter and receiver work simultaneously, which can severely shield the receiver, making it unable to receive signals of interest from remote transmission or return weak signals [1–9].

FD technology aims to transmit and receive simultaneously in the same frequency band. In this case, the RF system receives not only the signal of interest, but also the transmitted coupled or leaky signal, which becomes the essential problem of simultaneous transmission and reception in radio systems. Therefore, the strength of the self-interfering signal at the receiver must be sufficiently reduced so that the radio system's own transmission does not interfere with its normal reception of the signal of interest. Especially for the phased array system with multiple transceiver units, the components and magnitudes of self-interference and cross-interference between units are obviously higher than those of conventional RF systems [7–12].

For achieving sufficient isolation between transmission and reception, there is usually a need to combine different technologies, including spatial isolation suppression, and analog and digital cancellation. In the application of a single channel FD radio system, these technologies can be integrated to satisfy the need for self-interference suppression. While for phased array, especially digital phased array which has hundreds of antenna cells, the mutual coupling paths among different elements are profuse. To apply the FD method in phased array, the complex channel's characteristic of the coupling paths must be analyzed and modeled before self-interference cancellation, using relevant technologies [3–6].

In [7] and [8], the aperture level of simultaneous transmit and receive configuration of a phased array for simultaneous transmission and reception was proposed and simulated, and preliminary experiments with a one-dimensional linear array of eight elements were carried out. That work mainly considered the case where the amplitude and phase of the array can be adjusted in an all-digital mode. In [10] and [11], the authors studied FD

millimeter wave communication based on beamforming mainly focused on the controllable amplitude and/or phase of the array weights. Through a comprehensive analysis of relevant literature [7–26], we can see that, as an important key technology to realize the elimination of simultaneous coupling interference suppression in a phased array system, it is necessary to realize the unsaturation of the receiving channel of the large array system while taking into account the realization of the system by making full use of the multi-unit multi-freedom characteristics in the array system airspace/transmission domain to suppress self-interference. In [23–25], the MIMO system and state-of-the-art decoupling works were studied by means of a special array antenna structure design, which can provide a good reference for self-interference suppression of the array system in the transmission domain. On the basis of the phased array digital domain adaptive system identification and cancellation filtering principle and experimental research [6, 19], as the first level of the interference suppression multi-level method, the work in [12] is mainly for the actual phased array system aperture-level simultaneous transmit and receive realization of self-interference suppression in transmission domain, the principle model and corresponding optimization methods under the practical limiting factors such as limited quantization number, constant envelope amplitude, scanning mode, wideband signal mode, etc.

On the basis of the above research, this work makes a systematic study of the strong self-interference problem faced by the simultaneous application of phased array transceiver and receiver. It proposes the integrated cancellation architecture and corresponding method of integrated transmission domain, RF domain and digital domain, and conducts the principle test of interference suppression and cancellation by constructing a principle test system. The results show that the multi-domain and multi-level joint architecture and method can achieve good results in the elimination of strong self-interference in the simultaneous transmit and receive phased array system. This research will provide a certain reference for the application of simultaneous transmit and receive technology in future 5G/6G array antenna systems.

This paper is structured as follows. The coupling self-interference electromagnetic model of simultaneous transmitting and receiving phased array is introduced in Section II. The system architecture and method of coupled self-interference signal suppression for simultaneous transmit and receive phased arrays are analyzed in detail in Section III. Section IV presents practical results of proof-of-principle for the proposed architecture and method by building a principle test system. Section V summarizes the paper and prospects for the future work.

## II. COUPLING SELF-INTERFERENCE ELECTROMAGNETIC MODEL OF SIMULTANEOUS TRANSMITTING AND RECEIVING PHASED ARRAY

From previous research work [6, 8, 12], the self-interference channel characteristics  $[H(f)]_{M \times N}$  directly determines the complexity of coupled self-interference and the feasibility of its suppression methods. Because the practical array antenna has complex three-dimensional configuration, the simple near-field model is not strictly accurate for characterization of the coupling interference in an array system [10, 11]. In order to better simulate the channel characteristics of the coupling interference between the transmitting unit and the receiving unit in this experimental array, we introduce an electromagnetic model of the array based on Ansoft HFSS. The HFSS apply FEM to calculate the S-parameter matrix  $S$  and full-wave electromagnetic field of arbitrary array antenna configuration.

The  $p$ -th row and  $q$ -th column of the  $S$  matrix are represented as  $S(p, q)$ , ( $p, q = 1, 2, \dots, P$ ), which represents the coupling relationship between the  $p$ -th and  $q$ -th elements in the array.  $P$  is the total number of elements in the array. Based on the S-parameter matrix  $S$ , we define the element  $H(m, n)$  of the array in  $m$ -th row and in the  $n$ -th column of the interference channel characteristic matrix  $[H]_{M \times N}$ , as:

$$H(m, n) = \sum_{q_n \in T_n} S(m, q_n), \quad (1)$$

$$(n = 1, 2, \dots, N; m = 1, 2, \dots, M).$$

In the formula,  $q_n$  is the unit number of the sub-array set for transmitting and/or receiving in the entire array,  $T_n$  is the unit set corresponding to the transmitting sub-array,  $N$  is the number of units of the transmitting sub-array, and  $M$  is the number of units of the receiving sub-array.  $R_m$  is the set of units corresponding to the receiving sub-array. For the separated-aperture array-level simultaneous transceiver mode, there is  $R_m \cap T_n = \emptyset$ ; for the partial array-level/partial unit-level simultaneous transceiver mode, there is  $R_m \cap T_n \neq \emptyset$ . Especially for the full-aperture unit-level transceiver simultaneous mode, there is  $R_m = T_n$ .

Based on the self-interference coupling model proposed above, we first construct an electromagnetic model and a digital model for the practical array system, conduct design simulation verification through digital methods, and use it for subsequent principle experiment verification and evaluation. In this work, we take the 30(T)×10(R) array antenna as the example, and study the interference characteristics of the sub-apertures level simultaneous transmit and receive mode.

When the separate sub-apertures transmission and reception work simultaneously, the transmission sub-array can be transmitted according to a certain beam-shaping weight, and the receiving sub-array can be

simultaneously received according to a certain receiving beam-shaping weight. The arrangement of the phased array antenna in this mode is shown in Fig. 1, and the power of each transmitting component is set to 30 dbm, which can be controlled by the joint weights of amplitude and/or phase.

In the research process, combined with the actual physical array antenna development, we design and construct the corresponding electromagnetic model and digital model. Among them, the electromagnetic model is used to electromagnetically analyze the self-interference coupling characteristics between the transmitting and receiving antenna elements. The simulation environment used is Ansoft HFSS. The FEM is used to electromagnetically analyze the coupling characteristics between any two array elements. The S parameter of the array is obtained by electromagnetic calculation. Then by choosing the same layout as the specific test array antenna, that is, a transmitting sub-array with 30 units in 5 rows and 6 columns and a receiving sub-array with 10 units in 5 rows and 2 columns, the S parameter of the array is converted to a coupling matrix H, as shown in Equation (1). The specific electromagnetic model of the array is shown in Fig. 1 (a). The digital model is that for the practical prototype array antenna, that is, the transmitting sub-array of 5 rows and 6 columns, and the receiving sub-array of 5 rows and 2 columns, by constructing a digital design simulation model with the same characteristics as the array unit layout and operating frequency. It is used for design simulation to evaluate the beam characteristics and interference suppression performance of the different optimized weights. The specific digital model is shown in Fig. 1 (c). The practical testing array antenna is shown in Fig. 1 (b).

The saturation level of the receiving channel is generally about -10 dbm. In order to achieve conventional reception operation of the phased array system, the low noise amplifier on the receiving channel of each array element is firstly not saturated, that is, the power of the transmitting signal coupled to each receiving component must be below the saturation level of -10 dbm. By analyzing the self-interference coupling coefficients characteristics of the  $30(T) \times 10(R)$  array antenna as shown in Fig. 2 (a), the simulation coupling power at the receiving array elements can be obtained as shown in Fig. 2 (b). It can be seen that for the 30 dbm output power of the transmitting unit, the self-interference power received by the receiving array element is greater than the saturation power of the component by -10 dbm. As a result, all the receiving components are saturated and cannot receive the desired signal. However, the interference power received by different array elements varies greatly. Therefore, from the demand of SIC, it is necessary to suppress the self-interference signal power below

the saturation power level of the component in order to ensure the normal operation of the component. In this work, we will study the overall self-interference suppression of an array system by the multi-domain and multi-level method.

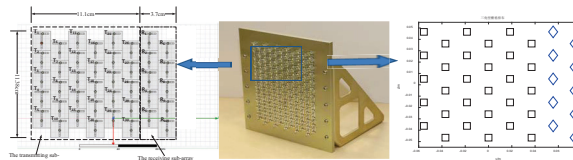


Fig. 1. Illustrative model and physical array antenna used for interference characteristics analysis. (a) HFSS EM model of the used array antenna (T: Transmitting element, R: Receiving element). (b) Practical testing array antenna. (c) Digital model of the array antenna ( $\square$ : Transmitting element,  $\diamond$ : Receiving element).

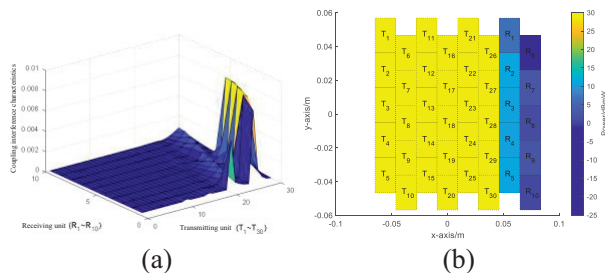


Fig. 2. Distribution characteristics of the coupling self-interference power for the illustrative array antenna operating simultaneous transmission and reception with the separate sub-apertures. (a) Coupling coefficients of the array antenna for the separate sub-aperture mode (10GHz). (b) Distribution characteristics of the coupling self-interference power (the digital unit in the Figure is dBm) for the separate sub-aperture mode.

### III. SYSTEM ARCHITECTURE AND METHOD FOR SIMULTANEOUS TRANSMISSION AND RECEPTION OF PHASED ARRAY COUPLED SELF-INTERFERENCE SIGNAL SUPPRESSION

Based on previous related research work [1, 12, 21–29], in order to solve the problem of strong self-interference in the simultaneous application of an array system, interference suppression and cancellation can be carried out from multiple dimensions including transmission domain, RF domain, and digital domain. First of all, for different phased array transceivers, the self-interference signal power entering the receiver can be reduced by passive suppression, including antenna

isolation and beamforming in the transmission domain, to achieve the first level of interference suppression. Radio frequency interference cancellation, composed of self-interference reference signal generation, delay and amplitude adjustment, and RF anti-inversion signal synthesis, reduces the signal power of the low-noise amplifier entering the receiving component to avoid component saturation. This is the second-level interference suppression. In the third stage, through active digital interference cancellation (such as adaptive filtering), the residual self-interference is eliminated to reduce the self-interference below the noise floor of the receiver, thereby avoiding affecting the reception of the desired signal by the system.

Figure 3 shows the principle block diagram of the multi-level self-interference suppression and cancellation of the phased array antenna at the same time of transmission and reception:

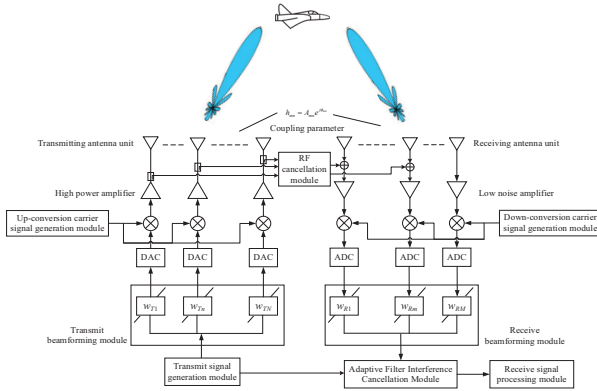


Fig. 3. Schematic diagram of phased array antenna narrow-band signal space-domain transmit and receive beam optimization principle.

According to the system architecture of the simultaneous multi-domain and multi-level self-interference cancellation of the phased array system as shown in Fig. 3, we propose the detailed process of interference cancellation according to the requirements of the actual system as follows:

#### A. Obtain the characteristic parameters of self-interference coupling between the transceiver arrays

(1) According to the unit arrangement characteristics of the phased array system to achieve simultaneous transmission and reception, the interference coupling characteristics between the transmitting array and the receiving array are obtained by means of electromagnetic calculation, array measurement or channel estimation, that is, the difference between the transmitting and receiving antenna units. The self-interference coupling characteristic matrix between  $H = [h_{mn}]_{M \times N}$ ,  $h_{mn} =$

$A_{mn}e^{j\phi_{mn}}$  is the receiving antenna unit  $m(m = 1, 2, \dots, M)$  and the transmitting antenna unit  $n(n = 1, 2, \dots, N)$  is the self-interference coupling coefficient, where  $N$  is the number of transmit antenna units, and  $M$  is the number of receive antenna units.

(2) Determine the antenna front radiation control parameters, and the amplitude/phase control quantization bit or quantization step.

#### B. Phased array modeling and spatial interference suppression optimization

(1) According to the working mode requirements and arrangement characteristics of the phased array system, combine the coupled self-interference characteristic relationship matrix used by the corresponding phased array to transmit and receive at the same time, and establish a digital array model [7, 8, 12].

(2) According to the characteristic indicators such as the radiation gain lobe of the phased array system and the simultaneous transmission and reception interference transmission suppression requirements, construct the beamforming weight parameter design optimization target calculation model, comprehensively analyze the beam characteristics and interference suppression performance, respectively shape the optimized transmission beam and receive beam and implement spatial interference suppression.

#### C. Cancellation preprocessing

Aiming at the nonlinear signal components existing in the process of transmission and transmission of the radio frequency system, a signal is coupled at the output end of the power amplifier of the transmission channel through a coupler as a cancellation reference signal. Set the carrier frequency of the radio frequency signal to be  $f_c$ , and the band-pass filter preprocessing with the passband bandwidth of  $B$  will filter out the harmonics and spurious components outside the bandwidth of the original reference signal and the received coupled reference interference signal, so as to retain the effective components within the passband. The effective component of the signal is used as the reference and desired signal for the input of the self-interference cancellation processing algorithm.

#### D. Self-interference cancellation processing in radio frequency domain

For the residual strong self-interference of the local array units and corresponding channels that still exist after the transmission domain interference suppression, the multi-tap delay, phase shift and attenuation methods are used to eliminate the radio frequency domain interference. Let the radiation signal output by the transmitting antenna through the power amplifier be  $s_n(t)(n = 1, 2, \dots, N', N' \leq N)$ . Due to the limited isolation between the transceiver units, the transmitted signal

enters the receiving antenna through spatial coupling and transmission domain interference suppression to form a self-interference signal  $s_{I,m}(t)$ . The transmitting signal of the coupling part of the transmitting end is used as a reference signal  $s_{r,n}(t) = c_{m,n}s_n(t)$ , and sent to the radio frequency cancellation module,  $c_{m,n}$  is the transmission coupling from the  $n$ -th channel reference coefficient. Usually considering factors such as bandwidth and spatial multipath transmission, the RF cancellation module adopts a multi-tap analog cancellation method [21]. Different taps have different delays, amplitudes and phases. Reconstruction of self-interfering signals. The receiver uses an adaptive optimization algorithm, such as the steepest descent method, to obtain the corresponding delay, amplitude and phase parameter control of different tap branches, so as to synthesize the corresponding self-interference cancellation signal  $\hat{s}_{I,m}(t)$ , the self-interference signal  $s_{I,m}(t)$  is eliminated in the radio frequency domain of the receiving end.

Let the RF signal of the  $m$ -th receiver be:

$$r_m(t) = d_m(t) + s_{I,m}(t) + \hat{s}_{I,m}(t) + n_m(t), \quad (2)$$

where  $d_m(t)$  represents the desired signal received, such as a long-range target scattered echo signal or a signal received by a long-range radio frequency system and is received at the local  $m$ -th receiver;  $s_{I,m}(t)$  represents the self-interference signal;  $\hat{s}_{I,m}(t)$  represents the locally synthesized self-interference cancellation signal;  $n_m(t)$  represents noise signal. The self-interference radio frequency signal  $s_{I,m}(t)$  of the local receiver is:

$$s_{I,m}(t) = (1-c)s(t) \otimes h_I(t), \quad (3)$$

where  $c$  represents the coupling coefficient between the transmitting antenna and the receiving antenna. Its value range is  $(0,1)$ . Then  $(1-c)$  represents the signal amplitude through the main channel.  $s(t)$  is the transmitter signal.  $h_I(t)$  represents the self-interference characteristics of the transmission channel from the transmitting antenna to the receiving antenna.  $\otimes$  represents the convolution of the transmitter and the self-interference channel.

The self-interference cancellation RF signal  $\hat{s}_{I,m}(t)$  synthesized by the local receiver is:

$$\begin{aligned} \hat{s}_{I,m}(t) &= \sum_{n=1}^N \hat{s}_{I,m,n}(t) \\ &= \sum_{n=1}^N \sum_{k=1}^K a_{k,m,n} e^{-j\varphi_{k,m,n}} s_{r,n}(t - \tau_{k,m,n}), \end{aligned} \quad (4)$$

where  $K$  is the number of analog cancellation channels,  $K \geq 2$ ,  $a_{k,m,n}$ ,  $\varphi_{k,m,n}$  and  $\tau_{k,m,n}$  ( $m = 1, 2, \dots, M$ ) are the amplitude attenuation value, phase shifter value and delay of each tap of the RF/analog cancellation.

During the transmitter training period signal transmission, assuming  $d(t) = 0$ , the radio frequency signal received by the receiver is:

$$\hat{r}(t) = s_I(t) + \hat{s}_I(t) + n(t). \quad (5)$$

In a specific time period, it is assumed to be  $[t_1, t_2]$ , ( $t_1 < t_2$ ). In order to minimize the residual interference

signal of the receiver, the amplitude of the signal  $\bar{r}(t)$  received by the receiver is integrated and the expectation is obtained. The optimized objective function with adjustable attenuation and phase shift parameters is as follows:

$$\begin{aligned} O(a, \varphi, \tau) &= E \left( \int_{t_1}^{t_2} |\bar{r}(t)|^2 dt \right) \\ &= E \left( \int_{t_1}^{t_2} |s_I(t) + \hat{s}_I(t) + n(t)|^2 dt \right). \end{aligned} \quad (6)$$

The optimal solution model is:

$$(a_o, \varphi_o, \tau_o) = \min_{a, \varphi, \tau} O(a, \varphi, \tau), \quad (7)$$

$$\text{s.t.} \begin{cases} 0 \leq a(n) \leq 1, n = 1, 2, \dots, N \\ -\pi \leq \varphi(n) \leq \pi, n = 1, 2, \dots, N \\ 0 \leq \tau(n) \leq \tau_{max} \end{cases}$$

where  $a$  represents the amplitude control vector of the multi-tap self-interference synthesis unit;  $\varphi$  represents the delay control vector of the multi-tap self-interference synthesis unit. As a result,  $a_o$ ,  $\varphi_o$  and  $\tau_o$  represent the optimal amplitude, phase and delay control vector values that are solved.

Considering the practical limitations of the effective bandwidth of the signal, the optimization can be done in the frequency domain:

$$\arg \min_{a, \varphi, \tau} [H_I(f) - H_r(f)]^2. \quad (8)$$

In the formula,  $H_I(f)$  represents the frequency domain response of the interference signal transmission channel;  $H_r(f)$  represents the frequency domain response of the reconstructed interference signal transmission channel.

Based on this, band-pass filtering is used to filter out harmonics and spurious components outside the bandwidth of the original reference signal and the coupled interference signal before the cancellation process, so as to retain the effective components of the signal. Use this as the reference signal and desired signal input to the self-interference cancellation processing algorithm.

## E. Digital domain interference cancellation processing

The residual interference signal after cancellation in the transmission domain and the radio frequency domain is further eliminated by the adaptive filtering system identification method in the digital domain. The basic principle is to characterize the interference channel as a multi-tap adaptive filter system, use the filter weights to weight the delayed signal to generate the output signal, and compare the output signal with the expected signal under a certain error criterion to adjust the weight value. After convergence, the transmission characteristics of the filter system are similar to the characteristics of the interference channel, and the subsequent transmitted signal can be approximated by the filter system to approximate the actual coupled interference signal, and the two are

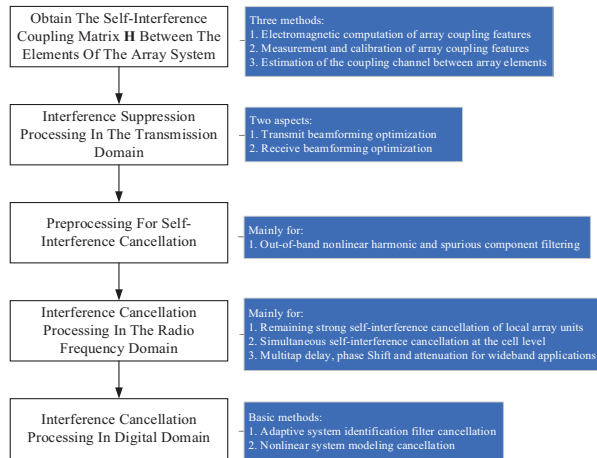


Fig. 4. Phased array coupled self-interference suppression process and method at the same time as transmission and reception.

subtracted to achieve the purpose of eliminating interference.

#### IV. PRINCIPLE EXPERIMENTAL EVALUATION

To evaluate the performance of the multi-domain joint self-interference suppression method, we use an experimental array antenna configured with 30 transmitting elements and 10 receiving elements. Passive spatial attenuation and active adaptive beamforming in the transmission domain and radio frequency domain are combined, and the adaptive identification filter cancellation method in the digital domain is also adopted. The test signal is a single frequency continuous wave signal. The transmitted signal of the array antenna is recorded as the reference signal for interference suppression and the received signal of the receiving unit is recorded as the signal for self-interference cancellation to evaluate and analyze the comprehensive effect of the joint interference cancellation method. The architecture and schematic diagram of the experiment system is shown in Figs. 5 and 6.

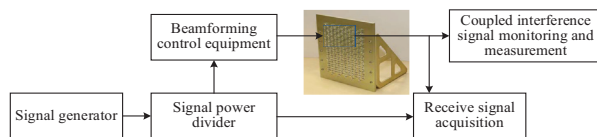


Fig. 5. Block diagram of the principle experiment architecture.

We jointly adopt passive spatial attenuation and active adaptive beam assignment in the transmission domain and RF domain, and adaptive identification filtering cancellation in the digital domain. The active beam

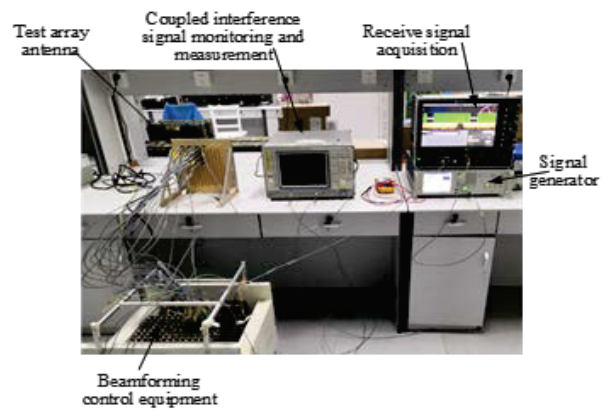


Fig. 6. Schematic diagram of interference cancellation principle experiment scene.

assignment method is the conventional beam assignment weight with  $0^\circ$ , azimuth angle  $0^\circ$  and optimization weight for interference suppression; adaptive identification filtering elimination in the digital domain adopts FIR model of order 256, and adopts adaptive filtering based on the minimum mean square error criterion. Considering the above methods, the experiment data results are shown in Fig. 7. Under the constraints of 0.5 db amplitude quantization and 6-bit phase quantization control of the practical hardware system, the spatial passive transmission of the transmission domain and the active beam optimization formation are jointly adopted. Also, the adaptive system identification interference cancellation method in the digital domain can achieve a total of more than 150 db self-interference cancellation. The verification of the principle test shows that the method of multi-domain/multi-level combination can achieve a

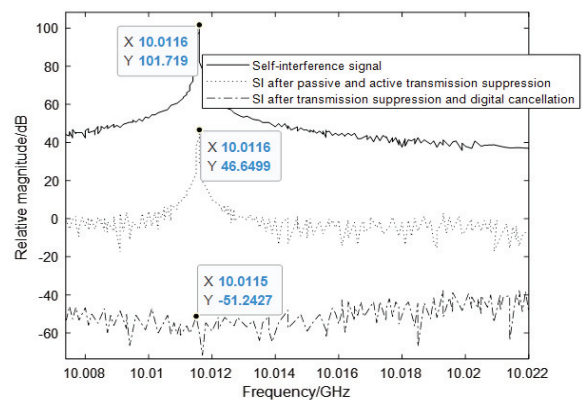


Fig. 7. Experimental results of multi-domain integration for self-interference cancellation of simultaneous transmit and receive phased array.

good effect for the elimination of strong self-interference in the simultaneous transmit and receive phased array system.

## V. CONCLUSION

Based on the electromagnetic modeling and digital modeling analysis of the coupling interference characteristics between phased array antenna elements, this paper breaks through the key technologies of simultaneous transmission and reception of electromagnetic radiation under the actual constraints of the array system, and adaptive digital identification and cancellation. Simultaneous multi-domain and multi-level self-interference suppression/cancellation principle model and implementation process, through the multi-domain comprehensive interference suppression principle test, the principle evaluation of key technologies and optimization models has been realized. The cancellation method and its process are processed according to the transmission and coupling characteristics of the radio frequency interference signal, and can be popularized and applied in the system self-interference cancellation requirements of different frequency bands and different functions.

## REFERENCES

- [1] D. Bharadia, E. McMilin, and S. Katti, "Full duplex radios," *Proceedings of ACM SIGCOMM*, 2013.
- [2] J. I. Choi, M. Jain, K. Srinivasan, P. Levis, and S. Katti, "Achieving single channel, full duplex wireless communications," *Proceedings of ACM MobiCom*, 2010.
- [3] M. Li, X. Chen, A. Zhang, A. A. Kishk, and W. Fan, "Reducing correlation in compact arrays by adjusting near-field phase distribution for mimo applications," *IEEE Transactions on Vehicular Technology*, vol. 70, pp. 7885-7896, 2021.
- [4] Y. Da, Z. Zhang, X. Chen, and A. Kishk, "Mutual coupling reduction with dielectric superstrate for base station arrays," *IEEE Antennas and Wireless Propagation Letters*, vol. 20, pp. 843-847, 2021.
- [5] M. Li, X. Chen, A. Zhang, W. Fan, and A. A. Kishk, "Split ring resonator loaded baffles for decoupling of dual-polarized base station array," *IEEE Antennas and Wireless Propagation Letters*, vol. 19, pp. 1828-1832, 2020.
- [6] J. Zhang, S. Li, W. Chang, T. Jiang, B. Li, and Z. Liang, "Study on full-duplex channel characteristic for simultaneous transmit and receive used in phased array," *Proceedings of IEEE AP-S*. 2019.
- [7] E. Everett, "SoftNull many-antenna full-duplex wireless via digital beamforming," *IEEE Transactions on Wireless Communications*, vol. 15, pp. 8077-8092, 2016.
- [8] J. P. Doane, "Simultaneous transmit and receive with digital phased arrays," *Proceedings of IEEE International Symposium on Phased Array Systems and Technology (PAST)*, pp. 1-6, 2016.
- [9] I. T. Cummings, J. P. Doane, T. J. Schulz, and T. C. Havens, "Aperture-level simultaneous transmit and receive with digital phased arrays," *IEEE Transactions on Signal Processing*, vol. 68, pp. 1243-1258, 2020.
- [10] X. Liu, Z. Xiao, L. Bai, J. Choi, P. Xia, and X.-G. Xia, "Beamforming based full-duplex for millimeter-wave communication," *Sensors*, vol. 16, no. 7, 2016.
- [11] Z. Xiao, P. Xia, and X. Xia, "Full-duplex millimeter-wave communication," *IEEE Wireless Communications*, vol. 24, pp. 136-143, 2017.
- [12] J. Zhang and J. Zheng, "Prototype verification of self-interference suppression for constant-amplitude full-duplex phased array with finite phase shift," *Electronics*, vol. 11, no. 3 pp. 295, 2022.
- [13] A. J. Fenn, "Evaluation of adaptive phased array antenna, far-field nulling performance in the near-field region," *IEEE Transactions on Antennas and Propagation*, vol. 38, pp. 173-185, 1990.
- [14] A. D. Yaghjian, "An overview of near-field antenna measurements," *IEEE Transactions on Antennas and Propagation*, vol. 34, pp. 30-45, 1986.
- [15] A. Sayers, W. Dorsey, K. O'Haver, and J. Valenzi, "Planar near-field measurement of digital phased arrays using near-field scan plane reconstruction," *IEEE Transactions on Antennas and Propagation*, vol. 60, pp. 2711-2718, 2012.
- [16] D. Bharadia and S. Katti, "Full duplex MIMO radios," *Proceedings of the 11th USENIX Conference on Networked Systems Design and Implementation*, pp. 359-372, 2014.
- [17] Z. Zhang, K. Long, A. V. Vasilakos, and L. Hanzo, "Full-duplex wireless communications: challenges, solutions, and future research directions," *Proceedings of the IEEE*, vol. 104, pp. 1369-1409, 2016.
- [18] T. Riihonen, S. Werner, and R. Wichman, "Mitigation of loopback self-interference in full-duplex MIMO relays," *IEEE Transactions on Signal Processing*, vol. 59, pp. 5983-5993, 2011.
- [19] J. Zhang, W. Chang, and T. Jiang, "Research on modeling and principle verification of full-duplex technology based on phased array," *IEEE Radar Conference (RadarConf20)*, Florence, Italy, 2020.
- [20] D. L. Gerber, "Adaptive transmit beamforming for simultaneous transmit and receive," Master's thesis, Massachusetts Institute of Technology, 2011.
- [21] K. E. Kolodziej, J. G. McMichael, and B. T. Perry, "Multitap RF canceller for in-band full-duplex

- wireless communications,” *IEEE Transactions on Wireless Communications*, vol. 15, pp. 4321-4334, 2016.
- [22] B. Liu, X. Chen, J. Tang, A. Zhang, and A. Kishk, “Co- and cross-polarization decoupling structure with polarization rotation property between linearly polarized dipole antennas with application to decoupling of circularly polarized antennas,” *IEEE Transactions on Antennas and Propagation*, vol. 70, no. 1, pp. 702-707, 2022.
- [23] S. Song, Y. Da, B. Qian, X. Huang, X. Chen, Y. Li, and A. A. Kishk, “Dielectric resonator magnetoelectric dipole arrays with low cross polarization, backward radiation, and mutual coupling for MIMO base station applications,” *China Communications*, in press.
- [24] T. Jiang, T. Jiao, and Y. Li, “A low mutual coupling MIMO antenna using periodic multi-layered electromagnetic band gap structures,” *Applied Computational Electromagnetics Society (ACES) Journal*, vol. 33, no. 3, pp. 305-311, 2018.
- [25] S. Luo and Y. Li, “A low mutual coupling antenna array with gain enhancement using metamaterial loading and neutralization line structure,” *Applied Computational Electromagnetics Society (ACES) Journal*, vol. 34, no. 3, pp. 411-418, 2019.
- [26] Y. Wang, X. Chen, X. Liu, J. Yi, J. Chen, and A. Zhang, “Improvement of diversity and capacity of MIMO system using scatterer array,” *IEEE Transactions on Antennas and Propagation*, vol. 70, no. 1, pp. 789-794, 2022.
- [27] E. Aryafar and A. Keshavarz-Haddad, “PAFD: phased array full-duplex,” *IEEE Conference on Computer Communications*, Honolulu, HI, 2018.
- [28] K. E. Kolodziej, J. P. Doane, B. T. Perry, and J. S. Herd, “Adaptive beamforming for multi-function in-band full-duplex applications,” *IEEE Wireless Communications*, pp. 28-35, 2021.
- [29] J. S. Herd and M. D. Conway, “The evolution to modern phased array architectures,” *Proceedings of the IEEE*, vol. 104, no. 3, pp. 1-11, 2016.



**Jie Zhang** received his Ph.D. degree from the School of Information Science and Engineering of Southeast University, Nanjing, China, in 2006. He joined Nanjing Research Institute of Electronics Technology in 2006.

His research interests include radar system technology, simultaneous transmitting and receiving, radar waveform design.



**Hongchao Wu** received his B.E. and Ph.D. degrees in Communication Engineering from Southeast University, Nanjing, China, in 1999 and 2006, respectively. He joined Nanjing Research Institute of Electronic Technology in 2006.

His research interests include solid-state active phased array antenna and digital array antenna.

